

極低温走査型トンネル顕微鏡を用いた高温超伝導体の
表面観察とスペクトロスコピー

南 任 真 史

**Cryogenic Scanning Tunneling
Microscopy and Spectroscopy
on
High Temperature
Superconductors**

極低温走査型トンネル顕微鏡を用いた高温超伝導体の
表面観察とスペクトロスコピー

by
Masashi NANTOH

南任真史

*Superconductivity Course
Graduate School
University of Tokyo*

March, 1995

Contents

Chapter 1 General Introduction	1
1.1 Problems in Tunneling Spectroscopy on High Temperature Superconductors (HTSC's)	1
1.2 Application of Scanning Tunneling Microscopy and Spectroscopy (STM/STS) to HTSC's	3
1.3 Organization of This Dissertation	4
Chapter 2 Theories	7
2.1 Theories of Tunneling	7
2.1.1 Basic Concept of Tunneling	7
2.1.2 Quasiparticle Tunneling	10
2.1.3 Gap Broadening by Quasiparticle Recombination in a Strong Electron-Phonon Coupling System	15
2.2 STM/STS Technique	17
2.2.1 Local Probe Method	17
2.2.2 Resolution	18
2.2.3 Free-Electron Model	20
2.2.4 Operating Modes	23
2.2.5 Imaging	25
2.2.6 Spectroscopy	25
Chapter 3 Experimental	29
3.1 Design of Cryogenic STM	29
3.1.1 Hardware	29
3.1.2 Probe Tips	33
3.1.3 Electronics	34
3.2 Sample Preparation	36
3.2.1 Crystal Structures and Electronic Natures of HTSC's	36
3.2.2 $\text{Bi}_2\text{Sr}_2\text{CaCu}_2\text{O}_y$ (BSCCO) Single Crystals	40
3.2.3 $\text{YBa}_2\text{Cu}_3\text{O}_y$ (YBCO) Thin Films	41

CONTENTS

Chapter 4 Observations on BSCCO Single Crystals	46
4.1 Introduction	46
4.2 STM Observations on Cleaved Surfaces of BSCCO Single Crystals	52
4.3 STS Measurements on Cleaved Surfaces of BSCCO Single Crystals	55
4.3.1 Atomic Site Tunneling-Spectroscopy (AST) Measurements on Surface BiO Layers	55
4.3.2 Superconducting Energy Gap	58
4.3.3 Temperature Dependence of Superconducting Energy Gap	63
4.3.4 Oxygen Content Dependence of Electronic Structure	65
4.3.5 Barrier Width Dependence of Tunneling Spectrum	68
4.3.6 Energy Resolution Dependence of Superconducting Spectrum	74
4.4 Tunneling Spectroscopy on Cross-Sectional Surfaces of BSCCO Single Crystals	76
4.5 Tunneling Spectroscopy on Cleaved Surfaces of $\text{Bi}_{1-x}\text{Pb}_x\text{Sr}_{1-x}\text{CaCu}_2\text{O}_y$ Single Crystals	78
4.6 Discussions	81
4.6.1 Estimation of Superconducting Gap Energy	81
4.6.2 Origins of Broadening of Superconducting Gap Structure	84
4.6.3 Explanation for Spectrum Variation Depending on Barrier Width	86
4.7 Conclusions	92
Chapter 5 Observations on YBCO Thin Films	99
5.1 Introduction	99
5.2 STM Observations on (001) Oriented YBCO Thin Films	102
5.3 STS Measurements on (001) Oriented YBCO Thin Films	105
5.3.1 AST Measurement on Surface Layer	105
5.3.2 Barrier Width Dependence of Tunneling Spectrum	106
5.3.3 Superconducting Energy Gap	109
5.4 STM Observations on (110) Oriented YBCO Thin Films	110
5.5 STS Measurements on (110) Oriented YBCO Thin Films	113
5.5.1 Spatial Variation of Electronic Structure	113
5.5.2 Tunneling Spectroscopy Changing Barrier Width	116
5.5.3 Superconducting Energy Gap	117
5.6 Discussions	118
5.6.1 Growth Mechanisms of YBCO Thin Films	118
5.6.2 Models for Surface Termination of (001) Oriented Film	120
5.6.3 Origins of High Zero-Bias Conductance Values in Superconducting Spectra	121
5.6.4 Symmetry of Cooper Pair	122
5.7 Conclusions	125

Chapter 6 Typical Structures Appeared in Tunneling Spectra by Extrinsic Effects	129
Chapter 7 Explanations for Variations and Anomalous Behaviors of Tunneling Spectra Measured on HTSC's	136
Chapter 8 General Conclusions	152
List of Publications	154
Acknowledgements	158

Chapter 1

General Introduction

1.1 Problems in Tunneling Spectroscopy on High Temperature Superconductors (HTSC's)

Tunneling spectroscopy discovered by Giaever [Refs. 1, 2], is probably the most powerful experimental method for studying the density of states in superconductors. By this technique the tunneling current between two metals separated by a very thin insulator is measured as a function of the applied voltage, and from this the density of states is rather easily deduced with very high energy resolution. The simplicity of the method and the wealth of information it yields have led to many tunneling measurements on superconductors. Actually, the results constituted the most detailed comparison of the Bardeen-Cooper-Shliefer (BCS) theory [Ref. 3] with experiments, and became one of the most important experimental proofs for the BCS mechanism.

In 1986, an oxide ceramic superconductor which has relatively high critical temperature (T_c) was discovered by J. G. Bednorz and K. A. Müller [Ref. 4]. A series of compounds which have similar layered structures containing CuO_2 planes were discovered in a year, and some of them showed higher T_c 's than expected by the BCS theory, which would be called high temperature superconductors (HTSC's). It was pointed out that the mechanism of superconductivity of these materials may be different from the phonon-mediated coupling mechanism of the BCS theory, and a great deal of work has been concentrated on investigations on the HTSC's.

It is natural to think that tunneling spectroscopy is one of the suitable ways to study these new materials, and actually a number of tunneling experiments have been done so far. However, in the early stage of the tunneling study on the HTSC's, this technique was less informative than expected because of its poor reproducibility [Ref. 5]. The superconducting gap values observed were scattered over a wide range, and the shapes of the spectra differed from one observation to another showing irregular features such as a zero-bias conductance peak, bilateral dip structure and multiplex structure. As the qualities of the specimens employed and the experimental techniques were improved, the results became somewhat convergent. A certain consensus was reached about the size of the superconducting gap [Ref. 5], and the better understanding of the origins of the irreproducibility made it possible to distinguish extrinsic structures in the spectrum from intrinsic ones.

Nevertheless, there still remain problems in this field as follows.

- 1) The superconducting gap structure tends to appear in a broadening shape.
- 2) Considerably high inner-gap conductance is observed.

- 3) The background conductance of the spectrum, which is expected to be rather flat in the case of normal metal, often shows linear feature (V-shape).
- 4) Unexpected dip structure appears just outside the peak of the superconducting gap structure, which is enhanced in the occupied states.

These facts have been explained by means of new theories for the HTSC mechanism, e.g., resonating valence bond (RVB) model proposed by Anderson [Ref. 6] and marginal Fermi liquid model proposed by Varma *et al.* [Ref. 7].

However, even though experimental techniques of junction fabrication have been improved, there seems to be technical problems originating from the characteristics of the HTSC. In the case of break junction or point contact, small particles, which cause coulomb blockade [Ref. 8] and charging effect [Ref. 9], tend to be created by breakage or chipping due to fragileness of the HTSC materials. On the other hand, instability of the surface of the HTSC does not allow fabrication process of a planar type junction to avoid chemical reaction or oxygen depletion at the interface which causes poor characteristics of the superconducting gap structure.

Moreover, all these conventional tunneling techniques have macroscopic junction areas. Therefore, in order to observe an intrinsic nature of the material, an ideal state should be realized over the wide area of the interface, which seems to be difficult especially when the junction is fabricated on the *c*-plane of the HTSC because of the extremely short coherence length along the *c*-axis (ξ_c) of this material [Ref. 10]. If some regions of the junction area do not have ideal conditions, the tunneling spectrum must have the contributions from such areas which cause the broadening and the irregular structures of the spectrum, and this is more real than a perfect junction in the case of these macroscopic junction methods.

Furthermore, there is a possibility that a superconducting order parameter has spatial variation along the *c*-axis even in one unit cell of the crystal structure of the HTSC. The HTSC's are fundamentally composed of conductive CuO_2 layers and electrically rather inert ionic layers stacked alternately. A consensus has been reached about the fact that the CuO_2 layers are basically responsible for the quasi two dimensional (2D) superconductivity of this system. If we consider the ξ_c value which has been estimated to be as short as 1 to 2 Å, the order parameter may vary in the *c*-direction with a periodicity comparable to the atomic scale. This suggests that the tunneling data of macroscopic junctions reflect the electronic natures of both superconducting CuO_2 layers and other nonsuperconducting or weakly superconducting layers, which intrinsically makes it almost impossible to probe the original superconducting state of this material by these conventional tunneling methods. Tachiki *et al.* discussed this possibility in their layered model [Ref. 11] and predicted the intrinsic flux pinning [Ref. 12]. Artemenko *et al.* proposed the pancake vortex model considering these facts [Ref. 13]. Recently, Kleiner *et al.* reported that they observed Josephson coupling between CuO_2 double layers in $\text{Bi}_2\text{Sr}_2\text{CaCu}_2\text{O}_8$ single crystals by direct measurements of ac and dc Josephson effects with current flow along the *c*-axis, which indicates that this system behaves like a series array of Josephson junctions [Ref. 14]. All these can be circumstantial evidence of the spatial variation of the superconducting order parameter. However, in order to

prove it directly, we have to observe the local electronic structure of the HTSC material with a microscopic probe.

1.2 Application of Scanning Tunneling Microscopy and Spectroscopy (STM/STS) to HTSC's

Scanning tunneling microscopy (STM) was invented by Binnig and Rohrer [Refs. 15-18] as a probe to investigate surface topography of a material with atomic resolution. It was found that STM is also useful as a way of tunneling spectroscopy. In this method, the area where tunneling current flows is very small, which is considered as the order of an atomic scale (see Fig. 1.1). Therefore, the information about the local density of states can be obtained. Furthermore, if both STM and tunneling spectroscopy are done simultaneously, the spatial variation of the electronic structure of the material can be probed with atomic resolution (STS: scanning tunneling spectroscopy). Besides, the tunneling spectroscopy using STM has some other advantages. In this technique, undesired chemical reaction or mechanical damage of the material surface can be avoided because the tunneling barrier is vacuum, and the sample surface can be characterized by the STM picture taken at the measuring position. All these characteristics of this technique are thought to be very suitable for the observation on the HTSC which has peculiarities described above.

In order to observe a superconductor when it is in a superconducting state, it is necessary to measure it at the temperature lower enough than its T_c . Although development of a cryogenic STM apparatus which can be operated at liquid He temperature (4.2 K) has some difficulties as described in section 3. 1. 1, several groups have been successful in the development and tried cryogenic observations on the HTSC's so far [Refs. 19-21]. However, most of these experiments were not reproducible, and not so informative as expected.

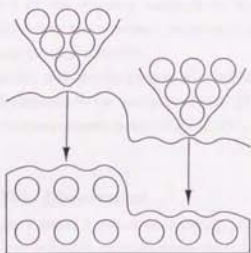


Fig. 1.1 Observing area in STM.

As mentioned above, the most significant characteristic of the tunneling spectroscopy using STM is that the tunneling area is an atomic order, which is the reason why atomic resolution images can be obtained by STM. Considering this, the conditions of small tunneling areas of both sides (*i.e.*, the STM tip and the sample surface) are very important to obtain reliable tunneling data by using STM. If the STM tip is not clean, accurate information cannot be obtained from the tunneling spectra, and if the nature of the observed area of the sample surface does not represent the original nature of the material, intrinsic properties cannot be derived from the data. Therefore, from this aspect, the tunneling data obtained by using STM should be treated much more carefully than those by macroscopic tunneling methods in which the tunneling spectrum gives information integrated over the wide junction area. Any accurate information cannot be obtained based on the tunneling data using STM without the ideal condition, and it is very dangerous to derive some conclusions from such data. From this point of view, the following points are fatally significant in this measurement.

- 1) The observed area of the sample surface is stable and keeps the ideal condition, and this is checked and secured by STM imaging.
 - 2) The STM tip is well controlled not to crash onto the sample surface, and keeps its cleanness.
- It seems that the sole way to estimate attainment of these requirements is to verify whether an atomic resolution image can be obtained or not.

Most of the previous works employed specimens whose qualities were not so high as those obtained now, and actually they reported that an insulating oxide shell was formed at the surface of the specimen. In these experiments, the STM tip was contacted onto the sample surface, and superconducting gap structure was observed only when the tip was driven into the surface layer deeply and it was very rare. Besides, the superconducting spectra observed were of rather poor quality sometimes with irregular structures described above. Atomic resolution STM imaging was not achieved but only rough surface topographic images were obtained, thus it was not clear whether they are real surfaces of the observed materials or not. Taking these facts into consideration, it seems to be difficult to derive intrinsic properties from these experiments because STM was used as a probe without the ideal condition.

From these reasons, we began this study for the purpose of doing tunneling measurements at low temperature on the surface well estimated by the atomic resolution STM imaging, which is thought to yield reliable data reflecting the true electronic nature of the HTSC.

1.3 Organization of This Dissertation

In Chapter 2, we will discuss a theory involved in tunneling phenomena, which was studied mainly in 1960's. We will also introduce semi-phenomenological theories about quasiparticle tunneling established by Giaever and Megerle [Ref. 22] and by Dynes *et al.* [Ref. 23]. In this chapter, we will also make a general survey of the STM/STS technique and discuss a model explaining the resolution realized in STM.

The actual experimental details will be presented in Chapter 3. The design of our cryogenic STM will be demonstrated clearing the problems caused by the cryogenic operation and the means to solve them. Although the specimens employed in this work were provided by another group of Kitazawa laboratory and Koinuma laboratory (Tokyo Institute of Technology), we will give a brief explanation of the procedures of crystal growth and film deposition.

The results of observations on $\text{Bi}_2\text{Sr}_2\text{CaCu}_2\text{O}_x$ single crystals and $\text{YBa}_2\text{Cu}_3\text{O}_y$ thin films will be presented in Chapter 4 and Chapter 5, respectively. STM images of surface topography and atomic corrugation and STS results, including the dependence of the spectra on temperature, oxygen content, barrier width, energy resolution, will be demonstrated. Then we will focus on some subjects which are still unclear in spite of their significance, and try some discussions and speculations based on the data obtained in this work.

In Chapter 6, we will discuss some typical structures appeared in tunneling spectra which are thought to be caused by extrinsic effects. This kind of spectral features have been reported by a number of groups, too [Ref. 5]. Some of them interpreted these structures as intrinsic ones, which has made this field of study more complex to understand. We will explain the extrinsic origins of them considering our experimental results.

Finally, in Chapter 7, we will explain the variation of the tunneling spectroscopic results presented in Chapter 4 and Chapter 5. Then we will return to the problem discussed in section 1.1, the anomalous behaviors of tunneling spectra measured on the HTSC's. We will try to interpret these behaviors based on our experiments.

Although this field of research has become clearer and more convergent, it still seems to be quite controversial. I hope this dissertation will give useful information to all the researchers working in this field.

References

- [1] I. Giaever, Phys. Rev. Lett. 5, 147 (1960).
- [2] I. Giaever, Phys. Rev. Lett. 5, 464 (1960).
- [3] J. Bardeen, L. N. Cooper, and J. R. Schrieffer, Phys. Rev. 108, 1175 (1957).
- [4] J. G. Bednorz, and K. A. Müller, Z. Phys. B 64, 189 (1986).
- [5] See T. Hasegawa, H. Ikuta, and K. Kitazawa, *Physical Properties of High Temperature Superconductors III*, edited by D. M. Ginsberg, World Scientific Publishing, 525 (1992).
- [6] P. W. Anderson, and Z. Zou, Phys. Rev. Lett. 60, 132 (1988).
- [7] C. M. Varma, P. B. Littlewood, S. Schmitt-Rink, E. Abrahams, and A. E. Ruckenstein, Phys. Rev. Lett. 63, 1996 (1989).
- [8] P. J. M. van Bentum, H. van Kempen, L. E. C. van de Leemput, and P. A. A. Teunissen, Phys. Rev. Lett. 60, 369 (1988).
- [9] P. J. M. van Bentum, R. T. M. Smokers, and H. van Kempen, Phys. Rev. Lett. 60, 2543 (1988).

- [10] G. Deutscher, and K. A. Müller, *Phys. Rev. Lett.* 59, 1745 (1987).
- [11] M. Tachiki, S. Takahashi, F. Steglich, and H. Adrian, *Z. Phys. B* 80, 161 (1990).
- [12] M. Tachiki, and S. Takahashi, *Solid State Comm.* 70, 291 (1989).
- [13] S. N. Artemenko, and A. N. Kruglov, *Phys. Lett. A* 143, 485 (1990).
- [14] R. Kleiner, F. Steinmeyer, G. Kunkel, and P. Müller, *Phys. Rev. Lett.* 68, 2394 (1992).
- [15] G. Binnig, H. Rohrer, C. Gerber, and E. Weibel, *Appl. Phys. Lett.* 40, 178 (1982).
- [16] G. Binnig, H. Rohrer, C. Gerber, and E. Weibel, *Phys. Rev. Lett.* 49, 57 (1982).
- [17] G. Binnig, H. Rohrer, C. Gerber, and E. Weibel, *Phys. Rev. Lett.* 50, 120 (1983).
- [18] G. Binnig, H. Rohrer, C. Gerber, and E. Weibel, *Surf. Sci.* 131, L379 (1983).
- [19] M. C. Gallagher, and J. G. Adler, *J. Vac. Sci. Technol. A* 8, 464 (1990).
- [20] R. Wilkins, M. Amman, R. E. Soltis, E. Ben-Jacob, and R. C. Jaklevic, *Phys. Rev. B* 41, 8904 (1990).
- [21] J. R. Kirtley, *Int. J. Mod. Phys. B* 4, 201 (1990).
- [22] I. Giaever, and K. Megerle, *Phys. Rev.* 122, 1101 (1961).
- [23] R. C. Dynes, V. Narayanamurti, and J. P. Garno, *Phys. Rev. Lett.* 41, 1509 (1978).

Chapter 2

Theories

2.1 Theories of Tunneling

2.1.1 Basic Concept of Tunneling [Ref. 1]

Most of the features of tunneling phenomena in solids are essentially of a one-dimensional (1D) nature. If the tunneling barrier extends in the x direction, the momentum in the y and z directions can usually be taken to be constants, and hence are merely fixed parameters. In this section a basic concept of tunneling by studying purely a 1D problem is described. Almost all of our results have wider ranges of applicability to real situations than 1D problems usually have.

We will, in fact, study the simplest of all 1D problems, namely, square barriers and square wells in one dimension. The Schrödinger equation have the simple form

$$\left(\frac{p^2}{2m} + V\right)\psi = E\psi \quad (2.1)$$

where V is a constant in a given region. The general solution of Eq. 2.1 has the well-known form

$$\psi(x) = ae^{ikx} + be^{-ikx} \quad (2.2)$$

$$\frac{\hbar^2 k^2}{2m} = E - V \quad (2.3)$$

When $E - V > 0$ the wave functions are for plane waves. When $E - V < 0$ we will write $k = i\kappa$ and

$$\psi(x) = ae^{-\kappa x} + be^{\kappa x} \quad (2.4)$$

The wave functions are now exponentially growing and decaying waves characteristic of barrier penetration problems. In the "square barrier" and "square well" problem which we will discuss V changes abruptly from one constant value to another. The overall wave function is then constructed out of pieces having the form of Eq. 2.2 by matching ψ and $d\psi/dx$ at the discontinuities of V .

The basic matching problem can be done at a potential step as shown in Fig. 2.1. The matching conditions are then conveniently described as a 2×2 matrix R operating on the two-dimensional

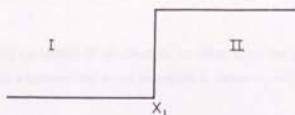


Fig. 2.1 Potential step.

(2D) vectors

$$\begin{pmatrix} a_1 \\ b_1 \end{pmatrix} \quad \text{and} \quad \begin{pmatrix} a_2 \\ b_2 \end{pmatrix}$$

which describe the wave function in regions I and II, respectively. We may write

$$\begin{pmatrix} a_1 \\ b_1 \end{pmatrix} = R_1 \begin{pmatrix} a_2 \\ b_2 \end{pmatrix} \quad (2.5)$$

$$R_1 = \frac{1}{2k_1} \begin{pmatrix} (k_1 + k_2) \exp[i(-k_1 + k_2)x_1] & (k_1 - k_2) \exp[i(-k_1 - k_2)x_1] \\ (k_1 - k_2) \exp[i(k_1 + k_2)x_1] & (k_1 + k_2) \exp[i(k_1 - k_2)x_1] \end{pmatrix} \quad (2.6)$$

Eqs. 2.5 and 2.6 are valid for either real or imaginary values of k . The general problem of any number of square barriers or wells may then be briefly described in terms of a chain of operators of the form R_j .

We turn first to the square barrier problem of Fig. 2.2. We may write the solution

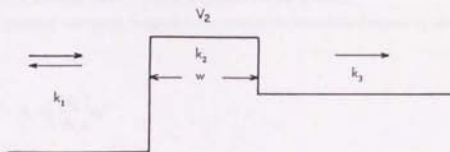


Fig. 2.2 Square barrier problem.

$$\begin{pmatrix} a_1 \\ b_1 \end{pmatrix} = R_1 R_2 \begin{pmatrix} a_3 \\ b_3 \end{pmatrix} \quad (2.7)$$

Let us study the boundary condition of an electron incident from the left. There will be a reflected wave in region 1 but only a transmitted wave in region 3, hence $b_3 = 0$. We want a_3 in terms of a_1 . Eq. 2.7 then gives

$$a_1 = (R_1 R_2)_{11} a_3 \quad (2.8)$$

Explicit evaluation of Eq. 2.8 with the use of Eq. 2.6 results in

$$(R_1 R_2)_{11} = \frac{\exp(ik_1 x_2 - ik_1 x_1) [(k_1^2 + \kappa_2^2)^{1/2} (k_3^2 + \kappa_2^2)^{1/2} \{\exp(i\alpha + \kappa_2 \omega) - \exp(-i\alpha - \kappa_2 \omega)\}]}{4ik_1 \kappa_2}$$

$$\alpha = \tan^{-1} \left(\frac{\kappa_2}{k_1} \right) + \tan^{-1} \left(\frac{\kappa_2}{k_3} \right) \quad (2.9)$$

$$\kappa_2 = ik_2 \quad \omega = x_2 - x_1 \quad (2.10)$$

Real plane waves are assumed in regions 1 and 3 and tunneling in region 2. To simplify the formula, we will neglect $\exp(-\kappa_2 \omega)$ in comparison to $\exp(\kappa_2 \omega)$. Then we have

$$a_3 = \frac{4k_1 \kappa_2 \varphi \exp(-\kappa_2 \omega)}{(k_1^2 + \kappa_2^2)^{1/2} (k_3^2 + \kappa_2^2)^{1/2}} a_1 \quad (2.11)$$

$$\varphi = i \exp(-i\alpha) \exp(ik_1 x_1 - ik_3 x_2) \quad (2.12)$$

φ is a phase factor of absolute value 1, which is ignored for the moment.

The quantity of physical interest to compute is the ratio of the transmitted current j_t to the incident current j_i

$$j_t = \left(\frac{\hbar k_1}{m} \right) a_1^2 \quad j_s = \left(\frac{\hbar k_3}{m} \right) a_3^2 \quad (2.13)$$

We find

$$\frac{j_2}{j_1} = \frac{16k_1 k_2 \kappa_2^2}{(k_1^2 + \kappa_2^2)(k_2^2 + \kappa_2^2)} \exp(-2\kappa_2 \omega) \quad (2.14)$$

$$\frac{\hbar^2 \kappa_2^2}{2m} = V_2 - E \quad (2.15)$$

The dominant feature of Eq. 2.14 is the barrier penetration factor $\exp(-2\kappa_2 \omega)$. In typical problems of interest this factor may be 10^{-5} - 10^{-10} , so that it tends to dominate the prefactor.

2.1.2 Quasiparticle Tunneling

The semi-phenomenological theory of tunneling introduced by Giaever and Megerle [Ref. 2] is essentially a one-dimensional model which assumes that the quasi-particles can be treated as independent Fermi-Dirac particles occupying a given state of energy E with a probability $f = [1 + \exp(\beta E)]^{-1}$. The tunneling current from metal 1 to metal 2 is assumed to be proportional to the density of occupied states at a given energy in the metal 1 and to the density of unoccupied states in the metal 2, at the same energy. This current is also assumed to be proportional to the probability for a given quasi-particle of this energy to tunnel through the barrier. When integrated over all energies this gives

$$i_{12} = \left(\frac{2\pi}{h} \right) \int_{-\infty}^{\infty} |M|^2 \rho_1 f_1 (1 - f_2) dE \quad (2.16)$$

where M is the matrix element between states of equal energy in the two metals. By subtracting a similar expression for the current from the metal 2 to the metal 1, we obtain for the net current

$$I = A \int_{-\infty}^{\infty} |M|^2 \rho_2 (f_1 - f_2) dE \quad (2.17)$$

To adapt the analysis to tunneling with superconductors the following assumptions were made.

- 1) The density of states in a normal metal is a constant, $\rho_n = N(0)$.
- 2) The density of states in a superconductor ρ_s at $T = 0$ K is given by the BCS relation

$$\rho = \begin{cases} N(0) \frac{|E|}{\sqrt{E^2 - \Delta^2}} & |E| \geq \Delta \\ 0 & |E| < \Delta \end{cases} \quad (2.18)$$

- 3) The matrix element M is independent of energy in the region of interest and is independent of whether the metals are superconducting or not.
- 4) The difference between the Fermi energies of the two metals equals the difference in electrical potential, V .

Measuring the energy in eV from the Fermi energy of the metal 1 the tunneling current becomes

$$I = A \int_{-\infty}^{\infty} \rho_1(E) \rho_2(E+V) [f(E) - f(E+V)] dE \quad (2.19)$$

where $A = (2\pi e/h) |M|^2$. When both metals are normal, Eq. 2.19 reduces to

$$I_{nn} = AN_1(0)N_2(0) \int_{-\infty}^{\infty} [f(E) - f(E+V)] dE \quad (2.20)$$

At low temperatures and voltages ($1 \ll bE_p$, $V \ll E_p$) the integral is easily evaluated and gives

$$I_{nn} = C_n V \quad (2.21)$$

where the constant, $C_n = AN_1(0)N_2(0)$, is the conductance for normal-normal tunneling.

When the metal 1 is superconducting and the metal 2 is normal, Eq. 2.19 gives

$$I_{ns} = \frac{C_n}{N_1(0)} \int_{-\infty}^{\infty} \rho_1(E) [f(E) - f(E+V)] dE \quad (2.22)$$

Differentiating this expression with respect to the applied voltage, we obtain

$$\frac{dI_{ns}}{dV} = \frac{C_n}{N_1(0)} \int_{-\infty}^{\infty} \rho_1(E) \left(\frac{\beta \exp[\beta(E+V)]}{\{1 + \exp[\beta(E+V)]\}^2} \right) dE \quad (2.23)$$

The second factor in this integral is a bell-shaped function which is symmetrical about its maximum, $\beta/4$, which is located at $E = -V$. The magnitude of this maximum is proportional to $1/T$ and at $T = 0$ the function degenerates into a delta function and

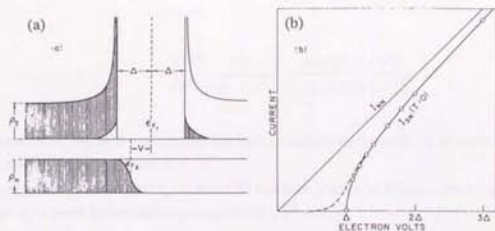


Fig. 2.3 (a) Schematic representation of the density of states in a superconductor-oxide-normal metal tunnel junction at a finite temperature. (b) Current as a function of voltage for such a junction at $T = 0$, $T/T_c = 0.2T_c$, and $T > T_c$. From [Ref. 3].

$$\left(\frac{dI_m}{dV}\right)_{T=0} = \begin{cases} C_n \frac{|V|}{\sqrt{V^2 - \Delta^2}} & |V| \geq \Delta \\ 0 & |V| < \Delta \end{cases} \quad (2.24)$$

If Δ is independent of energy these equations can be integrated to give

$$I_m = \begin{cases} C_n \sqrt{V^2 - \Delta^2} & V \geq \Delta \\ 0 & V < \Delta \end{cases} \quad (2.25)$$

Qualitatively this result can be understood from the density of states diagram of Fig. 2.3(a) and the resulting tunneling characteristic of Fig. 2.3(b). At $T = 0$ there evidently can be no current from the superconductor until the applied voltage depresses the effective Fermi energy of the normal metal by an amount which is equal to Δ . At that time current starts to flow and at higher voltages the current asymptotically approaches the straight line of normal-normal tunneling. At a finite temperature well below T_c the exponential tail of the Fermi distribution always gives a finite conduction, but there remains a sudden rise for $V = \Delta$ as shown in Fig. 2.3(b) for $T/T_c = 0.2$.

When $T \neq 0$ the BCS conductance from Eq. 2.24 is

$$\frac{dI_m}{dV} = \frac{C_n}{N_s(0)} \int_{\Delta}^{\infty} \frac{|E|}{\sqrt{E^2 + \Delta^2}} \left(\frac{\beta \exp[\beta(E+V)]}{\{1 + \exp[\beta(E+V)]\}^2} \right) dE$$

$$+ \int_{-\infty}^{-\Delta} \frac{|E|}{\sqrt{E^2 + \Delta^2}} \left(\frac{\beta \exp[\beta(E+V)]}{\{1 + \exp[\beta(E+V)]\}^2} \right) dE \quad (2.26)$$

This expression for the BCS conductance has been computed numerically by Bermon [Ref. 4] for a large range of parameters $\beta\Delta$ and βV .

The expression for the current I_m in Eq. 2.22 has been shown by Giaever and Megerle [Ref. 2] to be given by a series which converges rapidly for $|V| < \Delta$

$$I_m = 2C_n \Delta \sum_{m=1}^{\infty} (-1)^{m+1} K_1(m\beta\Delta) \sinh(m\beta V) \quad (2.27)$$

where K_1 is a modified Bessel function of the second kind. In the low-voltage limit Eq. 2.27 becomes

$$\lim_{V \rightarrow 0} I_m = 2C_n \Delta \sum_{m=1}^{\infty} (-1)^{m+1} m\beta V K_1(m\beta\Delta) \quad (2.28)$$

which in the low-temperature limit leads to

$$\lim_{V \rightarrow 0, T \rightarrow 0} \frac{I_m}{I_{m0}} = (2\pi\beta\Delta)^{1/2} \exp(-\beta\Delta) \quad (2.29)$$

For the case of superconductor-superconductor tunneling, Eqs. 2.18 and 2.19 lead to the following expression for the tunneling current

$$I_m = C_n \int_{-\infty}^{\infty} \frac{|E|}{\sqrt{E^2 - \Delta_1^2}} \frac{|E+V|}{\sqrt{(E+V)^2 - \Delta_2^2}} [f(E) - f(E+V)] dE \quad (2.30)$$

This result was first given by Nicol *et al.* [Ref. 5], who numerically calculated sample current-voltage curves and showed that at approximately $V = \pm |\Delta_2 - \Delta_1|$ there is a logarithmic singularity in the current of magnitude

$$I_m - \ln|V - (\Delta_2 - \Delta_1)| \quad (2.31)$$

and at $V = \Delta_1 + \Delta_2$ there is a finite discontinuity even at $T \neq 0$

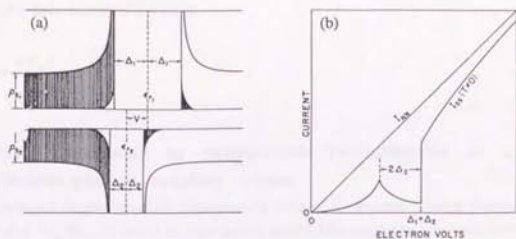


Fig. 2.4 (a) Schematic representation of the density of states in a superconductor-oxide-superconductor tunnel junction at a finite temperature. (b) Current-voltage characteristic calculated from the BCS theory. From [Ref. 3].

$$\Delta I_n = \frac{\pi C_n \sqrt{\Delta_1 \Delta_2}}{4} \frac{\sinh[\beta(\Delta_1 + \Delta_2)/2]}{\cosh(\beta \Delta_1/2) \cosh(\beta \Delta_2/2)} \quad (2.32)$$

These features are shown in Fig. 2.4(b) and may be understood qualitatively by considering the density of states diagram of Fig. 2.4(a) and how the product of occupied and available states of the same energy changes as the voltage is changed. At $T = 0$ Eq. 2.30 reduces to

$$I_n = C_n \int_{-V+\Delta_1}^{\Delta_1} \frac{|E|}{\sqrt{E^2 - \Delta_1^2}} \frac{|E+V|}{\sqrt{(E+V)^2 - \Delta_2^2}} dE \quad (2.33)$$

Eq. 2.33 can be integrated and expressed in terms of complete elliptic integrals [Ref. 6]. The discontinuity in the current at $V = \pm(\Delta_1 + \Delta_2)$ is at $T = 0$

$$\Delta I = \left(\frac{\pi}{2}\right) C_n \sqrt{\Delta_1 \Delta_2} \quad (2.34)$$

When $\Delta_1 = \Delta_2 = \Delta$ and $V < 2\Delta$, Taylor *et al.* [Ref. 7] have computed I_n numerically and have shown that a negative resistance region ($dI/dV < 0$) should appear at $T < 0.3\Delta/k_B$. When $T \ll \Delta/k_B$ and $V < 2\Delta$, the current is well approximated by

$$I_n = 2C_n \exp(-\beta\Delta) \sqrt{\frac{2\Delta}{V+2\Delta}} (V+\Delta) \sinh\left(\frac{\beta V}{2}\right) K_0\left(\frac{\beta V}{2}\right) \quad (2.35)$$

For $T = 0$ the discontinuity at $V = 2\Delta$ is

$$\Delta I = \frac{\pi C_v \Delta}{2} \quad (2.36)$$

2.1.3 Gap Broadening by quasiparticle recombination in a strong electron-phonon coupling system

In a simple and elegant tunneling experiment on films of the extremely strong electron-phonon coupling alloy $\text{Pb}_{0.9}\text{Bi}_{0.1}$, Dynes *et al.* have directly obtained the quasiparticle recombination time τ_R by measuring the corresponding temperature-dependent lifetime broadening of the energy gap edge [Ref. 8]. This effect can be seen directly in the I - V curves of the symmetric strong-coupling $\text{Pb}_{0.9}\text{Bi}_{0.1}$ -I- $\text{Pb}_{0.9}\text{Bi}_{0.1}$ junction, shown as a function of temperature in Fig. 2.5. The broadening shown here, in contrast to the finite discontinuities retained at higher temperatures in the Al-I-Al I - V curves of Fig. 2.6 [Ref. 9], arises from the large inherent width $\Gamma = (\hbar/2\pi)/\tau_R$ of the quasiparticle states due to strong electron-phonon coupling in this system. The strong temperature dependence is expected from the relation

$$\frac{1}{\tau_R} = \left(\frac{k_B T}{\Delta}\right)^{1/2} \frac{1}{\tau_0} \exp\left(-\frac{\Delta}{k_B T}\right) \quad (2.37)$$

which corresponds to the two-particle nature of the recombination process, $1/\tau_R$ for a given particle depends on the number of other particles, $n \propto \exp(-\Delta/k_B T)$.

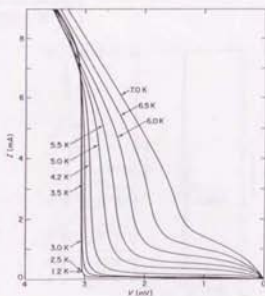


Fig. 2.5 I - V characteristic of $\text{Pb}_{0.9}\text{Bi}_{0.1}$ -I- $\text{Pb}_{0.9}\text{Bi}_{0.1}$ tunnel junction at several different temperatures. From [Ref. 8].

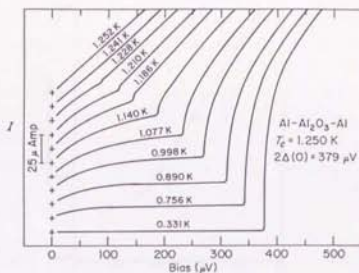


Fig. 2.6 Experimental results for quasiparticle tunneling between identical superconductors. From [Ref. 9].

These data have been analyzed using the S-I-S current expression

$$I = C_n \int_{-\infty}^{\infty} N(E)N(E+V)[f(E) - f(E+V)]dE \quad (2.38)$$

The lifetime broadening is treated simply by adding an imaginary part Γ to the energy variable

$$N(E, \Gamma) = \text{Re} \left\{ \frac{(E - i\Gamma)}{[(E - i\Gamma)^2 - \Delta^2]^{1/2}} \right\} \quad (2.39)$$

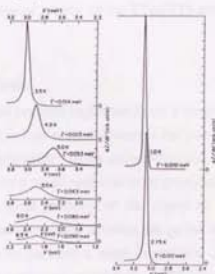


Fig. 2.7 The conductance dI/dV vs. V determined from the data shown in Fig. 2.5. From [Ref. 8].

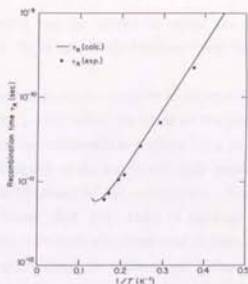


Fig. 2.8 Plot of corresponding recombination time $\tau = (\hbar/2\pi) / \Gamma$ on log scale vs. $1/T$. From [Ref. 8].

Differential I - V curves (data points in Fig. 2.7) have been fit by variation of Γ , using Eqs. 2.38 and 2.39. The excellent fits correspond to the values of Γ shown in the figure. The recombination times $\tau_R = (\hbar/2\pi) / \Gamma$ are plotted (data points) semilogarithmically vs. $1/T$, as appropriate to Eq. 2.37, in Fig. 2.8 and compared with the curve calculated by Kaplan et al. [Ref. 10], based on the $\alpha^2 F(\omega)$ function measured for $Pb_{0.9}Bi_{0.1}$ by superconductive tunneling (Dynes and Rowell [Ref. 11]). The agreement is clearly excellent and does not involve parameters other than the measured Γ values.

2.2 STM/STS Technique

In this section, we will make a general survey of the STM/STS technique.

2.2.1 Local Probe Method

There are two major methods to perform experiments on a single microscopically small object or part thereof. In the first method, a lens system connects the microscopic object with the world of the macroscopic observer or experimenter. In the second method, the microscopic part of the object under investigation is addressed by a small probe in close proximity to the object. This is the local probe method, which probes a local property of the object or produces a local, reversible or irreversible modification *via* some interaction between the probe and the object. It is a natural and conceptually the simplest way to perform a local experiment and, together with the scanning capability of the probe, to image a microscopic object. STM pioneered this technique for imaging and making local modifications on a nanometer scale. In STM, imaging is performed by scanning

a probe over a fixed sample, and the drives for probe are generally built from piezoelectric components. Tripods [Ref. 12] or tube [Ref. 13] drives cover fields of view from a few thousand Å up to several μm.

The major instrumental problems are the vibration isolation of the local probe-object distance and the coarse positioning of the probe within the range of the piezo drives. Vibration isolation is achieved by either protecting the instrument as a whole from its environment [Refs. 14-16] or by making the lowest eigenfrequency of the mechanical path between object and local probe much higher than any mechanical vibrations of the environment. Various coarse-positioning methods have been used since the "louse" [Ref. 14]. Many of them are variations of reductions by lever systems [Refs. 17, 18], often combined with some kind of differential spring and screw systems. Convenient, remote coarse positioning over macroscopic distances in three dimensions, as done in the bioscope [Ref. 19], and at high mechanical eigenfrequencies for fast imaging are challenges for future versatile instrumentation. An interesting approach in this direction are the micromechanical instrument [Refs. 20, 21] or "beetle" type instruments [Ref. 22].

2.2.2 Resolution

The crucial elements for the lateral resolution of local probe methods are the size of the probe, the distance between probe and object and its control, and the distance dependence and lateral variation of the interaction under consideration. Therefore, the resolution depends on the local sample properties, so it is not possible to give simple general resolution criteria. Nevertheless, we can get a feeling for the resolution by considering the width L of the interaction filament, which contains $1-1/\eta$ of the total interaction intensity, as shown in Fig. 2.9. For the distance dependence of $f(d) \propto \exp(-\kappa d)$, we obtain

$$L \cong 2\sqrt{2}\sqrt{\ln\eta}\sqrt{\frac{(s+R)}{\kappa}} \quad (2.40)$$

for STM [Refs. 23, 24]. The value of η depends on the ratio of intensity change due to the object and that due to noise. Stoll [Ref. 25] obtains

$$a = \pi \ln^{-1}\left(\frac{h}{\delta}\right)\sqrt{\frac{(s+R)}{\kappa}} \quad (2.41)$$

where a is the minimum period of a corrugation of height h which can be detected and δ the noise in terms of distance fluctuations. The interaction used for STM imaging is tunneling (Fig. 2.10). The resolution limit can vary appreciably according to the property probed and the smallest practicable probe size. Atomic resolution is generally achieved in STM, in which the apex atom of the probe tip serves as a local probe.

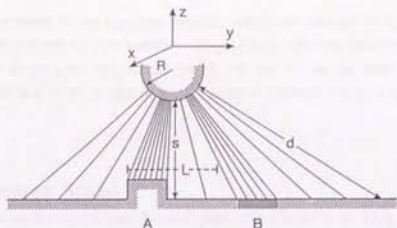


Fig. 2.9 Interaction $f(d)$ between a spherical tip of radius R and the surface of an object at distance s with a geometrical feature at A and an interaction inhomogeneity at B. From [Ref. 26].

The tunneling current is a measure of the overlap of the electronic wave functions of the tip and the sample in the gap between them, *i.e.*, the tip wave functions probe the object wave functions. In the approximation of Tersoff and Hamann [Ref. 23], the tip probes the local density of states at a distance $R+s$ from the surface. The tunneling current depends exponentially on the separation between the probe tip and the sample

$$I = B \exp(-\kappa s) \quad (2.42)$$

The decay length $1/\kappa$ is related to the effective average tunnel barrier height $\bar{\phi}$

$$\kappa = \sqrt{\frac{2m}{\hbar}} \sqrt{\bar{\phi}} = A \sqrt{\bar{\phi}} \quad (2.43)$$

In the case of a vacuum barrier, m is the free electron mass and $A = 1.025 \text{ \AA}^{-1} \text{ eV}^{-1/2}$. At large distances, *e.g.*, $s \geq 20 \text{ \AA}$, $\bar{\phi}$ closely corresponds to the work function, while at small distances the average tunnel barrier decreases with decreasing s (Fig. 2.10). B is proportional to the local

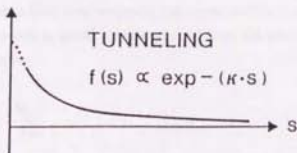


Fig. 2.10 Interaction in tunneling.

density of states involved in the tunneling process, which are selected by the voltage applied between probe tip and object, *i.e.*, the sample's occupied states when the electrons tunnel out of the sample, the empty states when they tunnel into it. B and κ are the local electronic sample properties of interest in an STM investigation. For metallic densities, $I \cong 1$ nA for $s \cong 6 \text{ \AA}$, $\bar{\phi} \cong 5$ eV and $V = 1$ V.

2.2.3 Free-Electron Model

There are several model calculations (Baratoff [Ref. 27], Garcia *et al.* [Ref. 28], Tersoff and Hamann [Ref. 23], Stoll *et al.* [Refs. 24, 25]). The first two relied on a perturbation approach to tunneling, whereas the latter two consider the transmission of plane waves through a rectangular potential barrier with corrugated boundaries. The former approach is in principle better suited for treating real surfaces and for making contact with the electronic structure of specific materials. The latter one has the advantage of being more direct and transparent, and is not restricted to low transmissivity. In particular, valuable insight into the principle and resolution of STM can be gained since the spatial distribution of the current density can be computed and displayed explicitly. The dependence of Eq. 2.40 is obtained in both of latter two. Here, we introduce Stoll's model.

Their purpose is to elucidate general features and trends of tunneling between a fine tip and a periodic sample surface. To simplify matters they consider a potential barrier of constant height U between periodically corrugated metallic electrodes, which are treated as free-electron metals. Furthermore the temperature is assumed so small that for all practical purposes all states below the Fermi energy E_f are occupied and those above E_f are empty. For a sufficiently small applied voltage V between the tip and the sample, the change in the potential is negligible, and the net tunneling current arises from states within an effective energy window where $eV \ll E_f$ near E_f . Adopting the same way introduced by Garcia *et al.* [Ref.28], the tip is replaced by an array of tips whose period is a multiple of the fundamental periodicity of the sampled surface [see Fig. 2.11]. For a sufficiently large period of the array, the calculated conductance per supercell approximates well that associated with a single physical tip. This formal trick transforms the problem into that of scattering and transmission of plane waves incident on a periodically modulated slab, a slight generalization of diffraction by a corrugated hard wall, a time-honored problem for which several numerical methods of solution have been proposed and compared [Refs. 29, 30].

Considering first the situation in which electrons tunnel from the sample into the tip(s), for each incident plane wave we assume

$$E(k_x) = \frac{(\hbar k_x)^2}{2m} = E_f = \frac{(\hbar k_f)^2}{2m} \quad (2.44)$$

where m is the electron mass. To keep the notation simple, both metals are assumed identical. As in standard surface scattering problems [Ref. 29] the wavevector k_x of the incident wave is split

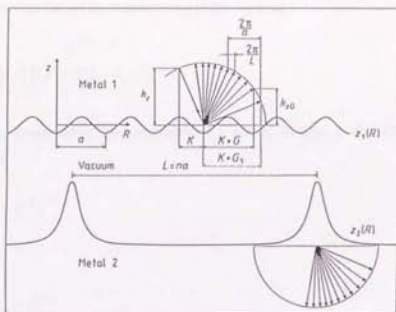


Fig. 2.11 Geometry of the two-dimensional corrugated sample and tip array with boundaries $z = z_{1,2}(R)$, and wavevectors of the incident, reflected and transmitted plane waves. From [Ref. 24].

into components parallel and perpendicular to the surface

$$\vec{k} = (K, k_z) \quad (2.45)$$

Thus the incident wave (normalized per unit volume) is

$$\psi_i(r) = \exp[i(KR - k_z z)] \quad (2.46)$$

As illustrated in Fig. 2.11, an infinite set of scattered or reflected waves, labeled by the reciprocal-lattice points G , is generated

$$\psi_s(r) = \sum_G A_G \exp\{i[(K+G)R + k_{zG} z]\} \quad (2.47)$$

The total wavefunction $\psi = \psi_i + \psi_s$, must be matched to the appropriate solution in the barrier region, which is conveniently represented as

$$\psi_b(r) = \sum_G [\alpha_G^- \exp(-\kappa_G z) + \alpha_G^+ \exp(\kappa_G z)] \exp[i(K+G)R] \quad (2.48)$$

Similarly we can describe the waves transmitted into the tip array

$$\psi_t(r) = \sum_G C_G \exp\{i[(K+G)R - k_{zG}z]\} \quad (2.49)$$

To guarantee energy conservation the components k_{zG} and κ_G in Eqs. 2.47-2.49 must satisfy the following conditions

$$k_{zG} = [k_r^2 - (K+G)^2]^{1/2} \quad (2.50)$$

and

$$\kappa_G = [\kappa_0^2 + (K+G)^2]^{1/2} \quad (2.51)$$

where

$$\kappa_0^2 = \left(\frac{2m}{\hbar^2}\right)(U - E_r) \quad (2.52)$$

The assumption of a step-like change in the potential at the electrodes leads to the condition that the wavefunction and its derivative normal to the surfaces, defined by

$$z = z_j(R) \quad j = 1, 2 \quad (2.53)$$

must be continuous. These conditions lead to the following equations

$$W_{RG}^{(1)} A_G + E_R^{(1)} = M_{RG}^{(1)} \alpha_G \quad (2.54)$$

$$W_{RG}^{(2)} C_G = M_{RG}^{(2)} \alpha_G \quad (2.55)$$

where summation over repeated indices is implied, and the matrices $M^{(j)}$ and $W^{(j)}$ and the vectors $E^{(j)}$ and α are defined in the following way

$$M_{RG}^{(j)} = \exp(iRG) \begin{pmatrix} \exp(z_j \kappa_G) & \exp(-z_j \kappa_G) \\ \exp(z_j \kappa_G)(i\kappa_G/k_z) & -\exp(-z_j \kappa_G)(i\kappa_G/k_z) \end{pmatrix} \quad (2.56)$$

$$W_{RG}^{(j)} = \exp\left[i\left(RG \pm z_j k_{z0}\right)\right] \begin{pmatrix} 1 \\ \mp k_{z0}/k_z \end{pmatrix} \quad (2.57)$$

with the upper(lower) sign referring to $j = 1(2)$ and

$$E_R^{(j)} = \exp(\mp iz_j k_z) \begin{pmatrix} 1 \\ 1 \end{pmatrix} \quad \alpha_G = \begin{pmatrix} \alpha_G^+ \\ \alpha_G^- \end{pmatrix} \quad (2.58)$$

The equations describing tunneling from the tip array into the sample are obtained by changing the signs in front of k_z and k_{z0} , and interchanging 1 and 2 in the above equations.

For computational purposes the sums in Eqs. 2.47-2.49 are truncated, e.g., only a finite number of waves with $|G| \leq 2\pi N_G/L$ are kept, resulting in there being $N = 2N_G + 1$ independent coefficients of each type (A_G , α_G^+ , α_G^- , C_G). The basic idea of the so-called GR-method is to impose Eqs. 2.54, 2.55 at N regularly spaced collocation points inside the supercell.

Returning to Eqs. 2.54, 2.55, where $M^{(0)}$ and $W^{(0)}$ are now $2N \times 2N$ and $2N \times N$ matrices, respectively, one may consider them as a system of linear equations for the $4N$ unknown coefficients or, alternatively, first eliminate α_G . We then solve the system

$$\begin{pmatrix} W_{RG}^{(1)} & -M_{RG}^{(1)}(M^{(2)})^{-1}GR W_{RG}^{(2)} \end{pmatrix} \begin{pmatrix} A_G \\ C_G \end{pmatrix} = -E_R^{(1)} \quad (2.59)$$

and can compute α_G , if desired, from

$$\alpha_G = (M^{(2)})^{-1}GR W_{RG}^{(2)} C_G \quad (2.60)$$

2.2.4 Operating Mode

Tracing the contours of constant interaction intensity with the probe tip is so far the easiest and most widely used control and imaging mode. It produces a "constant interaction surface". In this mode, the deviation from a set interaction intensity is corrected by constantly adjusting the separation of tip and sample *via* a feedback system. In STM, this is called the "constant current mode" [see Fig. 2.12(a)]. In region A, the interaction is homogeneous and the tip trace corresponds to the surface topography up to resolution broadening. In B, an inhomogeneity in the interaction changes the tip trace accordingly. In C, the local property is affected by the proximity of the tip. Shown is the effect of an elastic response of the object surface to an attractive force between the tip and the object, which induces a reversible change of the surface geometry. Effects of possible tip-surface interactions on the imaging should always be given due consideration.

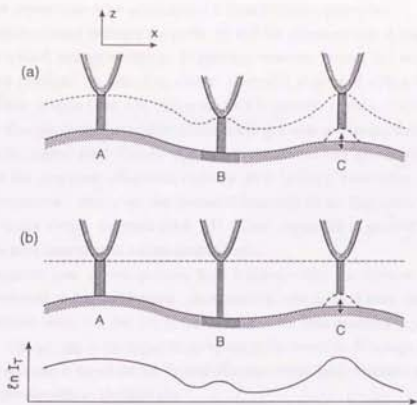


Fig. 2.12 (a) Constant current and (b) constant height mode. From [Ref. 26].

The imaging speed is limited by the motion of the probe tip in vertical or z -direction. This motion should only have frequency components smaller than the mechanical resonance frequency of the mechanical path connecting the probe tip and the sample. For a resonance frequency of 5 kHz and a pixel size of 1 Å, the scan speed should be considerably less than 5000 Å/sec.

The imaging speed can be increased substantially by keeping the z -position of the probe tip constant and recording the change in intensity [Ref. 31] [see Fig. 2.12(b)]. In practice, the time constant of the feedback loop is made sufficiently long or, if the relative z -position of the tip and the sample remains stable in time, the feedback loop is disabled. The limiting factor is then the scan frequency. This is called "constant height mode". It has to be applied to relatively flat parts of a sample due to the limited dynamic range of the control electronics. For instance, four orders of magnitude in the tunnel current at a tunnel barrier height of 2 eV allow maximal height differences of about 6 Å. Constant height images give a qualitative topography, for conversion to a quantitative topography the detailed distance dependence of the interaction is required, which is not known *a priori*.

Of prime importance in microscopy are the lateral and, for topographic structures, also the vertical sizes of specific features. They are obtained from the calibrated displacements of the probe. However, the absolute probe-object distance, s , is required when carrying out deconvolution procedures, since the lateral resolution depends s . In other experiments, such as those aimed at the

general distance dependence of an interaction, s is even a primary parameter.

In one approach, contact between the probe tip and the object surface is taken as $s = 0$. This seems straightforward and quite natural. In practice, however, contact is a rather delicate and not well understood problem. In tunneling, contact is usually associated with a discontinuity in the current vs. distance relation [Ref. 32]. Since such a discontinuity is not accounted for by theory, it is associated with a mechanical instability due to rearrangements or displacements of the probe and object atoms in the contact area. The discontinuity at contact can vary appreciably, from less than a factor of two in the current on clean metal surfaces [Ref. 32] up to two orders of magnitude in an electrolytic environment. Moreover, the predicted flattening of the $I(s)$ curve in the 2 Å region before contact is not always observed [Ref. 33]. Thus, contact is in practice a somewhat fuzzy concept, at least experimentally on a subangstrom scale.

A second approach uses an extrapolation from a region where the distance dependence of the interaction is believed to be well known. In tunneling, one method uses the field emission or Gundlach resonance [Refs. 14, 34, 35] or the fact that in the field emission regime, $I \sim \exp(-\phi^{3/2}/E)$, where $E = V/s$, as long as the radius of curvature of the tunnel tip R is large compared to s .

Still another estimate is based on the Tersoff-Hamann model and compares a measured surface corrugation amplitude with a calculated one.

2.2.5 Imaging

An image closest to the topography or geometrical structure is obtained as a constant interaction surface, provided the interaction itself and the response of the object to it are homogeneous. This is usually the case for clean metallic surfaces. On electronically inhomogeneous surfaces, the central task is to separate the inhomogeneity effects, like those at B and C in Fig. 2.12, from geometric features. In STM of clean metal surfaces, the constant interaction surface reflects the surface structure. In many others, however, the variations in the interaction dominate the image contrast. It is the local electronic properties contained in B and κ of Eq. 2.42, which make the interaction inhomogeneous. The imaging methods concerned with B and κ are STS with its variations and work-function profiles.

2.2.6 Spectroscopy

STS is concerned with the local density of electronic states, which appears in the prefactor B of Eq. 2.42. The electronic states of interest are selected by the voltage applied between the tip and the sample. A certain "course selection" is made by the energy dependence of the tunneling probability as shown in Fig. 2.13. The simplest type of STS consists of taking two constant current images at reversed polarity [Ref. 36]. We then obtain an image each of predominantly occupied and empty states, respectively. In the case of GaAs, As appears in the image of the occupied states, Ga in

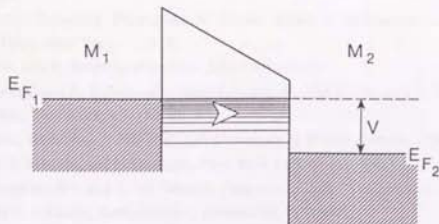


Fig. 2.13 Tunneling transmission is highest between occupied states at E_{F1} and the empty states at $E_{F2} + V$. From [Ref. 26].

those of the empty states. In a second mode, images taken at different voltages are compared, where the voltages are chosen such that specific electronic features are particularly evident in the corresponding constant current images [Ref. 37].

An elegant variation of this approach is the current imaging tunneling spectroscopy (CITS) [Ref. 38]. There, the z -position of the tip is controlled in the constant current mode at a set current and voltage I_0 and V_0 , respectively. The control is disabled intermittently to record I - V curves at every pixel. Besides the constant current image at V_0 , a series of images of I - I_0 at V - V_0 are obtained, which should exhibit the relevant electronic features. The art of the method consists of choosing V_0 such that the constant current image is electronically as homogeneous as possible. Hess *et al.* observed the superconducting vortices in 2H-NbSe₂ with this technique [Ref. 39].

The classical way of performing STS entails measuring dI/dV (or better $d(\ln I)/d(\ln V)$ for normalizing purposes) simultaneously with the topographic mode so as to obtain the local density of states at an energy $E_F \pm V$, depending on polarity, and at a distance from the surface given by the set current and the set voltage [Refs. 31, 40-42].

Finally, we call a special mode of CITS, which we developed, as AST (atomic site tunneling spectroscopy). The uniqueness of the AST technique is that the tunneling spectra are all taken at various positions predetermined optionally during a single scan of atomic imaging. Therefore, once a shot of STM image is observed, we have a number of tunneling spectra of which measuring positions are known on the image taken simultaneously with an atomic scale. In the case that the specimen has the spatial variation of local electronic structure in an atomic scale, this technique becomes a powerful tool to detect it. Hasegawa *et al.* have already showed such kind of observation on the b - c plane of a Bi₂Sr₂CaCu₂O₈ single crystal [Ref. 43].

References

- [1] E. O. Kane, *Tunneling Phenomena in Solids*, edited by E. Burstein and S. Lundqvist, Plenum Press, New York, 1 (1969).
- [2] I. Giaever, and K. Megerle, *Phys. Rev.* 122, 1101 (1961).
- [3] R. Meservey, and B. B. Schwartz, *Superconductivity Vol. 1*, edited by R. D. Parks, Marcel Dekker Inc., New York, 117 (1969).
- [4] S. Bermon, *Tech. Rep. 1, NSF-GP1100*, University of Illinois, Urbana, (1964).
- [5] J. Nicol, S. Shapiro, and P. H. Smith, *Phys. Rev. Lett.* 5, 461 (1960).
- [6] D. H. Douglass, Jr., and L. M. Falicov, *Progress in Low Temperature Physics Vol. 4*, Edited by C. J. Gorter, North-Holland, Amsterdam, 97 (1964).
- [7] B. N. Taylor, E. Burstein, and D. N. Langenberg, *Bull. Am. Phys. Soc.* 7, 190 (1962).
- [8] R. C. Dynes, V. Narayanamurti, and J. P. Garno, *Phys. Rev. Lett.* 41, 1509 (1978).
- [9] B. L. Blackford, and R. H. March, *Can. J. Phys.* 46, 141 (1968).
- [10] S. B. Kaplan, C. C. Chi, D. N. Langenberg, J. J. Chang, S. Jafarey, and D. J. Scalapino, *Phys. Rev. B* 14, 4854 (1976).
- [11] R. C. Dynes, and J. M. Rowell, *Phys. Rev. B* 11, 1884 (1975).
- [12] G. Binnig, H. Rohrer, C. Gerber, and E. Weibel, *Phys. Rev. Lett.* 49, 57 (1982).
- [13] G. Binnig, and D. P. E. Smith, *Rev. Sci. Instrum.* 57, 1688 (1986).
- [14] G. Binnig, and H. Rohrer, *Helv. Phys. Acta* 55, 726 (1982).
- [15] D. W. Pohl, *Rev. Sci. Instrum.* 58, 54 (1987).
- [16] C. Gerber, G. Binnig, H. Fuchs, O. Marti, and H. Rohrer, *Rev. Sci. Instrum.* 57, 221 (1986).
- [17] W. J. Kaiser, and R. C. Jaklevic, *Surf. Sci.* 181, 55 (1987).
- [18] J. E. Demuth, R. J. Hamers, R. M. Tromp, and M. E. Welland, *IBM J. Res. Develop.* 30, 396 (1986).
- [19] B. Michel, and G. Travaglini, *J. Microscopy* 152, Pt. 3, 681 (1988).
- [20] D. W. Pohl, *Europ. Patent Nr.* 0247219.
- [21] T. R. Albrecht, S. Akamine, M. J. Zdeblick, and C. F. Quate, *Proceedings Fourth International Conference on STM, Oarai, Japan 1989*.
- [22] K. H. Besocke, M. Teske, and J. Frohn, *Surf. Sci.* 181, 145 (1987).
- [23] J. Tersoff, and D. R. Hamann, *Phys. Rev. Lett.* 50, 1988 (1983).
- [24] E. Stoll, A. Baratoff, A. Selloni, and P. Carnevali, *J. Phys. C* 17, 3073 (1984).
- [25] E. Stoll, *Surf. Sci.* 143, L411 (1984).
- [26] H. Rohrer, *Scanning Tunneling Microscopy and Related Methods*, Edited by H. Rohrer, Kluwer Academic Publishers, Dordrecht/Boston/London, 1 (1990).
- [27] A. Baratoff, *Europhys. Conf. Abstracts* b 7, 364 (1983).
- [28] N. Garcia, C. Ocal, and F. Flores, *Phys. Rev. Lett.* 50, 2002 (1983).
- [29] N. Garcia, J. Ibanez, J. Solana, and N. Cabrera, *Surf. Sci.* 60, 385 (1976).
- [30] N. Garcia, and N. Cabrera, *Phys. Rev. B* 18, 576 (1978).

- [31] G. Binnig, and H. Rohrer, IBM J. Res. Develop. 30, 355 (1986).
- [32] J. K. Gimzewski, and R. Möller, Phys. Rev. B 36, 1284 (1987).
- [33] U. Dürig, O. Züger, and D. W. Pohl, J. Microscopy 152, 259 (1988).
- [34] G. Binnig, K. H. Frank, H. Fuchs, N. Garcia, B. Reihl, H. Rohrer, F. Salvan, and A. R. Williams, Phys. Rev. Lett. 55, 991 (1985).
- [35] R. S. Becker, J. A. Golovchenko, and B. S. Swartzentruber, Phys. Rev. Lett. 55, 987 (1985).
- [36] R. M. Feenstra, and A. P. Fein, Phys. Rev. B 32, 1394 (1985).
- [37] R. Wolkow, and Ph. Avouris, Phys. Rev. Lett. 60, 1049 (1988).
- [38] R. J. Hamers, R. M. Tromp, and J. E. Demuth, Phys. Rev. Lett. 56, 1972 (1986).
- [39] H. F. Hess, R. B. Robinson, R. C. Dynes, J. M. Volles, and J. V. Waszczak, Phys. Rev. Lett. 62, 214 (1989).
- [40] R. S. Becker, and J. A. Golovchenko, Phys. Rev. Lett. 55, 2032 (1985).
- [41] N. D. Lang, Phys. Rev. B 34, 5947 (1986).
- [42] J. Ihm, Physica Scripta 38, 269 (1988).
- [43] T. Hasegawa, and K. Kitazawa, Jpn. J. Appl. Phys. 29, L434 (1990).

Chapter 3

Experimental

3.1 Design of Cryogenic STM

3.1.1 Hardware

Cryogenic STM apparatuses developed by a number of groups can be roughly divided into two types. One approach to building a cryogenic STM system is to reform an usual ultrahigh vacuum (UHV) type STM for the operation at cryogenic temperature [Refs. 1-6]. The other is to design a special type of STM which can be dipped into a liquid He storage Dewar [Refs. 7-13]. The former type allows an observation in UHV, so that a good surface condition of a specimen can be obtained relatively easily. Since the same ways of approaching and vibration isolation are available, the developmental efforts can be focused on how to cool the STM unit and prevent the sample surface from adsorption. This way seems to be ideal except a heavy cost. The latter type allows cooling the whole system down to 4.2 K (or below by pumping) by steeping it in liquid He. By using a superconducting magnet, an observation under high magnetic field is possible. It is one of the advantages of this way that the expenses can be cut down. However, this needs special design which is completely different from ordinary STM apparatuses. We chose the second way.

Three facts which stand in the way of the development of cryogenic STM are cited as follows:

- 1) Thermal expansion and contraction of the STM unit.
- 2) Limited space for vibration isolation in the insert chamber.
- 3) Decrease of the piezoelectric coefficient at cryogenic temperature.

When we use the STM in the temperature range between liquid He temperature (4.2 K) and room temperature, *i.e.*, temperature difference of about 300 degrees, thermal expansion and contraction of the STM unit become a problem. If the STM unit is composed of materials which have various thermal expansion coefficients spreading over a wide range, it may be destroyed by striction. Since thermal drift of 1 Å of the distance between a probe tip and a sample changes the order of tunneling current, the demand for the stability of the temperature during the measurement is very strict. Therefore, we should use materials whose thermal expansion coefficients are small, and make the STM unit as small as possible, and design it to be a symmetric shape which cancels *x-y* drift.

In the narrow space of the insert chamber, it is difficult to provide a sufficient vibration isolation system. In order to make the STM unit itself have resistance against mechanical noises such as an acoustic wave and vibration of the building, it is effective to raise the resonance frequency of the unit higher than noise frequencies by making it small and rigid.

At 4.2 K, the piezoelectric coefficient of the PZT material, which is a component of the scanner, decreases to about 1/10 of that at room temperature. Accordingly, at cryogenic temperature, it becomes difficult to reduce the tip-sample distance within the tunneling region avoiding a crash. Possible methods to cope with this problem are to adopt a PZT material whose piezoelectric coefficient is large, and to provide a system which magnify the movement of the PZT, *e.g.*, a mechanical lever, and to make one approaching step shorter than usual.

We had built our first STM using the same method as originally presented by Smith and Binnig [Ref. 7]. With this STM, Hasegawa *et al.* got tunneling spectra which showed superconducting gap dimly on the cleaved surface of $\text{Bi}_2\text{Sr}_2\text{CaCu}_2\text{O}_y$ [Ref. 14], but no atomic resolution images were obtained. The approaching system using a spring and a flexible sample holder did not work reproducibly but caused z -drift. The adjustment operated by hand almost could not escape from collision between the tip and the sample. The single copper tube in which the STM unit was fixed was sensitive to bubbling of liquid He, and easy to propagate the vibration. We reformed it and built new machines several times, and finally we reached a system which is quite different from the original one. Figs. 3.1 and 3.2 show the current cryogenic STM system.

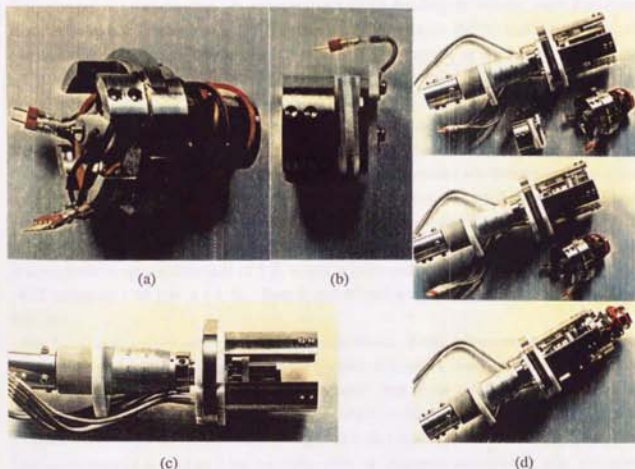


Fig. 3.1 Cryogenic STM unit (airtight type).

A scanner is composed of four piezoelectric rods, which are arranged almost like the tube scanner [Ref. 15], and a tip holder on the top of them [Fig. 3.1(a)]. The piezoelectric rod employed is a special type which is formed by piling small chips of PZT (Tokin Corporation, NLA 2×3×18), and has very large piezoelectric coefficient of 1200 Å/V. It has the maximum applied voltage value of 130 V, which allows maximum expansion of 1.56 μm even at 4.2 K. The tip holder is insulated from PZT's with MACOR to cut off the electric signal applied on PZT's during the scanning. All higher voltage electrodes of the four piezoelectric rods are connected to the longitudinal z-drive, and two lower voltage electrodes of one and adjacent PZT's are connected to the lateral x- and y-drives, and the other two to the ground. In the z-axis motion, all the PZT's move. In order to scan, two PZT's corresponding to the x- and y-axes expand and contract, and a probe tip mounted on the holder moves like nodding. With this scanner, we obtain a wide scanning area more than 1.5×1.5 μm even at 4.2 K, which is sufficient for the observation of a macro-scale structure.

The scanner is fixed on the 3D stage with which the tip position can be adjusted easily. Moreover, the x-stage can be moved by using a worm gear and a rotary shaft driven by a stepper motor even during the measurement, and we can change an observed area with a large distance. This allows us to find a suitable area of the sample surface to observe and increases the probability of success per one measurement. In addition to the PZT's building the scanner, extra four outer piezoelectric rods connected to a DC bias are provided. These PZT's make it possible to compensate for a large tip-sample distance change due to thermal or mechanical drift in the z-direction, by using them manually. It is also desirable to use these PZT's to make the tip take refuge when the mechanical systems, which cause vibration, are working.

Fig. 3.1(b) shows a sample holder. A specimen is nipped between an electrode and a glass plate pushed by a spring. This sample holder is fixed on a spindle of a micrometer head [Fig. 3.1(c)]. We adopt a differential type micrometer head using two screws which have different but very close pitches (Mitsutoyo Corporation, MHP2-2.5). A 360 degree rotation of a handle gives 50 μm linear motion of the spindle. The handle is driven by a stepper motor *via* a rotary shaft. The stepper motor has harmonic gears and 0.0036 degree steps. Finally, this mechanical approaching system gives a calculative approaching step of 5 Å, which is much smaller than the maximum span of the z-PZT motion of 1.56 μm at 4.2 K. Even if this did not work as we calculate, it seems to be sufficient.

Fig. 3.1(d) indicates the setting procedure of the STM unit. Finally, the scanner and the sample holder are covered with a tube, and the unit itself works as a airtight chamber. There is a hole for gas exchange beside the micrometer head, and a valve fixed at the spindle closes or opens the airtight chamber. This airtight structure is designed in order to observe chemically unstable materials. Some of the HTSC materials are degraded if they are exposed to the air. H₂O and CO₂ in the air are thought to react on these materials. After the exposure, an insulating shell is formed and an STM observation becomes almost impossible. With this airtight unit, we can observe these unstable specimens with the following procedure.

- 1) Set a specimen in a glove box filled with inert gas.

- 2) Close the airtight unit in the glove box.
- 3) Fix the unit in the insert chamber [see Figs. 3.2(a) and 3.2(b)].
- 4) Evacuate the insert chamber with a rotary pump.
- 5) Open the airtight unit and evacuate it.
- 6) The insert chamber and the airtight unit are filled with thermal exchange gas (He).
- 7) Dip the insert chamber in the liquid He storage Dewar to cool it down to 4.2 K.

By following this procedure, the specimen can be subjected to a cryogenic observation without exposure to air. It is well known that the depletion of the surface oxygen occurs if the HTSC material is stored in an UHV chamber. Edwards *et al.* reported that they obtained atomic resolution on a $\text{YBa}_2\text{Cu}_3\text{O}_7$ single crystal after cleavage at 20 K, and if they raised the temperature higher than 60 K, they could not get a clear atomic image [Ref. 16]. This result is consistent with the results of photoemission spectroscopy (PES) [Refs.17, 18]. With our airtight unit, we have to neither expose the specimen to air nor store it in UHV. Therefore, we believe, our method is superior to UHV STM systems as long as this problem is concerned.

For vibration isolation, the Dewar is put on a platform of an air damper which is supported by four pneumatic vibration isolation legs, and the STM unit is suspended by three springs inside the insert chamber (see Fig. 3.2). During the approaching process using the micrometer head, the STM unit is locked between an upper stationary ring and a lower movable stage which is pushed by

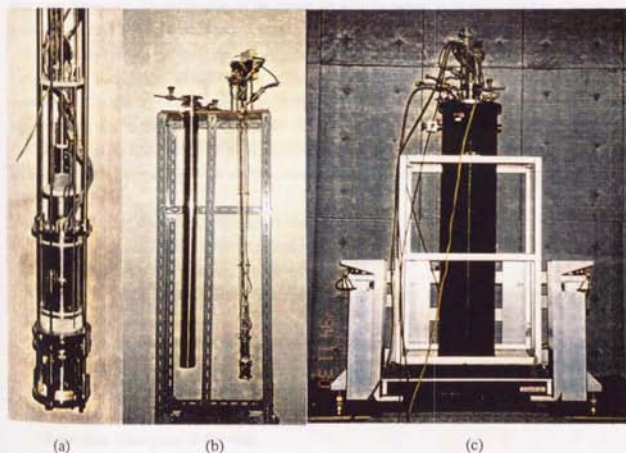


Fig. 3.2 Cryogenic STM apparatus.

a micrometer head. After the adjustment of the tip position, the probe tip is brought far from the sample surface by expanding the outer piezoelectric rods for manual use, and the stage is moved down by the micrometer head driven by a stepper motor *via* gears and a rotary shaft. After the STM unit is completely released, the probe tip is carried into the tunneling distance again, and then, we start to measure.

3.1.2 Probe Tips

A probe tip is one of the most important parts of an STM apparatus, because it is a key to whether atomic resolution is achieved or not. Generally, mechanically ground or chemically etched wires (W, Pt, *etc.*) are used for STM. Although the probe tip still remains a mysterious part of STM, recent calculations conclude that a normal atomic image reflecting real atomic arrangement can not be obtained unless the end of the tip has a single atom, and that an atomic image is distorted when the tip is out of perpendicular to the sample surface [Refs. 19-25]. In practice, we often experienced that the atomic images observed on the same material varied with distortion depending on the measurements. Comparing with these experiences, the conclusions of the calculations seem to be worth believing. One group, which insists significance of estimating the state of the tip, realizes the single atom tip by using field ion microscope (FIM) [Refs. 26-30]. Now, this is a very rare case, however, the estimation of the probe tip may be going to be demanded as evidence for reliability of the STM data in the near future.

At the early period of this study, we employed mechanically ground $Pt_{0.9}Ir_{0.1}$ tips (Digital Instruments, Inc.), but did not obtain sufficient reproducibility from the viewpoint of atomic resolution. Therefore, we use chemically etched tips which we make by ourselves now. W or Au wire of 0.3 mm in diameter is employed for this purpose. We prepare KOH (1 mol/l) or $CaCl_2/HCl$ ($CaCl_2$ 220 g, HCl 40 ml/l) distilled water solution and use Pt wire or carbon rod as a counterelectrode for making W or Au tips, respectively. The etching process is the same for both materials, as follows:

- 1) Pour 50 ml of the solution into a very clean beaker.
- 2) Insert the counterelectrode into the beaker.
- 3) Submerge the wire 1 mm into the solution.
- 4) Adjust the Variac Auto Transformer for 35 V, and with it off, connect one output to the electrode.
- 5) Connect the other output of the Variac to the wire.
- 6) Turn on a Variac and etch the wire. While the tip is etching, the solution will bubble violently, and the end of the wire will glow.
- 7) The wire will be constricted just below the surface of the liquid, and this part will be etched faster than other parts of the wire.
- 8) The constricted part will begin to glow. Stop etching when the glow becomes bright, *i.e.*, the constriction becomes narrow.

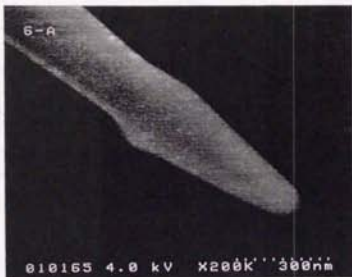


Fig. 3.3 FE-SEM picture of an electrolytically etched Au tip for STM.

- 9) Reduce the Variac lower than 1 V and turn on it and re-etch the wire observing with an optical microscope. Continue to etch the wire until the constriction becomes very narrow.
- 10) Repeat turning on and off the Variac, and stop it when the wire is cut at the constriction and the end drops.
- 11) Rinse the tip with the distilled water.
- 12) Dip the tip into acetone and clean it by using ultrasonic waves.

By this method, we can make a tip whose end has a radius of 600 \AA reproducibly, as shown in a field emission scanning electron microscopy (FE-SEM) picture (Fig. 3.3). It takes 3-5 minutes to prepare one tip. We can also make $\text{Pt}_{0.9}\text{Ir}_{0.1}$ tips with this technique, but it takes more than 10 minutes and the tips obtained tend to have ends of larger radii. Therefore the Au tip is the best because of its sharpness and chemical stability. The end of the W tip is thought to be covered with an oxide or hydroxide layer. In this case, the presence of the surface states may cause resonant tunneling, and the tunneling spectrum possibly does not reflect intrinsic nature of the specimen [Refs. 31-33]. Hence we should be very careful with W tips, which probably need after treatment, e.g., baking in UHV, to obtain intrinsic data.

3.1.3 Electronics

Fig. 3.4 shows a diagram of the whole STM system. The tunneling current which flows between the tip and the sample is picked up and amplified by a preamplifier, and the current signal is transformed into a voltage signal. The main electronics is an analog feedback circuit composed of a series of operational amplifier IC's (Fig. 3.5). We built this main electronics based on the

method originally presented by Park and Quate [Refs. 34, 35]. The tunneling signal (J) is compared with a reference voltage manually determined (V_0) by AD524. The difference is amplified by another AD524 via an RC filter and applied to the higher voltage electrodes of the z-PZT's (V_z) via a high voltage power supply, which makes the z-PZT's move to keep the tunneling current constant. A computer generates x , y scanning signals, which is applied to the lower voltage electrodes of the x -, y -PZT via a computer interface which provides digital to analog (D/A) converters. During the scanning, an analog to digital (A/D) converter takes the z -data into a memory buffer, and a CPU transfers the z -data into a main memory and display it on a screen.

There are two modes of data acquisition. The first mode is to take data from the output of the first AD524 by monitoring the variations in the tunneling current, while we scan at high speed with slow feedback. In the second mode we take data after RC filtering to record the actual tip displacements, while we scan slowly with fast feedback. The first mode and the second one generally correspond to the constant height mode and the constant current mode discussed in Chapter 2, respectively. An image can be taken in a short time using the first method, where the thermal drift and vibration problems are not significant. This method can be used when the sample is atomically flat so that there is no danger of bumping the tip, and graphite is the only material whose atomic images can be obtained with this method as far as we tried. In the second mode, we can take atomic images of all materials if their surface conditions are good, but we have to provide environment of low vibration and stable temperature.

When we measure a tunneling spectrum, the feedback loop is opened by a switch IC (Q1 in Fig. 3.5) and a condenser holds the output voltage applied to the z-PZT's (V_z) for several ms. During this period, I - V characteristics can be measured by changing the voltage between the tip and the specimen and recording the variations of the tunneling current. A tunneling spectrum (dI/dV - V curve) is obtained if we calculate differential conductance (dI/dV) value for each voltage (V) over the measuring voltage range based on the I - V curve. We found that this calculation method gives the same result as the direct measurement of the dI/dV - V characteristics by using lock-in technique. We adopt this method because of simplicity.

3.2 Sample Preparation

3.2.1 Crystal Structures and Electronic Natures of HTSC's

Generally, HTSC's have perovskite-like layered structures composed of several kinds of layers which contain CuO_2 sheets of corner-linked square-plane coordinated copper and oxygen atoms, and the other spacer atom layers interleaving the CuO_2 sheets. Figs. 3.6(a) and 3.6(b) indicate the crystal structures of $\text{Bi}_2\text{Sr}_2\text{CaCu}_2\text{O}_y$ (BSCCO) and $\text{YBa}_2\text{Cu}_3\text{O}_y$ (YBCO), respectively. In real crystals, the oxygen atom has nonstoichiometry and the spacer atoms, which range from Ca, Sr, and Ba, to Y and the rare earths, have cation disorder. BSCCO has incommensurate modulation

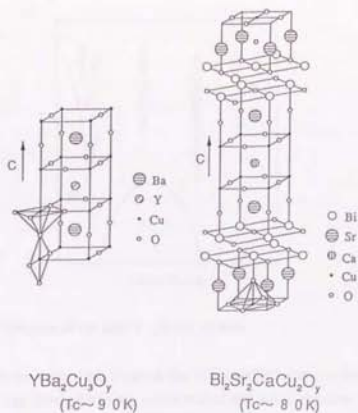


Fig. 3.6 Crystallographic structure of BSCCO and YBCO.

structure along the b -axis whose periodicity corresponds to about 4.8 times the b -spacing [Refs. 36-38]. The Bi-O3 bond, which joins adjacent sheets in the Bi_2O_3 bilayer, is long and weak. This weak bond parallel to the c -axis results in very weak interlayer bonding and mica-like mechanical behavior, which allow cleavage of the crystal. The specific feature of the YBCO system is the existence of one dimensional CuO chain layers which do not have oxygen between Cu atoms in the a -direction but have in the b -direction. Owing to this CuO chain layer, YBCO has the orthorhombic phase (Ortho I) with large oxygen content. As the oxygen content decreases, the orthorhombic superstructure phase (Ortho II), in which oxygen is completely absent from every second CuO chain, appears, and finally it changes to a non-superconducting tetragonal phase [Refs. 39-42].

Fig. 3.7 shows a general electronic phase diagram of the HTSC. It is widely believed that the CuO_2 network is the principal site of electronic activity of this system. At the left end of this diagram, copper ions in the CuO_2 sheets are in a Cu^{2+} valence state with a $\text{Cu}3d^9$ electronic configuration which corresponds to a half-filled $d_{x^2-y^2}$ band. Although the system is expected to be a metal at this carrier density, the real material, e.g., La_2CuO_4 , turns out to be an insulator with long-range antiferromagnetic order. This insulating nature of the undoped system is understood as a result of strong electron correlation on the Cu sites of the CuO_2 network. A strong on-site Coulomb repulsion U leads to splitting of the band into an upper and a lower Hubbard band as

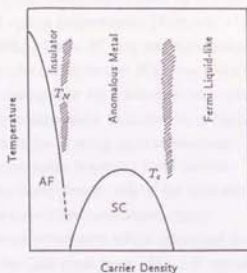


Fig. 3.7 Model phase diagram of the high T_c cuprate system.

shown in Fig. 3.8(a). In the case of the cuprates, the O2p band is located in the Mott-Hubbard gap owing to the atomic energy level proximity, which makes the actual situation more complicated. The Fermi level lies in the energy gap between the O2p band and the upper Hubbard band of Cu3d character. Therefore, the lowest electronic excitation energy Δ is charge transfer from the occupied O2p band to the empty Hubbard band [Fig. 3.8(b)]. This is categorized in the charge transfer type insulator according to the Sawatzky-Allen-Zaanen scheme [Refs.43, 44]. Charge carriers are introduced into the parent material by doping. Hole carriers are doped by cationic substitution or by oxygen intercalation. Even a relatively small number of holes destroy the antiferromagnetic long

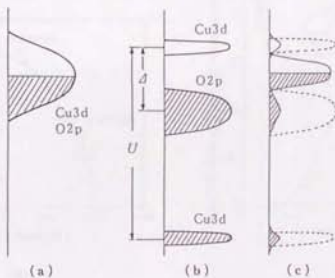


Fig. 3.8 Models of the electronic structure of the CuO_2 plane. (a) Band model. (b) Mott-Hubbard insulator. U : Mott-Hubbard gap, Δ : charge transfer gap. (c) Reconstruction of the band structure. In-gap states are formed around the Fermi level.

range order, although strong spin correlation remains up to high doping levels [Ref. 45]. It was elucidated by the results of optical measurements [Refs. 46, 47], PES [Refs. 48, 49], electron energy loss spectroscopy (EELS) [Refs. 50, 51], and X-ray absorption spectroscopy (XAS) [Ref. 52] that hole donation causes the reconstruction of the band structure and in-gap states are formed around the Fermi level decreasing both the conduction and valence bands of the parent material [Fig. 3.8(c)]. As the hole concentration is increased, an insulator-metal transition occurs and superconductivity emerges with the T_c rising up to a maximum. With further hole doping, the T_c decreases, although the system keeps becoming more metallic. In the electronic phase diagram (Fig. 3.7), the lower (higher) carrier density side of the optimally doped composition which gives the maximum T_c is called the underdoped (overdoped) region.

BSCCO has the oxygen nonstoichiometry which determines the hole concentration in the Bi_2O_2 bilayer, and YBCO has in the CuO chain layer. Fig. 3.9 indicates the dependence of T_c on the oxygen content for BSCCO [Fig. 3.9(a)] and YBCO [Fig. 3.9(b)], respectively [Refs. 53, 54]. As shown in Fig. 3.9(a), the curve of T_c vs. hole concentration in the phase diagram of the BSCCO system can be easily fit by a parabolic curve. A universal curve, which is applicable to La, Bi and Tl superconductors, was found to be the parabola $T_c/T_c(\text{max})=1-82.6(p-0.16)^2$ where p is the number of holes per Cu [Ref. 55]. In the case of the YBCO system, the situation is more complex. There are two phases namely the 90 K and the 60 K phases, which correspond to the Ortho I and Ortho II phases described above, respectively. Therefore, the curve has a plateau as a result that it is composed of two parabolic curves contributed from the two phases [Fig. 3.9(b)].

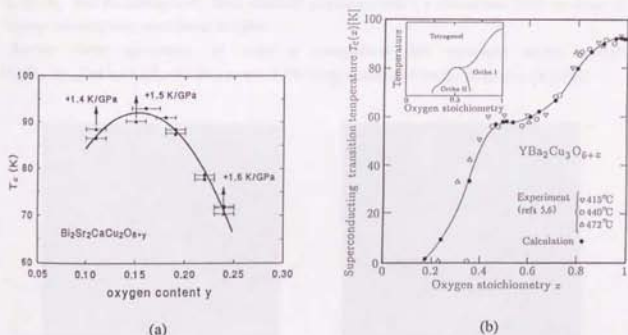


Fig. 3.9 The variation of T_c with oxygen stoichiometry for (a) BSCCO and (b) YBCO system. From [Refs. 53, 54].

3.2.2 $\text{Bi}_2\text{Sr}_2\text{CaCu}_2\text{O}_x$ Single Crystals

Single crystals of BSCCO were kindly offered by Mr. N. Motohira (Kitazawa Laboratory, University of Tokyo). They were grown by a floating zone method [Ref. 56]. Sintered feed rods were first prepared by solid state reaction using high-purity Bi_2O_3 , SrCO_3 , CaCO_3 and CuO as starting materials. A nominal composition of the rods was $\text{Bi}_{2.2}\text{Sr}_{1.8}\text{CaCu}_2\text{O}_x$. An infra-red heating furnace equipped with a double ellipsoidal mirror and two halogen lamps (Nichiden Machinery Ltd., SC15-HD) was used for the crystal growth. The growth was done at a speed of 0.5 mm/h and in the oxygen pressure of 1 atm.

One zone-melted rod, which is 7-8 mm in diameter and 60-70 mm long, is composed of a number of single crystals piling up in such direction that their c -axes are perpendicular to the rod's axis. Crystals were separated from the rods and selected under an optical microscope. They were rectangular platelets parallel to the a - b plane, while the c -axis was along the thin direction. A typical size of the crystals is $5 \times 5 \times 0.5$ mm [Fig. 3.10(b)], which is suitable for the observation on the a - b plane. These crystals were characterized by X-ray diffraction (XRD) analysis and magnetization measurement, indicating excellent quality. A BSCCO crystal has cleavage which occurs between a double BiO layer. Therefore, we can get a clean surface just before the measurement by using adhesive tape very easily.

The as-grown BSCCO crystal exhibited Meissner transition onset at 88.9 K. The oxygen content of as-grown BSCCO employed in this work is thought to be in the over doped region. In order to increase the information obtained by observations, we prepared five kinds of specimens with different oxygen contents by annealing the as-grown single crystals under high-pressure O_2 , 1 atm O_2 , air, N_2 , and Ar atmosphere. Heat treatment conditions and T_c 's determined from the onset of magnetic susceptibility were listed in Table 3.1.

Besides these specimens, to make a comparison, we measured single crystals $\text{Bi}_{1.8}\text{Pb}_{0.4}\text{Sr}_{1.8}\text{CaCu}_2\text{O}_x$ ($T_c \sim 82.9\text{K}$) in which Pb atoms substituted for the Bi sites dope holes.

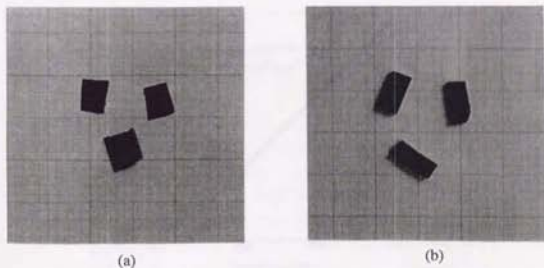


Fig. 3.10 Pictures of (a) BSCCO single crystals and (b) YBCO thin films.

specimen	atmosphere	temperature	T_c
a	200 atm O ₂	600°C, 12 h	74.5 K
b	1 atm O ₂	850°C, 30 d	83.6 K
c	1 atm air	800°C, 20 h	88.4 K
d	1 atm Ar	700°C, 7 d	86.5 K

Table 3.1 Heat-treatments and T_c values of four BSCCO specimens.

3.2.3 YBa₂Cu₃O₇ Thin Films

All the YBCO thin films employed in this work were kindly supplied by Dr. M. Kawasaki, Dr. J. P. Gong, Mr. K. Fujito, and Mr. R. Tsuchiya (Koinuma Laboratory, Tokyo Institute of Technology).

The (001) oriented YBCO films were deposited on SrTiO₃ (STO) single crystal (100) substrates by ArF excimer laser ablation from the stoichiometric target. The growth conditions were O₂ pressure between 200 and 400 mTorr, substrate temperature between 700 and 730°C, and laser fluence of 1 J/cm². The thickness of the films was between 50 and 300 nm. The as-grown films were cooled down to room temperature after annealing in an O₂ atmosphere of 700 mTorr at substrate temperature of 400°C for 30 min. Every YBCO epitaxial thin film prepared under the described condition had excellent superconducting properties with T_c of 90 K, critical current density (J_c) higher than 10⁶ A/cm² at 77 K, and normal resistivity ratio [ρ (300 K)/ ρ (100 K)] of 3 (Fig. 3.11). XRD patterns measured on these films showed a full width at half-maximum of the (005) peak as narrow as 0.11° (Fig. 3.12). Rutherford backscattering spectrometry (RBS) gave the aligned-to-random ratio χ_{min} as low as 3.5% (Fig. 3.13).

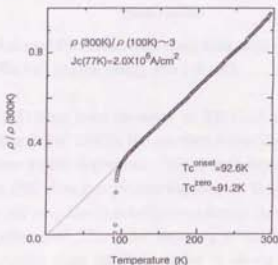


Fig. 3.11 Normalized resistivity vs. temperature curve of a YBCO film.

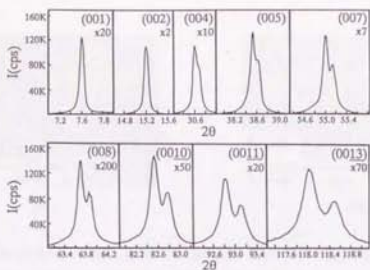


Fig. 3.12 (00 l) XRD patterns of a 300 nm thick YBCO film prepared under the conditions of substrate temperature of 725 °C, oxygen pressure of 400 mTorr, and laser fluence of 110 mJ. The substrate was SrTiO₃(100).

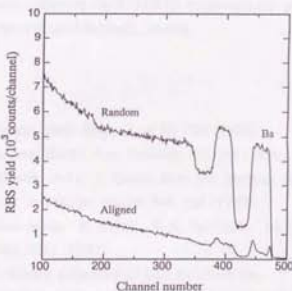


Fig. 3.13 Random and aligned RBS data of a 200 nm thick, (001) oriented YBCO film grown on SrTiO₃(100) substrate. The He⁺ incident energy was 1.5 MeV.

The (110) oriented YBCO films were deposited on STO(110) substrates. Because the c -axis length of STO is longer than that of YBCO, 100 nm thick PrBa₂Cu₃O₇ (PBCO) template layer was deposited at 600 °C before YBCO deposition. YBCO was deposited under the same growth conditions as those of the (001) film growth described above. The thickness of YBCO layer was controlled from 50 nm to 300 nm. The films before annealing in O₂ atmosphere had low T_c of ~50 K because of the stress effect [Ref. 57]. After annealing in O₂, the c -axis length decreased and cracks were formed in parallel along the (001) planes as shown in a field emission-scanning electron microscope (FE-SEM) picture (Fig. 3.14). The T_c was raised up to 85 K which was,

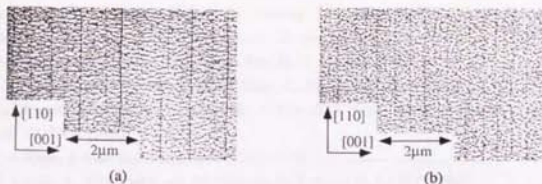


Fig. 3.14 FE-SEM pictures of YBCO/PBCO bilayers deposited on SrTiO₃(100) substrate. (a) YBCO/PBCO = 300 nm/100 nm, (b) YBCO/PBCO = 100 nm/50 nm.

however, lower than the maximum T_c of this system, 90 K suggesting the possibility of the presence of residual stress.

The as-grown films were subject to the STM/STS measurements without surface preparation. Details about these films are described in [Refs. 58-60].

References

- [1] G. Binnig, and H. Rohrer, *Helv. Phys. Acta* 55, 726 (1982).
- [2] G. Binnig, and H. Rohrer, *IBM J. Res. Develop.* 30, 355 (1986).
- [3] C. A. Lang, M. M. Dovek, and C. F. Quate, *Rev. Sci. Instrum.* 60, 3109 (1989).
- [4] D. M. Eigler, and E. K. Schweizer, *Nature* 344, 524 (1990).
- [5] R. Gaisch, J. K. Gimzewski, B. Reihl, R. R. Schlittler, M. Tschudy, W. D. Schneider, *Ultramicroscopy* 42-44, 1621 (1992).
- [6] R. R. Schulz, and C. Rossel, submitted to *Rev. Sci. Instrum.*
- [7] D. P. E. Smith, and G. Binnig, *Rev. Sci. Instrum.* 57, 2630 (1986).
- [8] A. P. Fein, J. R. Kirtley, and R. M. Feenstra, *Rev. Sci. Instrum.* 58, 1806 (1987).
- [9] J. W. Lyding, S. Skala, J. S. Hubacek, R. Brockenbrough, and G. Gammie, *Rev. Sci. Instrum.* 59, 1897 (1988).
- [10] C. Renner, P. Niedermann, A. D. Kent, and Ø. Fischer, *J. Vac. Sci. Technol. A* 8, 330 (1990).
- [11] B. L. Blackford, M. H. Jericho, and M. G. Boudreau, *Rev. Sci. Instrum.* 63, 2206 (1992).
- [12] P. Davidsson, H. Olin, M. Persson, and S. Pehrson, *Ultramicroscopy* 42-44, 1470 (1992).
- [13] H. Bando, H. Tokumoto, A. Zettl, and K. Kajimura, *Ultramicroscopy* 42-44, 1627 (1992).
- [14] T. Hasegawa, H. Suzuki, S. Yaegashi, H. Takagi, K. Kishio, S. Uchida, K. Kitazawa, and K. Fueki, *Jpn. J. Appl. Phys.* 28, L179 (1989).
- [15] G. Binnig, and D. P. E. Smith, *Rev. Sci. Instrum.* 57, 1688 (1986).

- [16] H. L. Edwards, J. T. Markert, and A. L. de Lozanne, *Phys. Rev. Lett.* 69, 2967 (1992).
- [17] R. S. List, A. J. Arko, Z. Fink, S.-W. Cheong, S. D. Conradson, J. D. Thompson, C. B. Pierce, D. E. Peterson, R. J. Bartlett, N. D. Shinn, J. E. Schirber, B. W. Veal, A. P. Paulikas, and J. C. Campuzano, *Phys. Rev. B* 38, 11966 (1988).
- [18] J. C. Campuzano, G. Jennings, M. Faiz, L. Beaulaigue, B.W. Veal, J. Z. Liu, A. P. Paulikas, K. Vandervoort, H. Claus, R. S. List, A. J. Arko, and R. J. Bartlett, *Phys. Rev. Lett.* 64, 2308 (1990).
- [19] C. J. Chen, *J. Vac. Sci. Technol. A* 6, 319 (1988).
- [20] N. Isshiki, K. Kobayashi, and M. Tsukada, *Surf. Sci.* 238, L439 (1990).
- [21] K. Kobayashi, M. Tsukada, and N. Isshiki, *Solid State Commun.* 74, 1187 (1990).
- [22] K. Kobayashi, and M. Tsukada, *J. Vac. Sci. Technol. A* 8, 170 (1990).
- [23] S. Ohnishi, and M. Tsukada, *J. Vac. Sci. Technol. A* 8, 174 (1990).
- [24] N. Isshiki, K. Kobayashi, and M. Tsukada, *J. Vac. Sci. Technol. B* 9, 475 (1991).
- [25] M. Tsukada, K. Kobayashi, N. Shima, and N. Isshiki, *J. Vac. Sci. Technol. B* 9, 492 (1991).
- [26] H. W. Fink, *IBM J. Res. Develop.* 30, 460 (1986).
- [27] T. Sakurai, A. Sakai, and H. W. Pickering, *Advances in Electronics and Electron Physics*, Academic Press, Boston, 1 (1989).
- [28] T. Sakurai, T. Hashizume, I. Kamiya, Y. Hasegawa, N. Sano, H. W. Pickering, and A. Sakai, *Prog. Surf. Sci.* 33, 3 (1990).
- [29] T. Sakurai, T. Hashizume, I. Kamiya, Y. Hasegawa, T. Ide, M. Miyao, I. Sumita, A. Sakai, and S. Hyodo, *J. Vac. Sci. Technol. A* 7, 1684 (1986).
- [30] T. Sakurai, T. Hashizume, Y. Hasegawa, I. Kamiya, N. Sano, K. Yokoyama, H. Tanaka, I. Sumita, and S. Hyodo, *J. Vac. Sci. Technol. A* 8, 324 (1990).
- [31] J. Halbritter, *Surf. Sci.* 122, 80 (1982).
- [32] R. Berthe, and J. Halbritter, *Phys. Rev. B* 43, 6880 (1991).
- [33] J. Halbritter, *Phys. Rev. B* 46, 14861 (1992).
- [34] Sang-il Park, Ph. D. Thesis, Stanford University, 46 (1986).
- [35] Sang-il Park, and C. F. Quate, *Rev. Sci. Instrum.* 58, 2004 (1987).
- [36] Y. Matsui, H. Maeda, Y. Tanaka, and S. Horiuchi, *Jpn. J. Appl. Phys.* 27, L372 (1988).
- [37] Y. Matsui, H. Maeda, Y. Tanaka, E. Takayama-Muromachi, S. Takekawa, and S. Horiuchi, *Jpn. J. Appl. Phys.* 27, L827 (1988).
- [38] S. Horiuchi, H. Maeda, Y. Tanaka, and Y. Matsui, *Jpn. J. Appl. Phys.* 27, L1172 (1988).
- [39] J. D. Jorgensen, B.W. Veal, W. K. Kwok, G. W. Crabtree, A. Umezawa, L. J. Nowicki, and A. P. Paulikas, *Phys. Rev. B* 36, 5731 (1987).
- [40] A. Renault, J. K. Burdett, and J. P. Pouget, *J. Solid State Chemistry* 71, 587 (1987).
- [41] R. Beyers, B. T. Ahn, G. Groman, V. Y. Lee, S. S. P. Parkin, M. L. Ramirez, K. P. Roche, J. E. Vazquez, T. M. Gür, and R. A. Huggins, *Nature* 340, 619 (1989).
- [42] R. J. Cava, A. W. Hewat, E. A. Hewat, B. Batlogg, M. Marezio, K. M. Rabe, J. J.

- Krajewski, W. F. Peck Jr., and L. W. Rupp Jr., *Physica C* 165 419 (1990).
- [43] G. A. Sawatzky, and J. W. Allen, *Phys. Rev. Lett.* 53, 2339 (1984).
- [44] J. W. Zaanen, and G. A. Sawatzky, *Can. J. Phys.* 65, 1262 (1987).
- [45] R. J. Birgeneau, and G. Shirane, *Physical Properties of High Temperature Superconductors I*, edited by D. M. Ginsberg, World Scientific Publishing, 152 (1989).
- [46] S. Uchida, T. Ido, H. Takagi, T. Arima, Y. Tokura, and S. Tajima, *Phys. Rev.* B43, 7942 (1991).
- [47] S. Uchida, *Physica C* 185-189, 28 (1991).
- [48] J. W. Allen, C. G. Olson, M. B. Maple, J.-S. Kang, L. Z. Liu, J.-H. Park, R. O. Anderson, W. P. Ellis, J. T. Markert, Y. Dalichaouch, and R. Liu, *Phys. Rev. Lett.* 64, 595 (1990).
- [49] H. Namatame, A. Fujimori, Y. Tokura, M. Nakamura, K. Yamaguchi, A. Misu, H. Matsubara, S. Suga, H. Eisaki, T. Ito, H. Takagi, and S. Uchida, *Phys. Rev. B* 31, 7205 (1990).
- [50] H. Romberg, M. Alexander, N. Nücker, P. Adelman, and J. Fink, *Phys. Rev. B* 32, 8868 (1990).
- [51] J. Fink, N. Nücker, M. Alexander, H. Romberg, M. Knupfer, M. Merkel, P. Adelmann, R. Claessen, G. Mante, T. Buslaps, S. Harn, R. Manzke, and M. Skibowski, *Physica C* 185-189, 45 (1991).
- [52] C. T. Chen, F. Sette, Y. Ma, M. S. Hybertsen, E. B. Stechel, W. M. C. Foulkes, M. Schluter, S.-W. Cheong, A. S. Cooper, L. W. Rupp, Jr., B. Batlogg, Y. L. Soo, Z. H. Ming, A. Krol, and Y. H. Kao, *Phys. Rev. Lett.* 66, 104 (1991).
- [53] R. Sieburger, P. Müller, and J. S. Schilling, *Physica C* 181, 335 (1991).
- [54] H. F. Poulsen, N. H. Andersen, J. V. Andersen, H. Bohr, and O. G. Mouritsen, *Nature* 349, 594 (1991).
- [55] M. R. Presland, J. L. Tallon, R. G. Buckley, R. S. Liu, and N. E. Flower, *Physica C* 176, 95 (1991).
- [56] N. Motohira, K. Kuwahara, T. Hasegawa, K. Kishio, and K. Kitazawa, *J. Ceram. Soc. Jpn. Int. Ed.* 97, 994 (1989).
- [57] E. Olsson, A. Gupta, M. D. Thouless, A. Segmuller, and D. R. Clarke, *Appl. Phys. Lett.* 58, 1682 (1991).
- [58] M. Kawasaki, J. P. Gong, M. Nantoh, T. Hasegawa, K. Kitazawa, M. Kumagai, K. Hirai, K. Horiguchi, M. Yoshimoto, and H. Koinuma, *Jpn. J. Appl. Phys.* 32, 1612 (1993).
- [59] J. P. Gong, M. Kawasaki, K. Fujito, R. Tsuchiya, M. Yoshimoto, and H. Koinuma, *Phys. Rev. B* 50, 3280 (1994).
- [60] K. Fujito, M. Kawasaki, J. P. Gong, R. Tsuchiya, M. Yoshimoto, and H. Koinuma, *Proceedings of IU-MRS-ICAM-93*, Tokyo, Japan, September 1992.

Chapter 4

Observations on BSCCO Single Crystals

4.1 Introduction

BSCCO is the most intensively studied HTSC material by STM. A BSCCO single crystal is cleavable so that an atomically flat clean surface which is suitable for an STM observation can be easily obtained by cleaving it. Actually, very clear atomic resolution STM images with the modulation structure along the b -axis were obtained on the cleaved surfaces of BSCCO single crystals in UHV at room temperature [Refs. 1-4]. The topographical features observed in these works are qualitatively consistent. A detailed analysis [Ref. 2] revealed that the corrugations observed in these images agree very well to the lattice structure of the BiO plane in the bulk derived from XRD [Ref. 5]. This confirms that the cleavage plane of the BSCCO single crystal is the BiO plane.

STS studies on the cleaved surface of BSCCO have shown that the surface BiO layer is nonmetallic [Refs. 2, 4, 6]. Hasegawa *et al.* have achieved an atomic resolution STM/STS observation on the cross-sectional surface (b - c plane) of a BSCCO single crystal at room temperature in dry N_2 atmosphere [Ref. 7]. The STM images show higher and lower layers which have been assigned to be $(CuO_2)_2$ and $(BiO)_2$ layers, respectively [Figs. 4.1(a), 4.1(b)]. As the bias voltage is decreased, the $(CuO_2)_2$ layer is enhanced relatively to the $(BiO)_2$ layer, implying that the density of states near the Fermi level (E_F) in the CuO_2 layer is substantially higher than that in the BiO layer. The STS result indicated that the BiO layer in the bulk is semiconducting with a band gap energy of 0.1 eV while the CuO_2 layer is essentially metallic [Fig. 4.1(c)].

On the other hand, the local-density-approximation (LDA) band-structure calculations predicted the contribution to the density of states at the Fermi level [$N(E_F)$] from both the CuO_2 plane and the BiO plane [Refs. 8-10]. There are two distinct types of bands which intersect E_F [Fig. 4.2(a)].

The first corresponds to a nearly degenerate pair of antibonding $Cu3d_{x^2-y^2}-O2p_{xy}$ states which disperse above E_F toward the X point in the Brillouin zone, leaving them less than half filled. The second represents the lowest band from the $Bi6p_{xy}-O2p_{xy}$ manifold which intersects E_F and form the electron pockets near the \bar{M} and L points. The calculated Fermi surface in an extended zone scheme shows the two nearly degenerate hole surfaces expected for the Cu-O bands centered at the X point and the Y point indicating nesting feature, and a small rounded square electron surface formed by the Bi-O band centered at the \bar{M} and L points [Fig. 4.2(b)]. Massidda *et al.* [Ref. 8] found that in the absence of interactions between the Cu-O band and the Bi-O band, there are two Bi-O bands crossing three Cu-O bands below E_F in the region near \bar{M} and L [Fig. 4.2(c)], and the

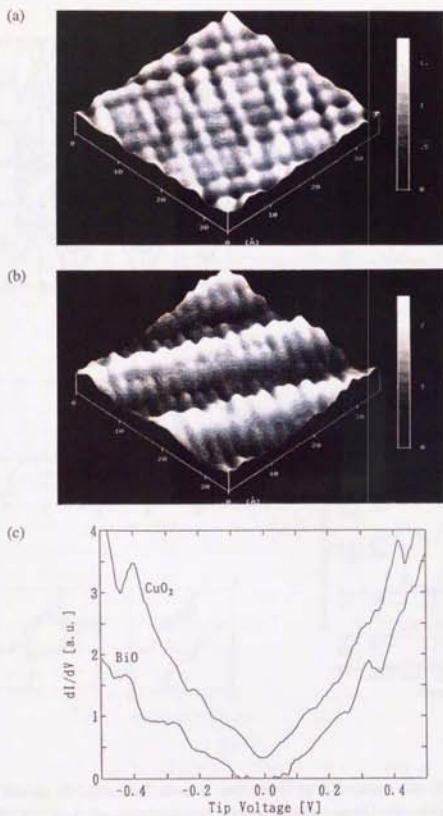


Fig. 4.1 STS observation on the b - c plane of a BSCCO single crystal measured at room temperature [Ref. 7]. (a), (b) Bias voltage dependence of STM images. Tip bias voltages were (a) -1.5 V, and (b) $+0.1$ V, respectively. (c) Tunneling spectra observed on BiO and CuO₂ layers.

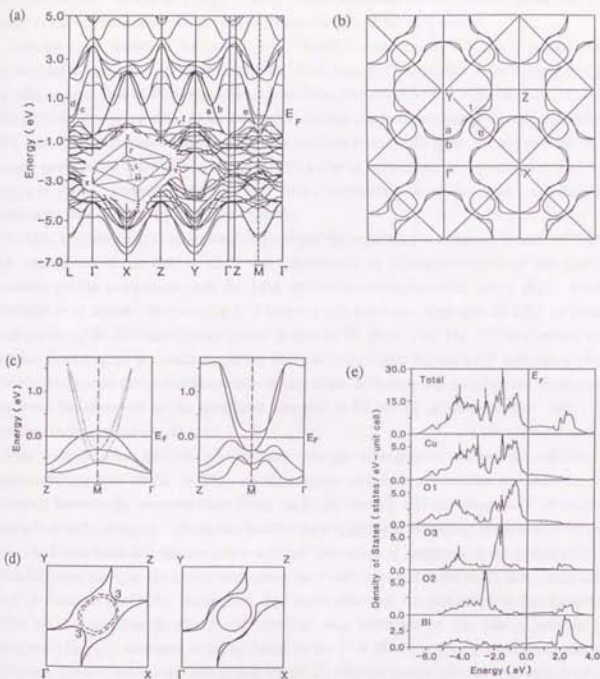


Fig. 4.2 Results of LDA band structure calculation by Massidda *et al.* [Ref. 8]. (a) Energy bands of BSCCO along the main symmetry lines of the face-centered orthorhombic Brillouin zone shown as an inset. (b) Fermi surfaces of BSCCO in an extended zone scheme. (c) Schematic drawing of the band structure near \bar{M} and near the Fermi level for "non-interacting" bands, and "interacting" bands. (d) Schematic of the Fermi surfaces corresponding to "non-interacting" bands, and "interacting" bands. (e) Total and projected DOS for valence bands.

Fermi surface consists of two distinct Cu-O surfaces and two distinct Bi-O surfaces which touch each other in the Γ -Z direction [Fig. 4.2(d)]. These calculation results indicate that the BiO layer works as a conducting reservoir of carriers, which disagree to the STS results.

From the same reason as the case of the STM/STS measurement, BSCCO is suitable for a photoemission spectroscopy (PES) experiment which demands smoothness of the sample surface. Actually, a great deal of PES experiments have been performed on this material [Refs. 11-27]. PES gives the density of states of the material so that the obtained data can be directly compared to STS data. The difference between these two methods is that PES gives the information in the k -space as described below, on the contrary, STS gives the information in the real space, *i.e.*, local density of states. Therefore, PES and STS have a compensational relation, and it is valuable to compare the data obtained by these two methods.

PES has a capability to examine band dispersion if the angle resolve technique is used (ARPES). The first interest of this field of study was concentrated on the band structure of this material, especially on the comparison with the LDA calculation result described above [Refs. 8-10]. Takahashi *et al.* insisted the insulating BiO feature which is not consistent with the LDA calculation result predicting the BiO-like electron pocket around the \bar{M} point [Ref. 11]. On the contrary, most of other results agree to metallicity of the BiO plane concluded by the LDA calculation [Refs. 12-15]. Wells *et al.* found that the metallic feature of the BiO plane was not observed on as-grown specimens but observed on the specimens annealed in 12 atm O_2 atmosphere [Ref. 18]. This explained both previous results.

Next interest was focused on the low energy quasiparticle excitations reflecting a superconducting state [Refs. 12-17]. As high angular and energy resolution was achieved, the difference between the spectrum taken along the Γ - \bar{M} direction and that along the Γ -X direction received scientific attention. The diplike feature which appears at the region centered at 75-90 meV below the Fermi level (E_F) became also a problem. Dessau *et al.* reported that the diplike structure appeared below the T_c in the spectra taken along the Γ - \bar{M} direction but did not in those taken along the Γ -X direction [Ref. 19]. In addition, they found that some spectral weight in the dip formed region of the spectrum in the Γ - \bar{M} direction was transferred to the pileup peak of the superconducting gap structure of the spectrum in the Γ -X direction during the superconducting transition. These features were remarkable for the H_2 -reduced sample but less pronounced for the O_2 -annealed sample. On the other hand, Hwu *et al.* reported the diplike structure at the energy corresponding to 3Δ (2Δ : superconducting gap energy) in the spectra taken both along the Γ - \bar{M} direction and along the Γ -X direction, and the spectral weight was conserved in any directions [Ref. 20]. Although these two results contradict to each other, it seems to be true that this diplike structure is an intrinsic feature for high temperature superconductivity of the BSCCO system. This diplike feature has been explained by existence of two bands in close proximity to each other, strong electron-phonon coupling [Refs. 28, 29], the resonating valence state [Refs. 30, 31], and the marginal Fermi liquid phenomenology [Ref. 32, 33].

All the ARPES studies showed gap anisotropy in the a - b plane, *i.e.*, the larger superconducting

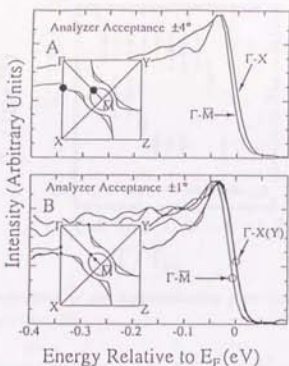


Fig. 4.3 High resolution ARPES data at k locations along the Brillouin zone edge and the zone diagonal by Wells *et al.* [Ref. 23].

gap in the Γ - \bar{M} direction than in the Γ - X direction [Refs. 19, 21-24, 26], except one early study observing an isotropic gap [Ref. 13]. These results ruled out an isotropic s -wave symmetry of the superconducting order parameter of the BSCCO system. Wells *et al.* [Ref. 23] concluded a d -wave symmetry [$\Delta(k) \sim \cos k_x a - \cos k_y a$] or a mixed symmetry with a strong d -wave component [Refs. 34-44] from their result showing an anisotropic gap (Fig. 4.3). However, they could not exclude the possibility of a $s+id$ mixed order parameter [Ref. 45] because the observed gap in the Γ - \bar{M} direction was larger than expected if a node exists in the gap symmetry. They attributed this ambiguity to the finite observing range of k space in the ARPES measurement which makes it impossible to establish whether a node exists or not. In the following work by Shen *et al.*, they observed a very small or null gap in the Γ - Y direction which strongly suggests the existence of the node and claimed that the d -wave symmetry was suitable for their result [Ref. 24]. Recent study by J. Ma *et al.* reported that the size of the gap in the Γ - X direction varied with oxygen concentration, ranging from 0.2 meV for underdoped or optimally doped samples to 8-12 meV for overdoped samples [Ref. 26]. They also measured the temperature dependence of the spectra taken along the Γ - \bar{M} and Γ - X directions and compared them (Fig. 4.4). They found that the gap opens quite rapidly below T_c in the Γ - \bar{M} direction, and, on the contrary, the gap begins to open slowly well below T_c in the Γ - X direction, which means the gap anisotropy has temperature dependence in this material. Based on these observations, they concluded that the simple type of d -wave symmetry order parameter should be ruled out, and the $s+id$ symmetry is favorable. Furthermore, most recent work by Ding *et al.* with much higher angular and energy resolution derived the

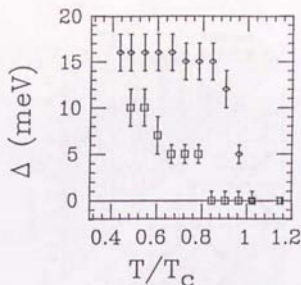


Fig. 4.4 Temperature dependence of the superconducting gaps measured along the Γ - X and Γ - \bar{M} directions by Ma *et al.* [Ref. 26].

conclusion that the gap minimum direction deviates from the Γ - \bar{M} direction which suggests an extended s -wave symmetry [$\Delta(k) \sim \cos k_x a + \cos k_y a$] of the order parameter [Ref. 27].

Moreover, a recent ARPES study by Dessau *et al.* made it clear that the Fermi surface determined by the LDA calculation indicating metallic nature of the BiO plane [Refs. 8-10], which was once established [Refs. 12-15, 18], is not true [Ref. 25]. Their recent result did not show the small piece of Fermi surface with strong BiO character centered around the \bar{M} point, and partially agree to the Fermi surface composed of two strongly nested pieces of the CuO_2 Fermi surface centered around the X (Y) point and the Γ (Z) point (Fig. 4.5) calculated by artificially ignoring the interaction between the BiO states and the CuO_2 states [Ref. 8]. This implies that the electronic states near E_F are mainly CuO_2 derived and the BiO bands remain above E_F for all k , which is consistent with the result from the STS experiments [Refs. 2, 4, 6, 7] measured at room temperature. They also found the presence of two flat bands within 30-50 meV of E_F around the \bar{M} point, and speculated that this flat bands at E_F may play a significant role for the high temperature superconductivity of this system.

As discussed above, the field of PES study on BSCCO is currently driven into a state of chaos. The keys to get out of this state are probably the angular and energy resolution of the apparatus which still seems not to be enough, the technique to keep a clean sample surface during the measurement, the quality of the specimen especially concerning twins, and the oxygen content of the crystal which should be the same about the data compared. This seems to give instructions for tunneling measurements.

Now, our interest is how the electronic structure of BSCCO is observed at cryogenic temperature below the T_c with the STS technique. Our experiments on the BSCCO single crystals presented below were done during the period from 1990 to 1991. When we started, no other groups succeeded in obtaining atomic resolution on BSCCO at cryogenic temperature. After we succeeded

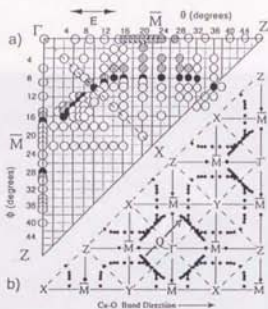


Fig. 4.5 The Fermi surface of BSCCO experimentally determined with ARPES by Dessau *et al.* [Ref. 25].

in the cryogenic observation with atomic resolution for the first time [Ref. 46], a number of groups also succeeded [Refs. 47-52]. Most of their data can be categorized in some cases of our results although the conclusions of some groups are different from ours, which will be discussed in Chapter 7.

4.2 STM Observations on Cleaved Surfaces of BSCCO Single Crystals

As described in section 3.2.2, we prepared BSCCO single crystals annealed in various atmospheres. We observed cleaved surfaces of these specimens, and whether atomic resolution could be achieved or not strongly depended on the annealing processes of the specimens. We often obtained atomic resolution images on the Air- or O₂-annealed crystals, but nothing on the as-grown crystals or the specimens annealed in N₂ or Ar atmosphere.

It is clear that annealing treatment changed some properties of the BSCCO single crystals, which determined whether atomic resolution STM observations were allowed or not. Annealing treatment seems to have two kinds of effects on the crystals. For one thing, annealing treatment is thought to improve the homogeneity of the crystals. The crystals must contain a great deal of microscopic defects. And, if we cleave the crystal, the cleaved place must correspond to defective place in the crystal. Therefore, the surface BiO plane cannot be complete, but has defects, steps and regions where another planes beneath it appear. It is natural to think that the possibility of getting atomic resolution by STM increases if the homogeneity of the crystal is improved by annealing with the

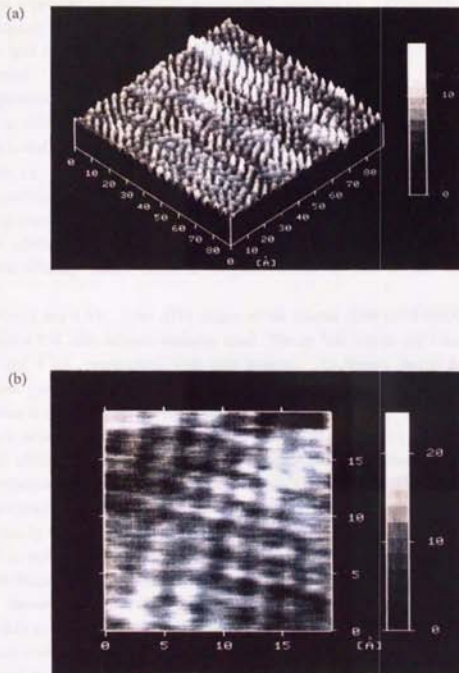


Fig. 4.6 STM images on the cleaved surfaces of BSCCO single crystals at 4.2 K. (a) Wide scan image measured with $V_b = -0.75$ V and $I_t = 5$ nA. (b) Narrow-scan image measured with $V_b = -0.75$ V and $I_t = 5$ nA.

result that the completeness of the surface layer is made better. Another possible effect by annealing process is changing oxygen contents of the crystals. BSCCO has nonstoichiometry of oxygen mainly on the BiO planes, which is varied by annealing depending on the annealing conditions, especially the atmosphere, and electronic nature of the BiO planes is determined by the oxygen content. As described below in section 4.3.4, the surface BiO layer became more metallic as the oxygen content increased, which is consistent with the change of electronic nature of the whole crystal.

The specimen dependence of getting atomic resolution can be explained as follows. Atomic imaging is allowed only on enough homogeneous crystals which are obtained by annealing treatment so that atomic images could not be obtained on the as-grown crystals. And the annealing conditions, *i.e.*, temperature and O₂ pressure, in Ar or N₂ atmosphere were not suitable ones. Another possibility is that the specimens whose surface BiO plane's electronic nature is comparably metallic are suitable for STM observations, although the reason is not clear at the present moment. However, whether atomic resolution can be achieved or not depends not only on the specimen but also on the STM tip. Hence further investigations should be done in order to make this subject clear.

Figs. 4.6(a) and 4.6(b) show STM images of the cleaved surfaces of BSCCO single crystals measured at 4.2 K with different scanning areas. The tip bias voltage and tunneling current were 0.75 V and 5 nA, respectively, with both images. The figures clearly demonstrate atomic corrugations corresponding to Bi atoms with an average interval of 0.35 nm, similar to the observations at room temperature under ultrahigh vacuum [Refs. 1-4]. Fig. 4.6 also indicates the modulation structure along the *b*-axis, which is seen as the waving of background with the periodicity of about 2.7 nm. In the bright regions of the images, Bi atoms concentrate. According to the refinement of the crystal structure of BSCCO by a Rietveld method [Ref. 53], this modulation structure is not real waving of the Bi atoms, but reflects the variation of local density of states caused by the concentration of the Bi atoms.

Kirk *et al.* reported that a missing row of Bi atoms occurs either every nine or ten atomic sites in both (110) directions, and accounted for the incommensurate periodicity of the modulation structure [Ref. 1]. However, we have never observed such missing rows in the images of the cleaved BiO planes. Shih *et al.* reported that they observed atomic rows depressed downward only when the bias voltage was higher than 1 V, which seems to be consistent with both of the results [Ref. 54].

The fact that atomic images were taken seems to guarantee the achievement of the condition of complete vacuum tunneling. Tunneling measurements on the HTSC's using cryogenic STM had already been reported [Refs. 55-61]. However, the condition of vacuum tunneling had not been secured in these experiments resulting in a lack of atomic resolution. Actually, in these works, the tunneling tip had been in contact with the sample surface, *i.e.*, the STM tip had been used in the mode of the point contact. We can claim that the present observations were done under the secured condition of vacuum tunneling, therefore the spectroscopic data obtained are reliable if compared to the former reported results.

4.3 STS Measurements on Cleaved Surfaces of BSCCO Single Crystals

4.3.1 Atomic Site Tunneling-Spectroscopy (AST) Measurements on Surface BiO Layers

Fig. 4.7 shows a result of an AST measurement at 4.2 K performed on the cleaved surface of a BSCCO single crystal annealed in Air. Fig. 4.7(a) shows the 64 spots where the tunneling spectra were taken during the imaging. In the image, the arrangement of Bi atoms can be observed, although it is distorted. In the AST measurement, the feedback is turned off during the measurements of tunneling spectra, therefore this measurement is very sensitive to mechanical noises. This technical problem is thought to cause the observed distortion of the image. Fig. 4.7(b) superimposes the 16 tunneling spectra chosen among the 64 spectra at random. Tunneling spectra obtained at the locations marked in the figure do not show difference but demonstrate basically the same feature with a band gap of about 0.1 eV independent of the measuring locations, indicating that the surface BiO layer was uniformly semiconductive even below T_c . The same result was observed on an O₂-annealed specimen (Fig. 4.8). Fig. 4.9 indicates the tunneling spectra with higher energy resolutions measured on the Air-annealed specimen [Fig. 4.9(a)] and the O₂-annealed one [Fig. 4.9(b)]. These spectra clearly indicate semiconducting features with band gap structures. We concluded that the surface BiO layer has semiconductive electronic structure even in the superconducting state.

This conclusion is consistent with the tunneling results, which were measured by STM at room temperature, reported so far [Refs. 2, 4, 6, 7], but disagree to LDA band-structure calculations [Refs. 8-10] which predicted existence of the electron pocket, *i.e.*, metallic BiO bands. On the other hand, from ARPES studies, Takahashi *et al.* reported a semiconducting nature of the BiO plane [Ref. 11], but Olson *et al.* [Refs. 12-14] and Dessau *et al.* [Refs. 19, 21] insisted that the E vs. k dispersion relationship of the BiO band intersects the Fermi level at the same k position as the band calculation predicted. Wells *et al.* [Ref. 18] found that the surface BiO band can be either metallic or nonmetallic depending on the oxygen-annealing process. However, we measured the specimens treated with different annealing processes and observed basically same semiconducting behavior, although the band gap energy was changed depending on the oxygen content as will be described in section 4.3.4. It should be noted that the most recent ARPES results with high angular and energy resolution [Refs. 24, 25] did not observe the electron pocket and reported the Fermi surface which corresponds to the result calculated ignoring the interaction between the Cu-O band and the Bi-O band [Ref. 8]. Considering the STS results and the recent ARPES results, the semiconducting nature of the BiO layer seems to be true. The fact that the LDA calculation result does not reflect the real BiO nature is possibly attributed to nonstoichiometry of oxygen, Sr substitution on the Bi site, and the incommensurate superstructure along the b -axis, which were not taken into account.

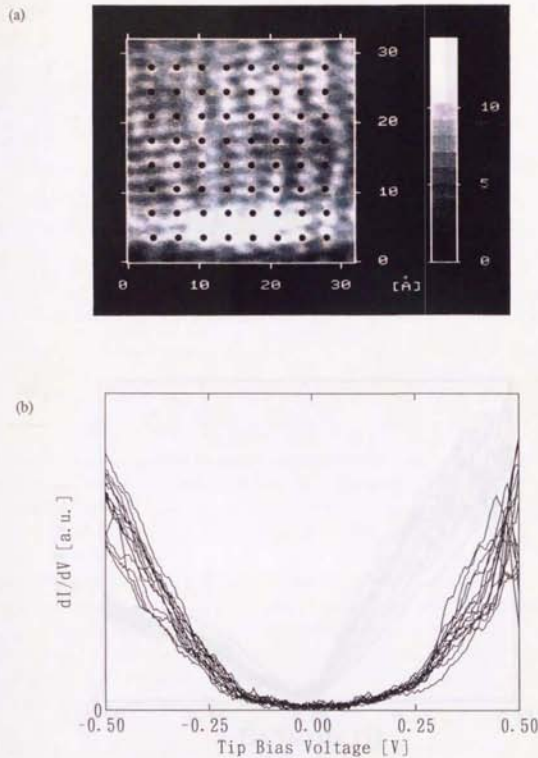


Fig. 4.7 AST measurement on the cleaved surface of an air-annealed BSCCO single crystal at 4.2 K. (a) STM image taken with $V_b = -0.75$ V and $I_p = 1$ nA. Black dots in the figure represent the spectroscopic measurement locations. (b) Tunneling spectra measured at the locations marked in the image with $V_b = -0.75$ V and $I_p = 1$ nA.

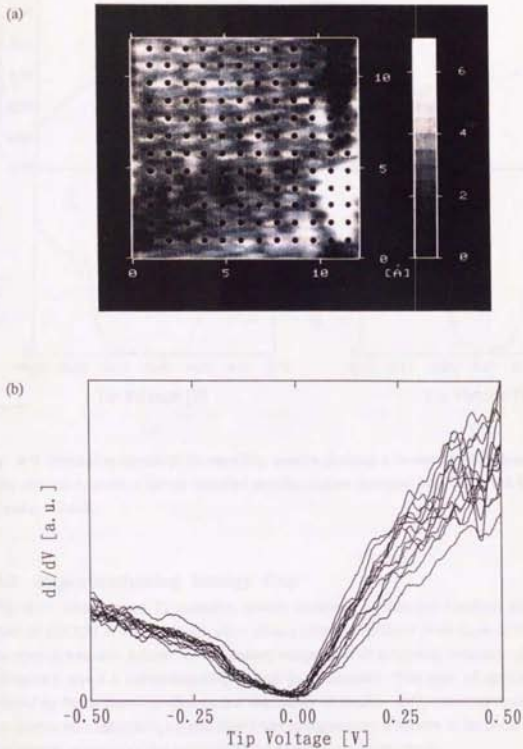


Fig. 4.8 AST measurement on the cleaved surface of an oxygen-annealed BSCCO single crystal at 4.2 K. (a) STM image taken with $V_s = -0.75$ V and $I_t = 1$ nA. Black dots in the figure represent the spectroscopic measurement locations. (b) Tunneling spectra measured at the locations marked in the image with $V_s = -0.75$ V and $I_t = 1$ nA.

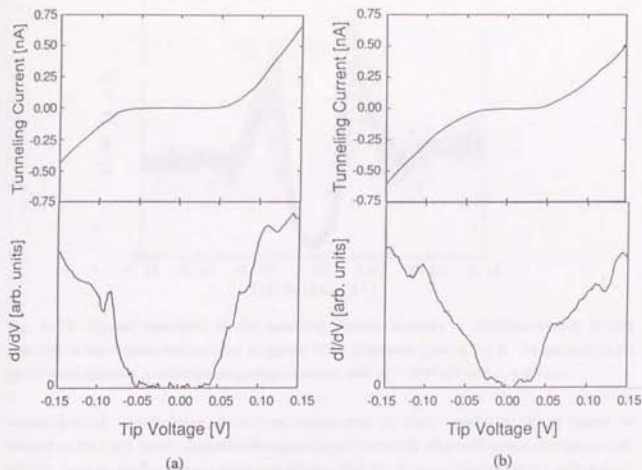


Fig. 4.9 Typical examples of the tunneling spectra showing a semiconducting feature measured on the cleaved surfaces of (a) air-annealed and (b) oxygen-annealed BSCCO at 4.2 K. $V_b = -300$ mV and $I_p = 2$ nA.

4.3.2 Superconducting Energy Gap

Fig. 4.10 demonstrates 12 tunneling spectra measured at different locations on the cleaved surface of BSCCO at 4.2 K, which show clearly different behavior from those in Figs 4.7-4.9. These spectra basically indicate a same feature independent of measuring locations. It is clear that these spectra reveal a superconducting energy gap structure. This type of spectra were often measured on the as-grown specimens, but very rarely on the Air- or O_2 -annealed ones. And, when these spectra were measured, a signal which was strong enough relatively to the noise level was not recorded with scanning so that a clear STM image could not be obtained.

Considering these matters, it is clear that when the superconducting spectra were observed, the surface condition was different from that under which the spectra showed the semiconducting behavior. Another clear point is that, in this case, the density of states near the E_F was metallic and superconducting, and there was no contribution from semiconductive bands around the E_F . One possible assumption is that the surface layer was not the BiO layer but the CuO_2 layer. However, it is questionable that the CuO_2 layer which is not covered with the hole donor layers becomes

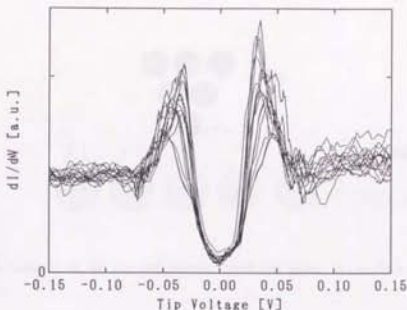


Fig. 4.10 Typical examples of the tunneling spectra showing a superconducting feature measured on the cleaved surface of an as-grown BSCCO single crystal at 4.2 K. 12 superimposed spectra were obtained at different measuring locations with $V_b = -200$ mV and $I_p = 20$ nA.

superconducting. Furthermore, there is no reason why an atomic resolution image cannot be obtained on the CuO_2 layer. Actually, Hasegawa *et al.* previously observed atomic corrugations of the CuO_2 layer on the b - c plane at room temperature [Ref. 7]. It is most likely that the surface layer which covered the superconducting CuO_2 layer had an insulating nature, and the edge energy of the band gap was higher than the operating tip bias voltage, so that there was no contribution from this top layer to the observed energy region near the E_F . There are two possible cases. The first case is that the specimen contained lots of defects and the cleaved top layer of the observed area was not the BiO layer but the SrO layer beneath it. The LDA calculation predicted that the Sr is ionic and has an insulating nature. If the SrO layer originally has an insulating nature, or if it became insulating because of oxygen depletion, the tunneling spectra reflected the superconducting electronic structure of the underlying CuO_2 layer as shown in Fig. 4.10. The second one is that the crystal had variation of the oxygen content and the cleaved place corresponded to the oxygen poor region in the crystal. In this case, the surface BiO layer had a small oxygen content resulting in the insulating nature with a wider band gap compared to the specimens on which the semiconducting spectra were observed as shown in Figs. 4.7-4.9.

The fact that a clear STM picture could not be obtained can be explained as follows. For one thing, the STM tip could not perceive the surface insulating layer and was very close to or elastically touched it, which did not allow the tip to trace the contour of the electronic density originating from the underlying CuO_2 layer because of the interaction between the tip and the surface layer (see Fig. 4.11). Another effect which should be taken into account is that the surface insulating layer might make the tunneling barrier between the CuO_2 layer and the STM tip lower than the vacuum barrier. The band gap energy, which determine the barrier height in the region of

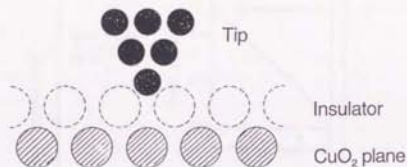


Fig. 4.11 Schematic of the tip and sample condition when the surface is covered with an insulating layer.

the surface layer, is thought to be lower than the vacuum work function of a metal which is typically 4-5 eV. Therefore, the average barrier height between the CuO_2 layer and the STM tip becomes lower in the case that the CuO_2 layer is covered with the surface insulating layer (Fig. 4.12). This is a very similar case to the metal surface covered with an oxide layer. In such a case, the tunneling current does not show the exponential decay as a function of the tip-sample separation which is expected on a non-degraded metal surface, and significant tunneling currents still remain after withdrawing the tip far from the sample surface. This makes the sensitivity of the tunneling current to the tip-sample separation worse, *i.e.*, the resolution in the z -direction becomes lower, so that it becomes very difficult to trace atomic corrugations. Fig. 4.13 demonstrates the comparison between the plot of the tunneling current as a function of the tip-sample separation measured on an as-grown YBCO thin film and that measured on a degraded film after exposure to air [Ref. 62].

Moreover, as the result of these two effects, the position of the STM tip is kept further from the CuO_2 plane than that when the CuO_2 plane appears on the surface even with the same bias voltage

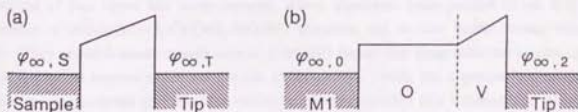


Fig. 4.12 Idealized tunneling barriers (a) between two metals with different work functions. (b) Composite barrier with oxide layer, O, and vacuum gap V. From [Ref. 25].

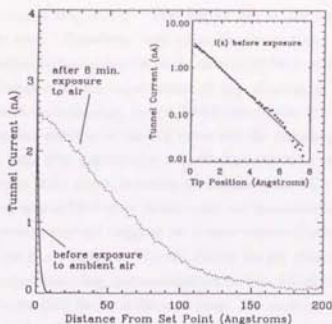


Fig. 4.13 Plots of the tunneling current from a Pt-Ir tip into a pulsed-laser-deposited YBCO film as a function of the tip-sample separation measured after mounting a sample onto the STM in an inert-atmosphere glove box (solid curve), and after an 8-min exposure to ambient air (dotted curve). From [Ref. 62].

and the same tunneling current. As discussed in section 2.2.2, the resolution of STM can be expressed by

$$L \cong 2\sqrt{2} \sqrt{\ln \eta} \sqrt{\frac{(s+R)}{\kappa}} \quad (2.40)$$

This equation indicates that the larger the tip-sample distance (s in the equation) is, the lower the resolution is, which is consistent with the observed tendency about atomic resolution.

Murakami *et al.* recently reported their STM/STS observations on cleaved surfaces of BSCCO single crystals with a cryogenic STM in an UHV system [Ref. 52]. They found a step structure composed of two upper and lower terraces, whose separation corresponded to the BiO-BiO separation of BiO-SrO-CuO₂-Ca-CuO₂-SrO-BiO sequence, and another middle terrace between them. They obtained atomic images indicating the BiO feature and semiconductive spectra on the upper and lower terraces which are thought to be the BiO layers, and superconducting spectra without an atomic image on the middle terrace which corresponded to a different kind of layer. Their result directly confirmed legitimacy of our first assumption. On the other hand, we performed STS measurements on cleaved surfaces of the BSCCO single crystals which had been stored in the vacuum chamber for 12 hours in order to deplete oxygen of the surface BiO layer. As will be discussed below in section 4.3.5, the spectrum is composed of the separated BiO (or SrO) bands and residual density of states with a superconducting gap structure originating from the CuO₂

band in the band gap region (Fig. 4.23). This proved the second case of our assumptions described above to be true. Therefore, both cases discussed above are realized in actual experiments obtaining superconducting spectra on the cleaved surfaces of BSCCO single crystals. We will discuss the sharpness of the superconducting gap structure in the spectrum which is thought to depend on which the terminating layer is the BiO layer or the SrO layer, in Chapter 7.

Fig. 4.14 shows a typical example of the I - V curve and the tunneling spectrum indicating a superconducting energy gap. This spectrum has a flat background and a clear gap structure with a flat bottom and sharp peaks at the edges, revealing the feature of the BCS function. Considering the very narrow tunneling area in STM of an atomic order and uncertainty principle, this tunneling result on the BSCCO system strongly suggests an s -wave superconductivity with a gap which completely opens up at the Fermi surface. (We will discuss the gap symmetry in detail in section 5.6.4.) However, the superconducting spectra measured on the cleaved surface of BSCCO have some features contrary to the BCS theory at the same time. The superconducting gap (the way of estimating the gap value will be discussed in section 4.6.1) takes the gap energy 2Δ of 70-90 meV which corresponds to the reduced gap $2\Delta/k_B T_c$ of 9-12, if we take the peak-to-peak separation.

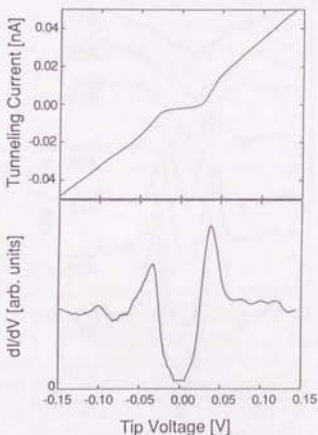


Fig. 4.14 Typical I - V and differential conductance curves showing a superconducting feature measured on the cleaved surface of a BSCCO single crystal at 4.2 K with $V_b = -300$ mV and $I_p = 0.1$ nA.

This value is much larger than that predicted from the BCS theory, *i.e.*, $2\Delta/k_B T_c = 3.52$. (It is not clear whether this simply means the strong electron-phonon coupling or not.) Although the temperature of the measurement was much lower than the T_c of the specimen, the smearing of the gap structure is quite remarkable. Furthermore, there often appears a diplike structure outside of the superconducting energy gap, which is enhanced especially in the occupied states (positive tip bias voltage) being consistent with the ARPES experiments. This structure can not be explained by the BCS theory. These anomalous features are also reported by other tunneling studies [Refs. 48, 49, 52; 63-65] and ARPES studies as discussed above [Refs. 18-27]. These features will be discussed in section 4.5, section 4.6.2 and Chapter 7.

4.3.3 Temperature Dependence of Superconducting Energy Gap

Fig. 4.15 demonstrates temperature dependence of the superconducting energy gap measured on the cleaved surface of an as-grown BSCCO single crystal. As the temperature increases, the

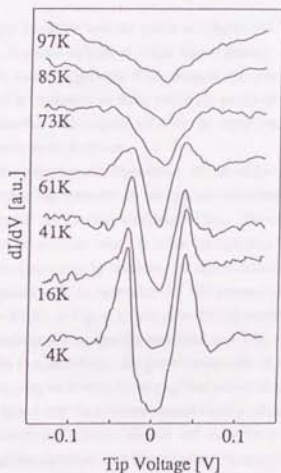


Fig. 4.15 Temperature dependence of the tunneling spectrum showing a superconducting gap measured on the cleaved surface of a BSCCO single crystal at 4.2 K with $V_b = -200$ mV and $I_p = 20$ nA.

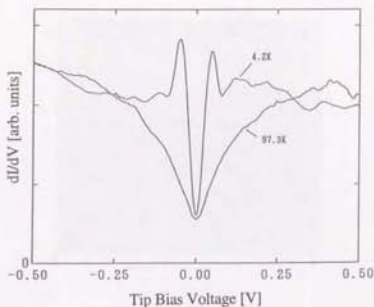


Fig. 4.16 Comparison between the tunneling spectra measured at 4.2 K and 97 K on the cleaved surface of a BSCCO single crystal with $V_b = -200$ mV and $I_p = 20$ nA.

conductance inside the gap increases and the peaks are depressed. The peak position does not change, and, near the T_c , it seems to shift to rather higher energy. The peak in the dI/dV curve should be shifted towards values larger than Δ/e , because the spectrum should be broadened by thermal smearing and there is no density of states inside the gap in the superconducting state. From this reason, we cannot take the peak-to-peak value as the superconducting energy gap value 2Δ when we discuss its temperature dependence.

In order to examine the temperature dependence of the superconducting energy gap, it is necessary to normalize a tunneling spectrum by the normal conductance curve at the temperature of the measurement and remove the thermal smearing effect. However, the critical field H_{c2} of BSCCO is very high at the temperature which is lower enough than the T_c , so that it is impossible to obtain the normal conductance curve by breaking the superconducting state with a magnetic field. A possible way of compromise is to normalize by the normal curve just above the T_c . The spectrum at 97 K ($> T_c = 89$ K) in Fig. 4.15 seems to be depressed around $V = 0$ with negative curvature. Fig. 4.16 superimposes the spectra measured at 4.2 K and 97 K with a larger energy scale. This result indicates that, basically, the gap structure still remains at 97 K which is higher than the T_c . This structure may be caused by strong fluctuation of the superconducting state near the T_c . Another possible idea is that the intrinsic normal density of states of this material has the V shape as predicted by some theories [Refs. 30, 32] and observed in the previous work [Ref. 7], although the observed negative curvature (not linear) cannot be explained from this point of view. According to the t - J model proposed by Fukuyama *et al.* [Refs. 66-68], the superconducting state appears under the T_c which is determined by the lower one between the temperature of the condensation of spinons into a spin singlet state (T_{RVB}) and the temperature of the Bose condensation of holons (T_B) (see Fig. 4.17). In the underdoped region where $T_{RVB} > T_B = T_c$, the

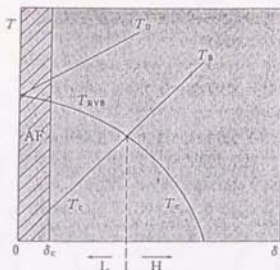


Fig. 4.17 Phase diagram according to the t - J model.

condensation of spinons occurs at higher temperature (T_{RVB}) than T_c which is said to be observed by nuclear magnetic resonance (NMR) as the spin gap [Refs. 69-73]. On the other hand, in the overdoped region where $T_B > T_{RVB} = T_c'$, the Bose condensation occurs in the electron system at $T_B > T_c'$. It is not clear how this is observed, however, the as-grown specimen, on which the temperature dependence of the spectrum shown in Figs. 4.15 and 4.16 were measured, is thought to be in the overdoped region, and the gaplike structure observed above T_c may possibly be related. Although the origin of the spectra depressed around $V = 0$ measured above T_c is not clear at the present, in any case, it is questionable that the spectra can be normalized by the normal conductance curve just above the T_c . From this reason, we do not discuss the temperature dependence of the superconducting gap any more.

4.3.4 Oxygen Content Dependence of Electronic Structure

As described in section 3.2.1, the hole concentration of the BSCCO system can be varied by changing oxygen nonstoichiometry or substituting Pb atoms for the Bi or Sr site, and the electronic nature of this system varies from semiconducting one to metallic one as carrier density increases. Wells *et al.* [Ref. 18] reported that the electronic structure of the surface BiO layer changed depending on the oxygen content. However, tunneling studies reported so far have never considered the oxygen content of the specimen. We measured tunneling spectra on the BSCCO single crystals of various oxygen content treated by various annealing conditions (see Table 3.1).

Fig. 4.18 indicates oxygen content dependence of the semiconducting spectra measured on the cleaved surfaces of BSCCO. Reduced specimens showed semiconducting spectra with wide band gaps, while oxidized specimens had narrower band gaps. In most cases of the measurements on the annealed single crystals, this type of semiconducting spectra were obtained. This is probably

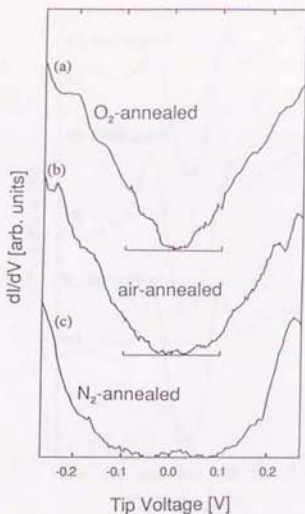


Fig. 4.18 Oxygen content dependence of the tunneling spectra showing a semiconducting feature measured on the cleaved surfaces of (a) oxygen-annealed, (b) air-annealed and (c) nitrogen-annealed BSCCO at 4.2 K. $V_b = -400$ mV and $I_p = 2$ nA.

because the homogeneity of the specimen had been improved by annealing, and the probability of the BiO termination had become higher. Especially on the O_2 -annealed specimens, atomic images of the surface BiO layers were often obtained. Considering these results, the electronic nature of the BiO layer varies from semiconducting nearly to metallic as the oxygen content increases. This is the same tendency as that of the bulk system of BSCCO as a function of the oxygen content.

Although it was very rare, we obtained tunneling spectra showing superconducting energy gaps on the annealed specimens (Fig. 4.19). We estimated the superconducting gap value for each of the specimens annealed in various atmospheres by taking the peak-to-peak values as the gap energy and averaging them. The N_2 -annealed specimen (T_c 81.7 K) and the O_2 -annealed one (T_c 82.9 K) showed averaged 2Δ values of 98.6 meV and 96.6 meV, respectively. On the other hand, the air-annealed specimens showed averaged 2Δ of 119.3 meV, corresponding to its higher T_c of 92.0 K. This result suggests that the variation of the oxygen content does not change the fundamental metallic nature of the CuO_2 plane, but changes the energy value of the superconducting

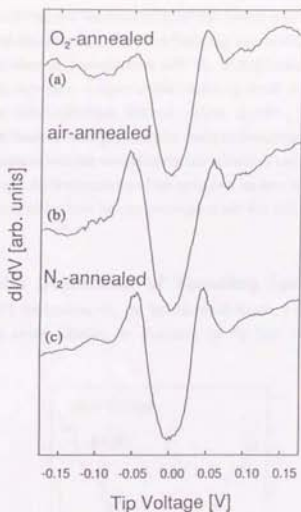


Fig. 4.19 Oxygen content dependence of the tunneling spectra showing a superconducting feature measured on the cleaved surfaces of (a) oxygen-annealed, (b) air-annealed and (c) nitrogen-annealed BSCCO at 4.2 K. $V_s = -400$ mV and $I_p = 2$ nA.

gap at the CuO_2 plane.

These results suggest a picture that the electronic nature of the bulk system of BSCCO is dominated by the oxygen content of the $(\text{BiO})_2$ layers which are sandwiched by the adjacent metallic $(\text{CuO}_2)_2$ layers. If the oxygen content decreases, the $(\text{BiO})_2$ layers become insulating and make the superconducting $(\text{CuO}_2)_2$ layers isolated, therefore the system has 2D properties. On the other hand, the increase of the oxygen content makes the $(\text{BiO})_2$ layers metallic, which couple the $(\text{CuO}_2)_2$ layers, and turns the bulk system 3D. However, the number of the examples of this type of superconducting spectra is not large enough to claim reproducibility about the averaged 2Δ values, and it is necessary to measure the specimens which have much lower T_c 's in order to ascertain the proportional relation between Δ and T_c .

In Fig. 4.18, the band gap of the semiconducting spectrum measured on the O_2 -annealed specimen is as small as about 50 meV. It gives us great interest whether or not the BiO layer becomes metallic and superconducting as the oxygen content increases more, concerning the

anisotropic nature and the strong two dimensionality of this system which become a difficulty in the way of the applications of this material. We tried tunneling spectroscopy on the specimen which had been annealed in 200 atom O_2 atmosphere at 600 °C. SQUID measurement showed the T_c of 74.5 K of this specimen, however, a reproducible tunneling result could not be obtained. The spectra measured on the same specimen showed various features, *i.e.*, an insulating nature, semiconducting ones with various band gap energies and a superconducting one. This is probably because the annealing treatment with the condition mentioned above caused decomposition or phase separation of the crystal, and the homogeneity of the specimen became rather worse. It is necessary to find the annealing process to increase the oxygen content without this problem.

4.3.5 Barrier Width Dependence of Tunneling Spectrum

In a series of STM/STS measurements, the tip-sample distance, *i.e.*, the barrier width of the tunneling junction can be easily adjusted by changing the tip bias voltage (V_p) or the set-point

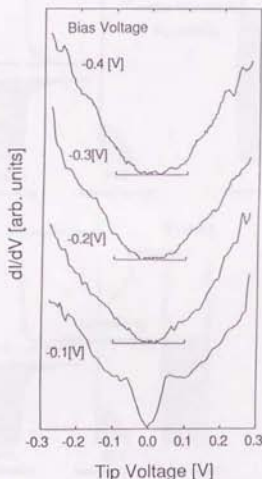


Fig. 4.20 Barrier width dependence of the tunneling spectrum measured on the cleaved surface of an air-annealed BSCCO single crystal at 4.2 K. $I_p = 2$ nA const. Zero conductance value is shown by the line under each spectrum.

current (I_p) operating the STM provided that the location of the tip on the surface is fixed and the work function and the density of states are constant. In the case of a planar junction, the width of the tunneling barrier is peculiar to each junction. Point contact and break junction method can change the barrier width, but it is not well-controlled. Considering these facts, this is a strong point of the STM/STS measurement, which, commonly, is not realized well.

We tried changing the barrier width and measuring tunneling spectra, when we obtained semiconducting spectra on the cleaved surface of a BSCCO crystal annealed in air. Fig. 4.20 demonstrates the tunneling spectra measured at various V_b 's from -0.4 V to -0.1 V for the constant I_t of 2 nA. In this case, the lower $|V_b|$ becomes, the narrower the tip-sample distance is, *i.e.*, the thinner the tunneling barrier is. At V_b 's from -0.4 V to -0.2 V, the spectrum shows basically semiconducting behavior. However, at $V_b = -0.1$ V, which means the much closer tip position to the sample surface, the spectrum clearly varies its shape. The gap structure, which is broadened a

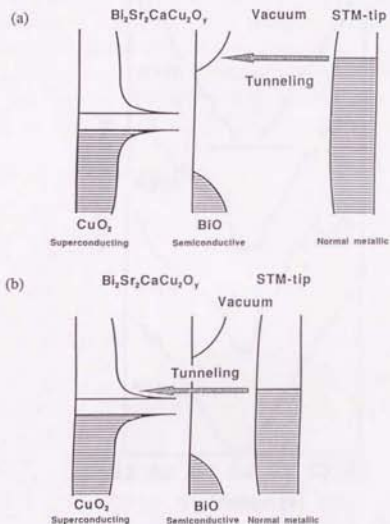


Fig. 4.21 Schematic diagram of the tunneling processes on the BiO terminated surface of BSCCO.

little but thought to reflect a superconducting energy gap, appears in the finite conductance which yields in the band gap region. The gap energy seems to correspond to the 2Δ value in the spectra showing a clear superconducting nature (Figs 4.10 and 4.14). The same tendency was observed on the (001) surfaces of YBCO thin films as will be presented in section 5.3.2. Shih *et al.* [Ref. 54] measured the cleaved surface of a BSCCO single crystal by STM in UHV at room temperature, and found that detectable conductance appeared in the semiconductive gap region only when the bias voltage was low (< 1.5 V) and the tip was close to the sample surface, which is consistent with our result shown in Fig. 4.20. They applied the vacuum resonance tunneling technique to estimate the absolute tip-sample separation and concluded that in this case the tip-sample distance was very small ($\sim 3\text{-}6$ Å).

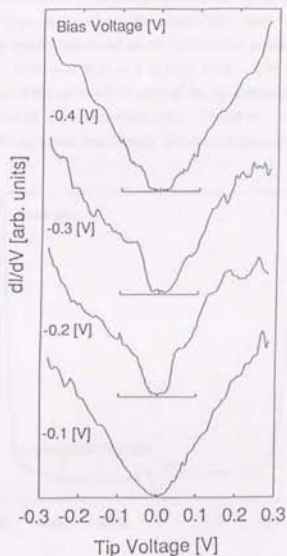


Fig. 4.22 Tunneling spectra measured with various barrier widths on the cleaved surface of an oxygen-annealed BSCCO single crystal at 4.2 K. $I_p = 2$ nA const. Zero conductance value is shown by the line under each spectrum.

Intuitively, this behavior can be explained as illustrated in Fig. 4.21. It is thought that the cleaved surface of BSCCO is covered with a semiconducting BiO layer, whose band gap can be estimated at -0.1 eV from the spectra in the case of Fig. 4.20, and a superconducting CuO_2 layer lies under the surface BiO layer with an average depth of 4.5 \AA . When the STM tip is far from the sample surface, the tunneling spectrum is strongly influenced by the presence of the semiconductive surface BiO layer which is closer to the tip by $\sim 4.5 \text{ \AA}$ than the CuO_2 layer. The spectrum indicates the semiconducting feature reflecting the electronic nature of the surface BiO layer [Fig. 4.21(a)]. However, if the bias voltage is adjusted at the energy where the surface BiO layer does not have enough density of states [note that Fig. 4.20(a) shows little density of states at the energy level of 0.1 eV], the tip is brought into the proximity region to the sample surface, which gives rise to the finite probability of the tunneling into the underlying CuO_2 layer [Fig. 4.21(b)]. Therefore the electronic properties contributed from the superconducting CuO_2 layer become dominant in the initially semiconducting gap region where the surface BiO layer has no density of states [Fig. 4.20(d)]. The tunneling spectra measured on an O_2 -annealed specimen did not show remarkable difference at various V_b 's from -0.4 V to -0.1 V (Fig. 4.22). This result is understandable if we consider that the band gap of the surface BiO layer of the O_2 -annealed BSCCO is smaller (~ 0.06 eV from Fig. 4.22) than that of the air-annealed one. Therefore, in the case of the O_2 -annealed specimen, the surface BiO layer still has density of states at the energy level of 0.1 eV, so that the

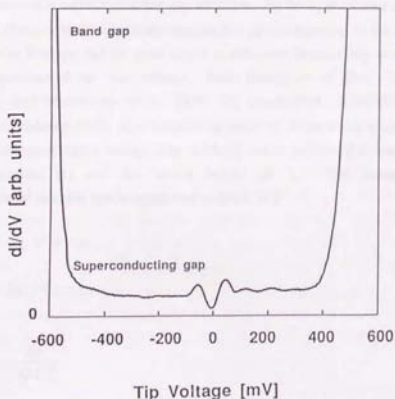


Fig. 4.23 Tunneling spectrum measured at 4.2 K on the cleaved surface of a BSCCO single crystal after storage in vacuum for 12 hours. $V_b = -800$ mV and $I_p = 1.65$ nA.

STM tip is at the further position if compared to the case on the air-annealed specimen even under the same tunneling condition, *i.e.*, $V_b = 0.1$ V, $I_p = 2$ nA, and the tunneling probability into the CuO_2 layer is negligible.

The conclusion obtained here is that the tunneling spectrum measured on the cleaved surface of BSCCO with a thin tunneling barrier is composed of two components: one is contribution from the surface BiO layer, and the other is from the underlying CuO_2 layer beneath it, and if the surface BiO layer has density of states near E_F , it conceals the superconducting feature of the CuO_2 layer. In order to confirm the legitimacy of this conclusion, we tried another experiment. If we can make the band gap of the surface BiO layer wider than usual, the superconducting feature of the CuO_2 band must be observed more clearly because of the disappearance of the surface states near the E_F . As discussed above in section 4.3.4, the band gap energy of the BiO layer depends on the oxygen content. We performed STS measurements on the cleaved surfaces of the air-annealed BSCCO single crystals which had been stored in the vacuum chamber for 12 hours in order to deplete oxygen of the surface BiO layer (Fig. 4.23). As a result of widening the band gap of the surface BiO layer by oxygen depletion, the spectrum shows the separated BiO (or SrO) bands and low residual density of states, in which a clear superconducting gap structure with pileup peaks at the gap edges can be observed, in the band gap region. We will give a quantitative discussion about this barrier width dependence of the tunneling spectrum in section 4.6.3.

Fig. 4.24, on the other hand, demonstrates the result of the same measurement obtained when the spectrum showed a clear superconducting gap structure. As the V_b decreases from -0.35 V to -0.03 V, the spectrum changes in the systematic manner that the background of the spectrum varies from V-shape to inverse V-shape and the peak height is enhanced dramatically and the peak position is essentially independent of the bias voltage. Both Huang *et al.* [Ref. 74] (point contact on $\text{Ti}_2\text{Ba}_2\text{CaCu}_2\text{O}_y$) and Matsumoto *et al.* [Ref. 75] ($\text{Au/Bi}_2\text{Sr}_2\text{CuO}_y/\text{BSCCO}$ planar junctions) reported the same tendency of the superconducting spectrum as the result shown in Fig. 4.24. The increased conductance at higher energy [Fig. 4.24(a)] can be explained in terms of the variation of the barrier thickness (t) and the barrier height (ϕ). The tunneling current for a metal-insulator-metal junction can be expressed as [Ref. 76]

$$I(V) = \alpha V + \gamma V^3 + \dots \quad (4.1)$$

$$G(V) = \alpha + 3\gamma V^2 + \dots \quad (4.2)$$

$$\frac{\gamma}{\alpha} = \frac{(Ae)^2}{96\phi} - \frac{Ae^2}{32\phi^{1/2}} \quad (4.3)$$

$$A = \frac{2t}{h} \sqrt{2m} \quad (4.4)$$

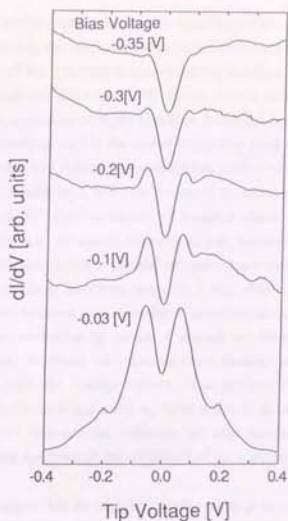


Fig. 4.24 Barrier width dependence of the tunneling spectrum originally showing a superconducting gap structure measured on the cleaved surface of an as-grown BSCCO single crystal at 4.2 K. $I_p = 20$ nA const. Zero conductance value is shown by the line under each spectrum.

The parabolic component of the tunneling conductance, γ/α value, is approximately proportional to the square of the barrier thickness and inversely proportional to the barrier height, thus, when the barrier thickness becomes large, the parabolic component increases. Therefore, if the voltage becomes a considerable fraction of the barrier height, its effect on the $I(V)$ cannot be neglected, and one customarily finds an increased conductance at higher voltages which takes a parabolic form about $V = 0$, which has offset for an asymmetric shape barrier. On the other hand, Fig. 4.24(e) shows very high conductance around $V = 0$. This spectrum is accompanied by the bilateral dip structure indicating the presence of a microscopic short circuit which has small J_c , so that this high conductance near zero bias can be contribution from ohmic current through the short circuit. However, the decreasing high-voltage conductance in Figs. 4.24(c) and 4.24(d) cannot be explained by these effects. Huang *et al.* proposed an assumption that the CuO_2 band has strongly energy dependent $N_s(E)$ which heaps near the E_f [Ref. 64]. They speculated that the $N_s(E)$ of this

system originally decreases at higher energy, and when the barrier width is large and the parabolic component is overwhelming, the spectrum shows rather increasing conductance at higher voltage, resulting in the manner of the spectrum shape variation depending on the barrier width shown in Fig. 4.24. This assumption can explain the diplike feature outside the superconducting gap structure by thinking of asymmetry of $N_s(E)$ as will be discussed in section 4.5.

Halbritter *et al.* explained our data by the model which they proposed [Ref. 77]. Their model can be summarized as follows: The cuprate superconductors have a narrow, quasi-2D *p-d* conduction band with a low carrier density ($n_s \geq 10^{21} / \text{cm}^3$) close to the metal-insulator transition occurring in two dimensions for $n_s \leq 10^{21} / \text{cm}^3$ as density of localized states. Thus any perturbation of the delicate *p-d* hybridization, *i.e.*, of spatial, energetical, and directional order, renders the cuprates insulating. Such perturbations occur at internal or external *a-b* surfaces by intrinsic relaxation or strain fields. All this yields an insulating seam (≥ 1 nm) with $n_s \leq 10^{21} / \text{cm}^3$. This intrinsic insulating seam with its localized states weakens superconductivity and supports tunneling in various channels. The weakening by on-site Coulomb repulsion close to the metal-insulator transition smears out and roughens the metal-insulator interface and, *e.g.*, causes reduced and locally varying energy gaps and leakage current. The different tunneling channels, direct and resonant or intermediate *via* localized states n_s , have different distance, temperature, and voltage dependencies. We will discuss the influence of this barrier width dependence of the superconducting tunneling spectrum on the estimation of the superconducting energy gap in section 4.6.1.

These observations suggest that the tunneling barrier width is an important determining factor of the tunneling spectrum in the case of the HTSC's. However, most of the tunneling studies reported so far disregarded this effect of barrier width, which would not be allowed in this case. Even in the case of a uniform superconductor, it was theoretically predicted that the reduction of the barrier height leads to the apparent increase in the midgap conductance [Refs. 78, 79].

4.3.6 Energy Resolution Dependence of Superconducting Spectrum

Figs. 4.25(a)-4.25(c) demonstrate typical examples of the spectra showing a superconducting energy gap obtained at various energy resolutions, which were 60 meV [Fig. 4.25(a)], 6 meV [Fig. 4.25(b)] and 1.5 meV [Fig. 4.25(c)], respectively. These show the differential conductance calculated based on recorded *I-V* characteristics as a function of *V*, as discussed in section 3.1.3. When the energy resolution was low [Fig. 4.25(a)], the spectrum shows extremely high zero-bias conductance which is more than 70 % of the normal one and a broad superconducting gap structure. At the high resolution of 1.5 meV, one can see a flat bottom region with low zero-bias conductance of 5 %. It is most likely that the spectrum shape with the higher energy resolution reflects an intrinsic feature.

This result suggests the significance of sufficiently high energy resolution in the observations of superconducting energy gaps of the HTSC's. Most of the other tunneling studies and PES studies

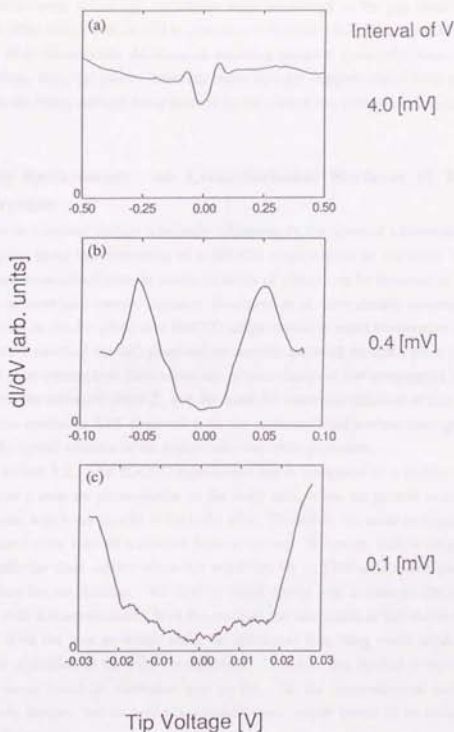


Fig. 4.25 Tunneling spectra showing a superconducting gap measured on an as-grown BSCCO single crystal at 4.2 K with different voltage intervals. Voltage intervals of the measurements are (a) 4.0 mV, (b) 0.4 mV and (c) 0.1 mV. The total energy resolution is fifteenth as large as the interval. The numbers of the data points are 500 for all the spectra.

on the BSCCO system reported gapless features of the spectra and asserted d -wave symmetry of the Cooper pair of this system [Refs. 23, 24, 49, 51]. However, if we consider our present result, it seems that, in these cases, the energy resolutions were not enough or the gap structures were broadened by some other effects (which will be discussed in section 4.6.2). Since the STM tip is a microscopic probe of an atomic scale, the observed tunneling spectrum gives information averaged over the Fermi surface, thus, the present tunneling result strongly suggests that a finite gap opens up at every point on the Fermi surface, being favored by the s -wave like pairing mechanism.

4.4 Tunneling Spectroscopy on Cross-Sectional Surfaces of BSCCO Single Crystals

The measurement on a cleaved surface is strongly influenced by the nature of a terminating layer, and there is ambiguity about the termination of a BSCCO single crystal as discussed in section 4.3.2. The cross-sectional observation in which all kinds of planes can be observed at the same time is expected to be more informative. Actually, Hasegawa *et al.* have already succeeded in the STM/STS observation on the b - c plane of a BSCCO single crystal at room temperature [Ref. 7], and the semiconductive nature of the BiO plane and the metallic nature of the CuO₂ plane have been concluded. It is of great interest how these electronic natures change at low temperature below the T_c in connection with the extremely short ξ_c and the quasi-2D electronic structure of this system. The cryogenic atomic resolution STS observation on the cross-sectional surface must give direct information about the spatial variation of the superconducting order parameter.

As described in section 3.2.1, the BSCCO zone-melted rod is composed of a number of piling single crystals whose c -axes are perpendicular to the rod's axis, since the growth occurs in the direction of a - b planes which are parallel to the rod's axis. Therefore, the cross-sectional surface can be always obtained if we slice off a disklike piece of the rod. However, there is no good way to obtain an atomically flat clean surface which has suitability for an STM observation because the cross-sectional surface has no cleavage. We filed the sliced crystal with a diamond file and made the surface smooth with a diamond sheet. With this method, the orientation of the obtained surface cannot be expected if we see it on an atomic scale. In addition to that, filing yields small particles which often become a problem in the STM measurement. Therefore this method is not ideal one although we have never found an alternative way so far. On the cross-sectional surface, we obtained some atomic images, but no well-characterized ones, which seems to be owing to the problem described above.

The tunneling spectroscopy on the cross-sectional surface gave two typical types of superconducting spectra whose gap energy values were different as shown in Fig. 4.26. One indicated the superconducting gap whose gap energy is $2\Delta \sim 80$ meV if we take the peak-to-peak separation, which is almost as large as the value measured on the cleaved surface [Fig. 4.26(a)]. This type of spectrum was often accompanied by the diplike feature outside the pileup peaks. The

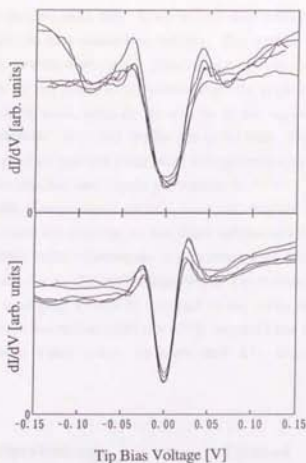


Fig. 4.26 Examples of the tunneling spectra measured on the cross-sectional surface of BSCCO at 4.2 K, showing superconducting gaps classified into two sizes. $V_b = -200$ mV and $I_p = 2$ nA.

other showed a relatively small energy gap of $2\Delta \sim 50$ meV, which has never been observed on the cleaved surface [Fig. 4.26(b)]. This type of spectrum has never been observed with the diplane feature. All the superconducting spectra measured on the cross-sectional surface belonged to either of these two types, and the spectra with some energy gap values in between have never been obtained. Fig. 4.26 superimposes some examples of the measured spectra showing that they can be divided into the two groups.

If the superconducting order parameter has a spatial variation along the c -axis in one unit cell intrinsically, it should change gradually. Thus it cannot explain the observed result. Although the extrinsic effects such as oxygen defects and substitution atoms can vary the local T_c , there is no reasons why the smaller gap has always the same gap value of $2\Delta \sim 50$ meV. The features of the observed two types of spectra shown in Figs. 4.26(a) and 4.26(b) seem to be similar to the features of the ARPES spectra observed by Wells *et al.* [Ref. 18] along the Γ - \bar{M} direction and the Γ - \bar{X} direction, respectively. However, in STM, k -dependent features cannot be distinguished because of the narrow tunneling area of an atomic scale, which means a wide area in the k -space considering uncertainty principle (see section 5.6.4 in details). Klemm *et al.* reported in their SN model that the top superconducting layer can have a significantly larger energy gap than the bulk provided that the

top layer is electronically isolated [Ref. 80]. If we believe their model calculation, the observed result shown in Fig. 4.26 can be explained as follows: The surface obtained by filing is not atomically flat but has step structures where a - b planes appear. When the STM tip is near the step and the tunneling occurs to the a - b plane, the spectrum reflects the larger gap opening in the band of the surface states. On the other hand, when the tip is on the terrace region and the tunneling occurs to the edge surface, the spectrum shows the smaller gap of the bulk. However, according to their model, this interpretation gives an opposite result about the appearance of the diplike feature, *i.e.*, a smaller gap with the diplike structure and a larger gap without it.

The spectrum data of the cross-sectional surfaces were not obtained on the well-characterized surfaces with the atomic resolution imaging, so that much information could not be derived from the data. In order to obtain more information, it is necessary to establish the method of the preparation of an edge surface, *e.g.*, chemical etching which was performed on YBCO [Ref. 81]. Another possible way is to employ a BSCCO thin film of not c -axis orientation with a smooth surface. The BSCCO system has neither (100) nor (110) oriented films unlike the YBCO system, but has (11n) oriented films whose c -axes are tilted [Ref. 82], which may allow interesting observations.

4.5 Tunneling Spectroscopy on Cleaved Surfaces of $\text{Bi}_{1.8}\text{Pb}_{0.4}\text{Sr}_{1.8}\text{CaCu}_2\text{O}_y$ Single Crystals

Substitutional doping of metals in the HTSC materials has been employed extensively in attempts to improve and elucidate the superconducting properties of these materials. It is well known that Pb substitution for the Bi site does not decrease the T_c of BSCCO. Sunshine *et al.* reported that Pb substitution in the BSCCO system enhanced the onset of the T_c from 84 K to 107 K [Ref. 83], since then, numerous studies on the Pb-substituted BSCCO have been reported [Refs. 84-90]. In polycrystalline $(\text{BiPb})_2\text{Sr}_2\text{Ca}_{n-1}\text{Cu}_n\text{O}_y$ materials, Pb substitution has been found to enhance the formation of the $n=3$ ($T_c \sim 110$ K) phase vs. the $n=2$ ($T_c \sim 80$ K) phase [Refs. 84, 88], although the lattice parameters and the T_c 's for a given phase do not vary substantially [Refs. 87, 88]. In addition, electron-diffraction [Refs. 84-86], XRD [Refs. 87, 88] and STM [Ref. 4] studies have shown that the modulation structure observed in the parent BSCCO material changes with Pb substitution. The effect of hole doping by Pb substitution for Bi on the electronic structure of the BSCCO system is of great interest in terms of the comparison with the effect by oxygen nonstoichiometry.

We observed the cleaved surfaces of $\text{Bi}_{1.8}\text{Pb}_{0.4}\text{Sr}_{1.8}\text{CaCu}_2\text{O}_y$ single crystals grown by a floating zone method. We employed as-grown specimens of $T_c = 82.5$ K, which are thought to have the same hole concentration as the O_2 -annealed BSCCO specimens. On these specimens, atomic resolution imaging has never been achieved, and the tunneling spectra always showed a superconducting feature [Fig. 4.27]. This behavior is similar to the results on the as-grown

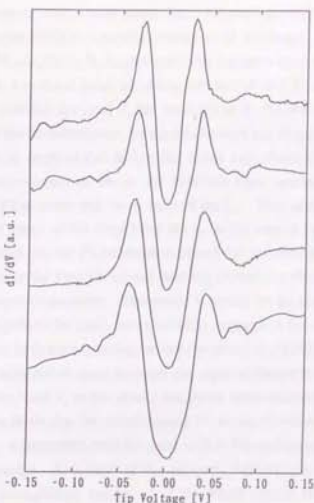


Fig. 4.27 Examples of the tunneling spectra measured at 4.2 K on the different cleaved surfaces of the same $\text{Bi}_{1.8}\text{Pb}_{0.4}\text{Sr}_{1.8}\text{CaCu}_2\text{O}_7$ single crystal, showing various values of superconducting gap energy. $V_b = -200$ mV and $I_p = 2$ nA.

BSCCO specimens, however the probability of getting superconducting spectra is much higher in this case. It is likely by analogy that the superconducting CuO_2 layer is covered with the surface layer which has no density of states near the E_F as discussed in section 4.3.2. On the other hand, Zhang *et al.* reported that they observed the cleaved surfaces of $\text{Bi}_{2-x}\text{Pb}_x\text{Sr}_2\text{CaCu}_2\text{O}_7$ ($x=0, 0.3, 0.7$) single crystals at room temperature in Ar atmosphere, and tunneling spectra measured on the surfaces on which atomic resolution images were obtained showed a semiconductive feature which varied to slightly metallic with a small tip-sample separation [Ref. 91]. This observation is analogous to our result obtained mainly on the air- or O_2 -annealed BSCCO whose surface is thought to be covered with the semiconducting BiO layer with a narrow band gap. The difference between their result and ours must arise from the difference of the surface layer.

Fig. 4.27 demonstrates tunneling spectra showing superconducting gaps observed on the same $\text{Bi}_{1.8}\text{Pb}_{0.4}\text{Sr}_{1.8}\text{CaCu}_2\text{O}_7$ single crystal in different measurements. Before each measurement, a clean surface was obtained by cleaving. As shown in the figure, the gap energy value 2Δ (peak-to-peak

separation) indicates scattering over a wide range from ~ 40 meV to ~ 100 meV, which has never been observed on the parent BSCCO crystals. Huang *et al.* measured tunneling spectra on the cleaved surfaces of $\text{Bi}_{1-x}\text{Pb}_x\text{Sr}_2\text{CaCu}_2\text{O}_y$ single crystals by a point contact method, and obtained an essentially same tendency, *i.e.*, the Δ value spreading between 16 and 30 meV [Ref. 64]. Judging from these results, it is clear that the local T_c has variation in Bi-Pb-Sr-Ca-Cu-O crystals. It has been widely believed that the Pb substitution for the Bi site does not degrade the superconductivity of this system. Zhang *et al.* reported that the unfilled states 1 eV above the Fermi level decreased systematically as the concentration of Pb in the Bi(Pb)O layer increased, and there was no remarkable change in the filled states and the vicinity of the E_F . They attributed this behavior to a decrease in the density of states of the $\text{Bi}6p$ band [Refs. 8-10] caused by the increase of the Pb concentration, and concluded that the Pb substitution causes the variation in the electronic structure sufficiently far removed from the Fermi level and does not perturb the electronic states near the E_F which is essential for superconductivity. However, it seems to be contradictory for them to conclude that Pb does not perturb the CuO_2 states which is responsible for superconductivity in this system, because their result is thought to mainly reflect the nature of the Bi(Pb)O layers. We would like to claim that the Pb substitution does suppress the superconductivity in the BSCCO system, because the variation of the local T_c in the crystal has never been observed in the parent BSCCO single crystals. It is most likely that the substitutional Pb atoms concentrate in some parts of the crystal where the local T_c is decreased, and the parts of low Pb concentration form a network of high T_c superconducting passes. As a result of this network, macroscopic observations measuring resistivity and magnetic susceptibility behave as if the whole crystal had high T_c without the influence of the Pb substitution.

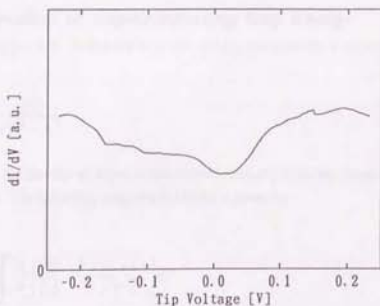


Fig. 4.28 Tunneling spectrum measured on the cleaved surface of a $\text{Bi}_{1.8}\text{Pb}_{0.2}\text{Sr}_{1.8}\text{CaCu}_2\text{O}_y$ single crystal at room temperature.

The superconducting spectra shown in Fig. 4.27 exhibit an asymmetric characteristic which appears as a dip just outside a pileup peak of the superconducting gap in occupied states (positive tip bias voltage) and a shoulder or a weak dip at the same energy in unoccupied states (negative tip bias voltage). This asymmetry was observed on the cleaved surfaces of the parent BSCCO, and consistent with other tunneling works on BSCCO [Ref. 49] and Bi-Pb-Sr-Ca-Cu-O [Ref. 64]. This asymmetric feature can be explained if we assume that the CuO_2 band has a strongly energy dependent asymmetric $N_s(E)$ with a heap near the E_F , which we discussed in section 4.3.5. Since the normal state conductance is a convolution of the usual parabolic tunneling conductance [Ref. 91] and the $N_s(E)$, the tunneling spectrum reflecting the CuO_2 band in the normal state must show a combination of a valley around zero bias caused by the parabola and decreased conductance at higher voltage owing to the $N_s(E)$, *i.e.*, a double heap structure. If this structure is asymmetric and the heap in the positive side of the tip bias voltage is the higher, this yields the diplike feature which asymmetrically appears in the superconducting spectra. Fig. 4.28 shows the tunneling spectrum measured on the cleaved surface of a $\text{Bi}_{1-x}\text{Pb}_x\text{Sr}_y\text{CaCu}_2\text{O}_7$ single crystal at room temperature. The spectrum indicates metallic behavior, and is thought to reflect mainly the nature of the CuO_2 layer as discussed above. The most important feature of this spectrum here is an asymmetric shape and a remarkable heap in the positive tip bias voltage region. This asymmetric normal conductance curve seems to give the diplike structure if we imagine that a superconducting gap opens near the E_F in this spectrum. This result seems to be consistent with the assumption described above.

4.6 Discussions

4.6.1 Estimation of Superconducting Gap Energy

The BCS theory predicts the density of states of the quasi-particles is expressed as

$$\frac{N_s(E)}{N_n(E)} = \frac{|E|}{\sqrt{E^2 - \Delta^2}} \quad (4.5)$$

where $N_n(E)$ is the density of states in the normal state, $N_s(E)$ in the superconducting state and Δ is the energy gap. The tunneling conductance $G(E)$ is given by

$$\frac{G_s(V)}{G_n(V)} = \int \frac{N_s(E)}{N_n(E)} \left[\frac{\partial f(E+V)}{\partial V} \right] dE \quad (4.6)$$

where $f(E)$ is the Fermi function [Ref. 76]. This should be fitted to the experimental tunneling spectrum data to compare the density of states of the quasiparticles in HTSC's with the BCS

theory. However, this procedure is not applicable to most cases of the HTSC's because the normal conductance $G_n(E)$ at low temperature cannot be obtained by breaking superconductivity with applying a magnetic field owing to the high critical fields of these materials in the temperature range of $T \ll T_c$. For this reason, an appropriately assumed curve extrapolated from the higher bias voltage region, or the tunneling conductance measured above T_c is often used instead of experimentally determining $G_n(E)$.

As discussed in Chapter 1, the conductance curves measured on the HTSC materials have been observed to deviate significantly from Eq. 4.6. Therefore, the way of estimating the superconducting gap value Δ from the experimental data has been involved in confusion. The estimation methods often used are as follows:

- 1) The peak-to-peak separation of the derivative conductance $G_i(V) = dI/dV$ is adopted as 2Δ .
- 2) The I^2-V^2 curve is extrapolated from the outer-gap region to $I^2 = 0$ to define Δ .
- 3) A Gaussian distribution of the gap value in Eq. 4.5 is assumed to take account the material inhomogeneity of the junction, yielding

$$\frac{G_i(V)}{G_n(V)} = \iint \frac{1}{\sqrt{2\pi}\delta\Delta} \exp\left[-\frac{(\Delta - \Delta_0)^2}{2\delta\Delta^2}\right] \frac{N_i(E)}{N_n(E)} \left[-\frac{\partial f(E+V)}{\partial V} \right] dE d\Delta \quad (4.7)$$

where $\delta\Delta$ is the standard deviation of Δ . The curve obtained by this equation is fitted to the conductance spectrum to derive Δ .

- 4) The Dynes equation, Eq. 4.8, which was originally introduced to consider the effect of quasi-particle recombination near a metal-insulator transition [Refs. 92, 93], is often used in Eq. 4.6 instead of Eq. 4.6, to fit the tunneling conductance to obtain the gap value Δ (see section 2.1.3).

$$\frac{N_i(E)}{N_n(E)} = \text{Re} \left\{ \frac{E - i\Gamma}{[(E - i\Gamma)^2 - \Delta^2]^{1/2}} \right\} \quad (4.8)$$

The imaginary part $\Gamma = (\hbar/2\pi)\tau$, τ is lifetime of a quasi-particle.

- 5) The background in the conductance curve is interpolated to the gap region, and the gap $2\Delta/e$ is estimated from the interval between the two crossing points with the curve. This should be a good approximation for the Dynes equation as long as the damping parameter Γ is not large compared with Δ .

Now we discuss the applicability of these methods to the HTSC's. The I^2-V^2 curve is observed to be not linear for HTSC materials, hence 2) is not available for the current purpose. 3) accounts for the gap smearing in a macroscopic junction, but cannot be adopted for analysis of the data measured by a microscopic method like STM. 4) has been often employed to estimate the gap value and actually the resultant $G_s(E)$ curves have fit the data well in many cases. However, this is not surprising because the Dynes equation introduces a new adjustable parameter Γ , which makes the fitting much easier than the original BCS function. For the application of the Dynes equation which has physical meaning, it is necessary for the Γ value to be physically reasonable and consistent with measurements of other related quantities. Most of the previous works employing this method reported quite large Γ values, and in these studies, the Dynes equation seems to have been used for fitting to the superconducting gap structure, which was extrinsically broadened, without any physical grounds. Furthermore, we found that the superconducting gap varies its shape depending on the barrier width as discussed in section 4.3.5 (see Fig. 4.24). Since the peak height is different for each spectrum, the Γ values derived from the spectra should have variation. We have no way

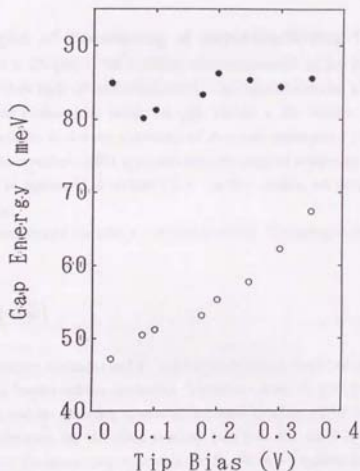


Fig. 4.29 Gap energies estimated from the peak-to-peak separation (closed circle) and the interpolation method (open circle) as a function of tip bias voltage V_b . $I_p = 20$ nA const.

to determine which spectrum is intrinsic. Hence, it is not clear whether or not the application of the Dynes equation to the tunneling data on HTSC's is physically meaningful.

As a result of elimination, only 1) and 5) remain. Fig. 4.29 demonstrates plots of the gap energies estimated from the peak-to-peak separation and the interpolation method as a function of the barrier thickness. The lower tip bias voltage means the thinner barrier width because of the constant set point current. This result obviously tells us that the interpolation of the tunneling spectrum according to 5) should not be justified because the gap value obtained by this method shows a tendency to increase as the barrier thickness increases. On the contrary, the peak-to-peak value is kept constant independent of the barrier width, so that the 2Δ value estimated by 1) should carry some intrinsic information. Finally, we would like to point out the fact that 1) gives a larger gap value than the true one, considering the effects of thermal smearing and the quasi-particle damping described above. Especially at the temperature near the T_c , the peak is shifted towards values larger than Δ by the smearing since $N_s(E) = 0$ inside the gap, and the pair breaking rate Γ increases rapidly, which enhances the difference between the peak position and the actual Δ . Therefore the gap value obtained by 1) should be regarded as the maximum possible value.

4.6.2 Origins of Broadening of Superconducting Gap Structure

As discussed in Chapter 1, the tunneling spectra measured on the HTSC's tend to be broadened irrespective of their high critical temperatures. The superconducting gap is observed with smeared peaks and finite conductance inside the gap without a flat bottom. These features have been discussed in relation to d -wave symmetry of the order parameter. However, our tunneling data measured by the cryogenic STM apparatus strongly suggest s -wave symmetry in both BSCCO and YBCO as will be discussed in section 5.6.4. In this section, we propose possible origins of this gap broadening.

First of all, we should consider a technical problem. Tunneling resistance (R_T) of a junction has the relation

$$R_T \propto \exp\left(-\sqrt{\bar{\phi}}t\right) \quad (4.9)$$

where t is the barrier thickness and $\bar{\phi}$ is the average barrier height which depends on the substance of the tunneling barrier and the electrodes. Therefore, when the junction has a thick barrier, the R_T becomes large, and the tunneling current (I) becomes small provided that the bias voltage (V) is the same. If we measure the tunneling junction with high R_T , the I is small especially at low V 's corresponding to the energy region around the E_F where a superconducting gap appears. Hence a signal/noise ratio becomes small in this case, resulting in the broadening of the superconducting gap structure. STM can solve this problem by making the tip position close to the sample surface. A point contact method and a break junction can vary the R_T by changing the pressure, however it is

quite difficult to decrease the R_T without making micro short circuits which yield leakage current. In the case of a planar type junction, the R_T of the junction is determined by the material of the insulating layer and its thickness. Although a thin insulating barrier is desirable, it cannot often avoid forming pin holes.

Next, we have to take into account the extrinsic effects such as inhomogeneity of the sample, oxygen depletion and chemical reaction. If the junction has a wide interface, the local T_c must have variation owing to these effects. Since the tunneling spectrum gives the information integrated over the wide junction area, this spatial variation of the Δ causes the smearing of the superconducting gap structure in the spectrum. This effect can be taken into account by assuming a Gaussian distribution of the gap value as discussed in section 4.6.1. The STM can avoid this problem because it is a local probe method.

There is possibility that the gap structure dimly observed on the HTSC is an intrinsic feature. In the original BCS theory, the gap parameter Δ for $|E| < \hbar\omega_c$ was estimated to be constant where E is the kinetic energy relative to the E_F , i.e., isotropic s -wave symmetry [Ref. 94].

$$\Delta(k) = \Delta = \text{const.} \quad (4.10)$$

Even if the Cooper pair has s -wave symmetry, the gap parameter in the HTSC which is highly anisotropic in the Fermi surface may not be constant, but could depend on k (anisotropic s -wave). Schneider *et al.* derived an anisotropic gap in the form shown in Eq. 4.11 with a multi-layer superconductor model, considering the interactions in and across two different planes with a spacing s [Ref. 95].

$$\Delta(k) = \Delta_1 - 2\Delta_2 \cos(k_x s) \quad (4.11)$$

Kirtley *et al.* [Ref. 96] proposed a model assuming the gap anisotropy to be

$$\Delta(k) = \Delta_a \sin^2 \theta - \Delta_c \cos^2 \theta \quad (4.12)$$

where θ is the angle between k and the c -axis (Fig. 4.30). As will be discussed in section 5.6.4, the tunneling spectrum measured by STM gives information integrated all over the k -space, considering the small tunneling area of an atomic scale. In the macroscopic junction method, the tunneling current may be composed of electron transfer with momentum both parallel and perpendicular to the simply assumed tunneling direction because of electron diffraction at atomic-scale step structures on the junction interface. This is more realistic case than the perfect junction of an atomically flat interface where the transverse momentum will be conserved, i.e., coherent tunneling process. Thus the tunneling spectrum measured by the macroscopic junction method must reflect the density of states averaged in the k -space. Therefore, if the HTSC's have isotropic s -wave symmetry of the Cooper pair as expressed in Eq. 4.10, the spectrum shows a clear

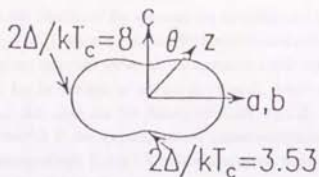


Fig. 4.30 Anisotropic gap symmetry determined by Eq. 4.12 proposed by Kirtley *et al.* [Ref. 96].

superconducting gap structure. However, if the anisotropic *s*-wave pair symmetry such as Eq. 4.11 and Eq. 4.12 is true, a broadened gap structure is observed in the tunneling spectrum intrinsically. The latter case seems to be more credible considering the highly anisotropic nature of the HTSC materials.

Finally, we would like to point out the possibility that the variation of the superconducting order parameter in the real space can be also the origin of the observed gap broadening of the HTSC's. We will discuss this point in Chapter 7.

4.6.3 Explanation for Spectrum Variation Depending on Barrier Width

As discussed in section 4.3.5, when the cleaved surface of a BSCCO single crystal was terminated with the BiO layer, the tunneling spectrum showed a semiconducting feature with the STM tip at the usual position of the scanning mode. However, as the tip approached closer to the sample surface, finite conductance appeared in the initially band gap region and a superconducting gap was observed in it (Fig. 4.20). Shih *et al.* [Ref. 54] and Zhang *et al.* [Ref. 91] also reported the same tendency of the change of the spectrum feature from semiconductive to metallic as the tunneling barrier became thinner, which was measured at room temperature. In section 4.3.5, we presented an intuitive interpretation assuming that the tunneling spectra is composed of two components: one is originating from the surface BiO layer, and the other from the underlying CuO₂ layer.

This phenomenon becomes easy to be understood if we divided the energy level into three regions in relation to the energy of the band gap edge of the surface BiO states (E_{bg}). In the energy region of $|E| \gg |E_{bg}|$, the surface BiO layer has enough density of states, so that the electronic feature of the BiO layer appears predominantly in the spectrum, independent of the barrier width, because the BiO layer is closer to the tip than the CuO₂ layer by the average distance of 4.5 Å. On the other hand, in the region $|E| < |E_{bg}|$, the surface BiO layer has no density of states, hence, when the tip approaches the sample surface, finite probability of tunneling between the tip and the CuO₂ layer yields, and superconducting characteristics appear in the band gap region of the BiO layer. In

these two energy regions, the behavior of the spectrum can be understood intuitively. However the behavior in the region $|E - E_{g/2}|$, where the surface BiO layer has not zero but very low density of states and two energy regions described above are connected, is a little complex and seems not to be explained by intuition. Let us take note of one energy value E_1 , which satisfies the relation $E = E_{g/2}$ and where the surface BiO layer has low density of states, e.g., $E_1 = 0.1$ eV in Fig.4.20. When the bias voltage is 0.4-0.2 V, the spectrum shows a small conductance value at $V_1 = 0.1$ V. However the spectrum measured with $V_b = 0.1$ V indicates relatively large conductance just outside the superconducting gap at $V_1 = 0.1$ V which seems to be comparable to the normal conductance of the CuO_2 band. This suggests that, in the spectrum of $V_b = 0.1$ V, the contribution to the conductance at $V = V_1 = 0.1$ V from the CuO_2 layer [$G_{\text{CuO}_2}(V_1)$] is larger than that from the surface BiO layer [$G_{\text{BiO}}(V_1)$], which is upside-down when $V_b = 0.2-0.4$ V. This reversal of the ratio $G_{\text{CuO}_2}(V_1)/G_{\text{BiO}}(V_1)$ is not self-evident, and the important feature which should be explained.

As discussed in 4.3.2, if there is an insulating layer, whose band gap is not so large, covering a metal surface, this makes the barrier lower (the edge energy of the unoccupied conduction band corresponds to the barrier height in the region of this insulating layer) and the decay of the tunneling current as a function of the barrier width more gently-sloping than the exponential one which is expected on a non-degraded metal surface (Fig. 4.13). This deviation from the exponential decay cannot be explained if the insulating layer simply decreased the barrier height. It is likely that the insulating layer change the average barrier height depending on the barrier thickness. Now we propose a possible explanation for the behavior of the barrier width dependence of tunneling spectrum on the BiO terminated surface of BSCCO considering all these factors.

What we will discuss is a 1D system which is assumed in the semi-phenomenological theory of tunneling introduced by Giaever and Megerle [Ref. 97] discussed in section 2.1.2. We assume that the CuO_2 layer is superconducting, the surface BiO layer is semiconducting and the STM tip is normal metallic, respectively [Figs. 4.31(a), 4.31(b)]. The CuO_2 layer and the BiO layer have energy dependent density of states [$N_1(E)$ and $N_2(E)$, respectively] and the probe tip has energy independent one [$N_3(E) = N_3 = \text{const.}$]. To simplify the system, we intentionally ignore the tunneling process between the SrO layer and the tip, and assume that the SrO layer is semiconducting whose band gap energy is comparable to that of the BiO layer.

If we could detect the tunneling conductance between the BiO layer and the tip and that between the CuO_2 layer and the tip separately, they are thought to be expressed as following equations, by the analogy with Eq. 2.24.

$$\text{BiO} \leftrightarrow \text{Tip} : \quad \left(\frac{dI_{21}}{dV} \right)_{T=0} = G_{21}(V) = A_{21} N_2(V) N_3 \quad (4.13)$$

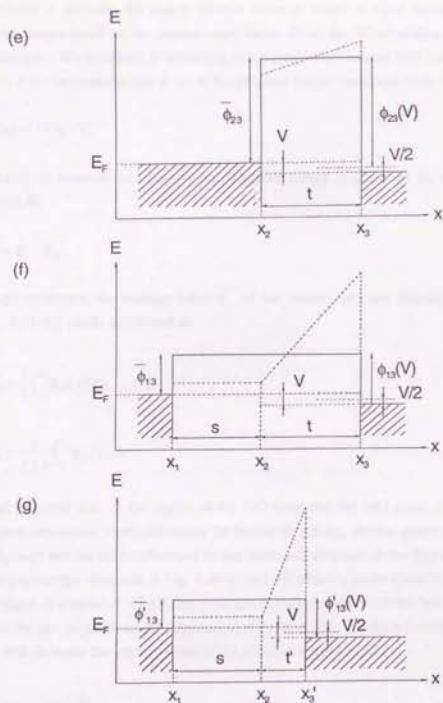


Fig. 4.31 Schematic diagrams of the composite barriers formed by vacuum and the surface semiconducting BiO layer. Average height of the barrier is varied by changing the thickness of vacuum.

$$\text{CuO}_2 \leftrightarrow \text{Tip} : \left(\frac{dI_{13}}{dV} \right)_{V=0} = G_{13}(V) = A_{13} N_1(V) N_3 \quad (4.14)$$

The prefactor A includes the matrix element between states of equal energy in both sides, and should be proportional to the transmission factor D of the Wentzel-Kramers-Brillouin (WKB) approximation. We introduce D according to the result after Sommerfeld and Bethe [Ref. 98]. In doing so, it is convenient to use $\phi(x)$ as the potential barrier measured from the Fermi energy (E_F),

$$\phi(x) = U(x) - E_F \quad (4.15)$$

and similarly to measure the x component of kinetic energy in excess of E_F , which is expressed by the symbol W .

$$W = E_x - E_F \quad (4.16)$$

For rough estimates, the average value $\overline{\phi}$ of the barrier for each tunneling process [see Figs. 4.31(c), 4.31(d)] can be expressed as

$$\overline{\phi}_{23} = \frac{1}{t} \int_{x_1}^{x_2} \phi_{23}(x) dx \quad (4.17)$$

$$\overline{\phi}_{13} = \frac{1}{s+t} \int_{x_1}^{x_2} \phi_{13}(x) dx \quad (4.18)$$

It should be noted that, in the region of the SrO layer and the BiO layer, the edge energy of the unoccupied conduction band determines the barrier height ϕ_1 , and the shape of the barrier between the CuO_2 layer and the tip is influenced by the electronic structure of the SrO and BiO layers. Since the band gap energy observed in Fig. 4.20 is -0.1 eV which is much lower than the typical vacuum barrier height of a metal of ~ 5 eV, the presence of these layers lower the barrier between the CuO_2 layer and the tip. In addition, the application of positive bias V , which lowers the right-hand Fermi energy, will decrease the average value of the potential barrier by $W/2$,

$$\phi_{23}(V) = \overline{\phi}_{23} - \frac{V}{2} \quad (4.19)$$

$$\phi_{13}(V) = \overline{\phi}_{13} - \frac{V}{2} \quad (4.20)$$

Using these results, transmission factors for each process become

$$D_{23} = \exp \left\{ -2 \sqrt{\frac{2m}{\hbar^2}} t [\phi_{23}(V) - W]^{1/2} \right\} \quad (4.21)$$

$$D_{13} = \exp \left\{ -2 \sqrt{\frac{2m}{\hbar^2}} (s+t) [\phi_{13}(V) - W]^{1/2} \right\} \quad (4.22)$$

The region of current interest is vicinity of the E_p , so that we fix $E_p = E_p(W=0)$ for simplicity. In the process of obtaining Eq. 2.24, we assumed that the prefactor A is independent of energy in the region we discussed. Therefore, the transmission factor D in the present case should be energy independent, too. In actual experiments, the observing energy region was $|W| < 0.5$ eV, hence $|W| \ll \bar{\phi}$ and the influence of the term $-W/2$ in Eqs. 4.19 and 4.20 is not so large. Here, we ignore this term $-W/2$, too, which is thought not to change the intrinsic part of this discussion. Finally we obtain

$$D_{23} = \exp \left[-2 \sqrt{\frac{2m}{\hbar^2}} t \bar{\phi}_{23}^{-1/2} \right] \quad (4.23)$$

$$D_{13} = \exp \left[-2 \sqrt{\frac{2m}{\hbar^2}} (s+t) \bar{\phi}_{13}^{-1/2} \right] \quad (4.24)$$

for the tunneling process between the BiO layer and the tip and that between the CuO_2 layer and the tip, respectively. These can be reduced very easily to the forms as follows:

$$D_{23} = \exp \left[-2 \sqrt{\frac{2m}{\hbar^2}} t \sqrt{\frac{\phi_2 + \phi_1}{2}} \right] \quad (4.25)$$

$$D_{13} = \exp \left[-2 \sqrt{\frac{2m}{\hbar^2}} (s+t) \sqrt{\frac{\phi_1 s + (\phi_1 + \phi_2) t / 2}{s+t}} \right] \quad (4.26)$$

Since $A_{23} \propto D_{23}$ and $A_{13} \propto D_{13}$,

$$\frac{G_{\text{CuO}_2}(V)}{G_{\text{BiO}}(V)} = \frac{G_{13}(V)}{G_{23}(V)} = \frac{D_{13} N_1(V)}{D_{23} N_2(V)} \quad (4.27)$$

The energy level of V_1 ($= 0.1$ eV in Fig. 4.20) corresponds to near the band gap edge of the BiO band, and to the middle of the CuO_2 band. Therefore the density of states of the CuO_2 layer at this

energy $N_1(V_i)$ is considered to be much larger than that of the surface BiO layer $N_2(V_i)$ [Fig. 4.31(b)].

$$N_1(V_i) \gg N_2(V_i) \quad (4.28)$$

The average barrier height of the tunneling process between the CuO_2 layer and the tip ($\bar{\phi}_{13}$) is lower than that between the BiO layer and the tip ($\bar{\phi}_{23}$) because the SrO and BiO layers play a role of a low barrier which lowers the average barrier height $\bar{\phi}$ [see Figs. 4.31(e), 4.31(f)].

$$\bar{\phi}_{13} < \bar{\phi}_{23} \quad (4.29)$$

If the tip-sample separation t becomes small, this effect becomes remarkable [Fig. 4.31(g)].

$$\bar{\phi}_{13} \ll \bar{\phi}_{23} \quad (t \rightarrow 0) \quad (4.30)$$

Therefore the ratio of transmission factors D_1/D_{23} becomes larger as t becomes small, which is thought to be the origin of the reversing behavior of the ratio $G_{\text{CuO}_2}(V_i)/G_{\text{BiO}}(V_i)$ and cause the deviation from the exponential decay. Actually, we assumed appropriate values for the parameters in the equations, and calculated this conductance ratio as a function of the tip-sample separation. Fig. 4.32(b) demonstrates this calculation result revealing the same tendency as observed.

4.7 Conclusions

We have performed atomic resolution STM/STS observations on BSCCO single crystals to investigate topographic features and electronic structures. The measurements have been done on the cleaved surfaces and the cross-sectional surfaces of the BSCCO crystals annealed in various atmospheres, and the cleaved surfaces of Pb doped BSCCO crystals, mainly at 4.2 K.

The results obtained on the cleaved planes of BSCCO under the same experimental condition showed two different features depending on the measurements. In one case, STM imaging revealed the atomic arrangement with a modulation structure in one direction which corresponds to the square lattice of Bi atoms, indicating the BiO termination of the specimen. The tunneling spectra showed essentially a semiconducting feature even below the T_c . The band gap energy changed depending on the annealing condition of the sample in the manner that the band gap became small as the oxygen content increased, suggesting that the electronic structure of the BiO layer becomes less insulative with a large hole concentration. The spectrum varied its shape depending on the barrier width, and a superconducting gap appeared in the band gap region with a small tip-sample separation. This behavior can be explained if we assume that the spectrum consists of two components originating from the surface BiO layer and the underlying CuO_2 layer, and the surface BiO layer and the adjacent SrO layer play a role to lower the average barrier height in the tunneling

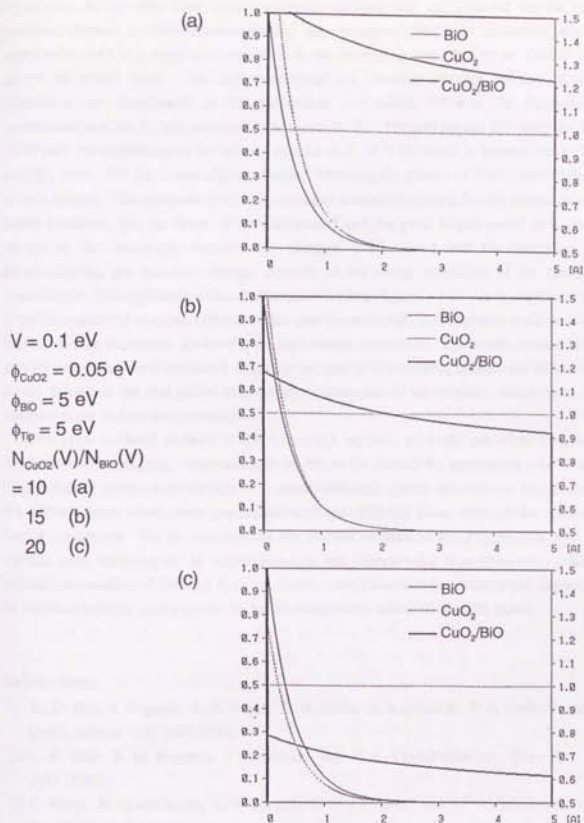


Fig. 4.32 Calculation results based on Eqs. 4.25-4.27 assuming appropriate parameters.

process between the CuO_2 layer and the probe tip, whose effect depends on the tip-sample separation. In the other case, atomic resolution imaging was not achieved but the tunneling spectrum showed a clear superconducting gap structure, which is understandable if the superconducting CuO_2 layer was covered with the terminating layer having no density of states around the Fermi level. The superconducting gap structure showed ordinary temperature dependence and disappeared as the temperature was raised, however the decrease of the conductance near the E_F still remained even above the T_c . The gap energy 2Δ took the value of 70-90 meV corresponding to the reduced gap $2\Delta/k_B T_c$ of 9-12 which is beyond the BCS weak coupling limit. The 2Δ value slightly changed following the change of the T_c depending on the oxygen content. The spectrum essentially indicated a superconducting feature independent of the barrier thickness, but the shape of the background and the peak height varied in a systematic manner as the tip-sample distance was changed. We found that the sharpness of the superconducting gap structure strongly depends on the energy resolution of the spectroscopic measurement. Although most of the spectra showed smeared gaps which can be explained in terms of both intrinsic and extrinsic effects, a finite gap structure with low zero-bias conductance and a flat bottom was sometimes observed with high energy resolution. This result obtained by STM strongly suggests *s*-wave symmetry of the Cooper pair of this system, because the STM tunneling is very limited in the real space, thus covers a wide area in the *k*-space, which rules out the existence of the node in the symmetry.

On the cross-sectional surfaces of BSCCO single crystals, we could not achieve reproducible atomic resolution imaging, which seems to be due to the lack of the appropriate way to obtain a clean surface of atomic-scale flatness. The superconducting spectra observed can be classified into two different types which show gap structures of two different sizes, although the reason is not clear at the present. On the contrary, on the cleaved surfaces of $\text{Bi}_{1-x}\text{Pb}_x\text{Sr}_{1-x}\text{CaCu}_2\text{O}_y$ single crystals, wide scattering of the superconducting gap energy value was observed. This result indicates the variation of the local T_c in the crystal, which seems to be owing to the degradation of the superconductivity locally caused by the inhomogeneous substitution of Pb atoms.

References

- [1] M. D. Kirk, J. Nogami, A. A. Baski, D. B. Mitzi, A. Kapitulnik, T. H. Geballe, and C. F. Quate, *Science* 242, 1673 (1988).
- [2] C. K. Shih, R. M. Feenstra, J. R. Kirtley, and G. V. Chandrashekar, *Phys. Rev. B* 40, 2682 (1989).
- [3] C. Wang, B. Giambattista, C. G. Slough, R. V. Coleman, and M. A. Subramanian, *Phys. Rev. B* 42, 8890 (1990).
- [4] X. L. Wu, Z. Zhang, Y. Wang, and C. M. Lieber, *Science* 248, 1211 (1990).
- [5] Y. Gao, P. Lee, P. Coppens, M. A. Subramanian, and A. W. Sleight, *Science* 241, 954 (1988).

- [6] M. Tanaka, T. Takahashi, H. Katayama-Yoshida, S. Yamazaki, M. Fujinami, Y. Okabe, W. Mizutani, M. Ono, and K. Kajimura, *Nature* 339, 691 (1989).
- [7] T. Hasegawa, and K. Kitazawa, *Jpn. J. Appl. Phys.* 29, L434 (1990).
- [8] S. Massidda, J. Yu, and A. J. Freeman, *Physica C* 152, 251 (1988).
- [9] M. S. Hybertsen, and L. F. Mattheiss, *Phys. Rev. Lett.* 60, 1661 (1988).
- [10] H. Krakauer, and W. E. Pickett, *Phys. Rev. Lett.* 60, 1665 (1988).
- [11] T. Takahashi, H. Matsuyama, H. Katayama-Yoshida, Y. Okabe, S. Hosoya, K. Seki, H. Fujimoto, M. Sato, and H. Inokuchi, *Nature* 334, 691 (1988).
- [12] C. G. Olson, R. Liu, A.-B. Yang, D. W. Lynch, A. J. Arko, R. S. List, D. W. Veal, Y. C. Chang, P. Z. Jiang, and A. P. Paulikas, *Science* 245, 731 (1989).
- [13] C. G. Olson, R. Liu, D. W. Lynch, R. S. List, A. J. Arko, D. W. Veal, Y. C. Chang, P. Z. Jiang, and A. P. Paulikas, *Solid State Commun.* 76, 411 (1990).
- [14] C. G. Olson, R. Liu, D. W. Lynch, R. S. List, A. J. Arko, D. W. Veal, Y. C. Chang, P. Z. Jiang, and A. P. Paulikas, *Phys. Rev. B* 42, 381 (1990).
- [15] R. Manzke, T. Buslaps, R. Claessen, and J. Fink, *Europhys. Lett.* 9, 477 (1989).
- [16] J.-M. Imer, F. Patthey, B. Dardel, W.-D. Schneider, Y. Baer, Y. Petroff, and A. Zettl, *Phys. Rev. Lett.* 62, 336 (1989).
- [17] Y. Chang, M. Tang, R. Zanon, M. Onellion, R. Joynt, D. L. Huber, G. Margaritondo, P. A. Morris, W. A. Bonner, J. M. Tarascon, and N. G. Stoffel, *Phys. Rev. B* 39, 4740 (1989).
- [18] B. O. Wells, Z.-X. Shen, D. S. Dessau, W. E. Spicer, C. G. Olson, D. B. Mitzi, A. Kapitulnik, R. S. List, and A. Arko, *Phys. Rev. Lett.* 65, 3056 (1990).
- [19] D. S. Dessau, B. O. Wells, Z.-X. Shen, W. E. Spicer, A. J. Arko, R. S. List, D. B. Mitzi, and A. Kapitulnik, *Phys. Rev. Lett.* 66, 2160 (1991).
- [20] Y. Hwu, L. Lozzi, M. Marsi, S. La Rosa, M. Winokur, P. Davis, M. Onellion, H. Berger, F. Gozzo, F. Lévy, and G. Margaritondo, *Phys. Rev. Lett.* 67, 2573 (1991).
- [21] D. S. Dessau, Z.-X. Shen, B. O. Wells, D. M. King, W. E. Spicer, A. J. Arko, L. W. Lombardo, D. B. Mitzi, and A. Kapitulnik, *Phys. Rev. B* 45, 5095 (1992).
- [22] R. J. Kelley, J. Ma, G. Margaritondo, M. Onellion, *Phys. Rev. Lett.* 71, 4051 (1993).
- [23] B. O. Wells, Z.-X. Shen, D. S. Dessau, W. E. Spicer, D. B. Mitzi, L. Lombardo, A. Kapitulnik, and A. J. Arko, *Phys. Rev. B* 46, 11830 (1992).
- [24] Z.-X. Shen, D. S. Dessau, B. O. Wells, D. M. King, W. E. Spicer, A. J. Arko, D. Marshall, L. W. Lombardo, A. Kapitulnik, P. Dickinson, S. Doniach, J. DiCarlo, A. G. Loeser, and C.-H. Park, *Phys. Rev. Lett.* 70, 1553 (1993).
- [25] D. S. Dessau, Z.-X. Shen, D. M. King, D. S. Marshall, L. W. Lombardo, P. H. Dickinson, A. G. Loeser, J. DiCarlo, C.-H. Park, A. Kapitulnik, and W. E. Spicer, *Phys. Rev. Lett.* 71, 2781 (1993).
- [26] J. Ma, C. Quitmann, R. J. Kelley, H. Berger, G. Margaritondo, and M. Onellion, submitted to *Phys. Rev. Lett.*
- [27] H. Ding, J. C. Campuzano, A. F. Bellman, T. Yokoya, M. R. Norman, M. Randeria, T.

- Takahashi, H. Katayama-Yoshida, T. Mochiku, K. Kadowaki, and G. Jennings, submitted to *Phys. Rev. Lett.*
- [28] W. L. McMillan, and J. M. Rowell, *Phys. Rev. Lett.* 14, 108 (1965).
- [29] G. B. Arnold, F. M. Mueller, and J. C. Swihart, *Phys. Rev. Lett.* 67, 2569 (1991).
- [30] P. W. Anderson, *Phys. Rev. Lett.* 67, 660 (1991).
- [31] P. Hedergård, and M. B. Pedersen, *Phys. Rev. B* 43, 11504 (1991).
- [32] C. M. Varma, P. B. Littlewood, S. Schmitt-Rink, E. Abrahams, and A. E. Ruckenstein, *Phys. Rev. Lett.* 63, 1996 (1989).
- [33] P. B. Littlewood, and C. M. Varma, to be published.
- [34] D. J. Scalapino, E. Loh, Jr., and J. E. Hirsch, *Phys. Rev. B* 34, 8190 (1986).
- [35] N. E. Bickers, *Int. J. Mod. Phys. B* 1, 687 (1987).
- [36] N. E. Bickers, D. J. Scalapino, and S. R. White, *Phys. Rev. Lett.* 62, 961 (1989).
- [37] A. E. Ruckenstein, P. J. Hirschfeld, and J. Appel, *Phys. Rev. B* 36, 857 (1987).
- [38] G. Kotliar, and J. Liu, *Phys. Rev. B* 38, 5142 (1988).
- [39] J. R. Schrieffer, X.-G. Wen, and S.-C. Zhang, *Phys. Rev. Lett.* 60, 944 (1988).
- [40] M. Inui, S. Doniach, P. J. Hirschfeld, and A. E. Ruckenstein, *Phys. Rev. B* 37, 2320 (1988).
- [41] G. J. Chen, R. Joynt, and F. C. Zhang, *Phys. Rev. B* 42, 2662 (1990).
- [42] P. Monthoux, A. V. Balatsky, and D. Pines, *Phys. Rev. Lett.* 67, 3448 (1991).
- [43] P. Monthoux, and D. Pines, *Phys. Rev. Lett.* 69, 961 (1992).
- [44] N. Bulut, and D. J. Scalapino, *Phys. Rev. Lett.* 68, 706 (1992).
- [45] G. Kotliar, *Phys. Rev. B* 37, 3664 (1988).
- [46] T. Hasegawa, M. Nantoh, H. Suzuki, N. Motohira, K. Kishio, and K. Kitazawa, *Physica B* 165&166, 1563 (1990).
- [47] C. Wang, B. Giambattista, C. G. Slough, and R. V. Coleman, *Phys. Rev. B* 42, 8890 (1990).
- [48] J.-X. Liu, J.-C. Wan, and A. M. Goldman, *Phys. Rev. Lett.* 67, 2195 (1991).
- [49] C. Renner, Ø. Fischer, A. D. Kent, D. B. Mitzi, and A. Kapitulnik, *Physica B* 194-196, 1689 (1994).
- [50] E. J. G. Boom, A. J. A. van Roy, and H. van Kempen, to be published in *Physica C*.
- [51] C. Manabe, M. Oda, and M. Ido, to be published in *Physica C*.
- [52] H. Murakami, and R. Aoki, submitted to *J. Phys. Soc. Jpn.*
- [53] F. Izumi, *Oyo Buturi* 59, 2 (1990).
- [54] C. K. Shih, R. M. Feenstra, and G. V. Chandrasekhar, *Phys. Rev. B* 43, 7913 (1991).
- [55] J. R. Kirtley, R. T. Collins, Z. Schlesinger, W. J. Gallagher, R. L. Sandstrom, T. R. Dinger, and D. A. Chance, *Phys. Rev. B* 35, 8846 (1987).
- [56] M. C. Gallagher, J. G. Adler, J. Jung, and J. P. Franck, *Phys. Rev. B* 37, 7846 (1988).
- [57] A. P. Fein, J. R. Kirtley, and M. W. Shafer, *Phys. Rev. B* 37, 9738 (1988).
- [58] S. Vieira, M. A. Ramos, M. Vallet-Regi, and J. M. Gonzalez-Calbet, *Phys. Rev. B* 38, 9295

- (1988).
- [59] J. R. Kirtley, R. M. Feenstra, A. P. Fein, S. I. Raider, W. J. Gallagher, R. Sandstrom, T. Dinger, M. W. Shafer, R. Koch, R. Laibowitz, and B. Bumble, *J. Vac. Sci. Technol. A* 6, 259 (1988).
- [60] M. C. Gallagher, and J. G. Adler, *J. Vac. Sci. Technol. A* 8, 464 (1990).
- [61] R. Wilkins, M. Amman, R. E. Soltis, E. Ben-Jacob, R. C. Jaklevic, *Phys. Rev. B* 41, 8904 (1990).
- [62] T. G. Miller, M. McElfresh, and R. Reifenberger, *Phys. Rev. B* 48, 7499 (1993).
- [63] T. Ekino, and J. Akimitsu, *Phys. Rev. B* 40, 7364 (1989).
- [64] Q. Huang, J. F. Zasadzinski, K. E. Gray, J. Z. Liu, and H. Claus, *Phys. Rev. B* 40, 9366 (1989).
- [65] K. Ichimura, and K. Nomura, *J. Phys. Soc. Jpn.* 62, 3661 (1993).
- [66] H. Fukuyama, Y. Hasegawa, and Y. Suzumura, *Physica C* 153-155, 1630 (1988).
- [67] Y. Suzumura, Y. Hasegawa, and H. Fukuyama, *J. Phys. Soc. Jpn.* 57, 401 (1988).
- [68] Y. Suzumura, Y. Hasegawa, and H. Fukuyama, *J. Phys. Soc. Jpn.* 57, 2768 (1988).
- [69] H. Yasuoka, T. Imai, and T. Shimizu, *Strong Correlation and Superconductivity*, edited by H. Fukuyama, S. Maekawa, and A. P. Malozemoff, Springer Verlag, Berlin, 254 (1989).
- [70] Y. Kitaoka, K. Ishida, S. Ohsugi, K. Fujiwara, and K. Asayama, *Physica C* 185-189, 98 (1991).
- [71] M. Takigawa, P. C. Hammel, R. H. Heffner, and Z. Fink, *Phys. Rev. B* 39, 7371 (1989).
- [72] M. Takigawa, A. P. Reyes, P. C. Hammel, J. D. Thompson, R. H. Heffner, Z. Fink, and K. C. Ott, *Phys. Rev. B* 43, 247 (1991).
- [73] M. Takigawa, *J. Phys. Chem. Solids* 53, 1651 (1992).
- [74] Q. Huang, J. F. Zasadzinski, K. E. Gray, E. D. Bukowski, and D. M. Ginsberg, *Physica C* 161, 141 (1989).
- [75] T. Matsumoto, T. Kawai, K. Kitahama, and S. Kawai, unpublished.
- [76] E. L. Wolf, *Principles of Electron Tunneling Spectroscopy*, Oxford University Press, New York, 36 (1985).
- [77] J. Halbritter, *Phys. Rev. B* 46, 14861 (1992).
- [78] G. E. Blonder, M. Tinkham, and T. M. Klapwijk, *Phys. Rev. B* 25, 4515 (1982).
- [79] G. E. Blonder, and M. Tinkham, *Phys. Rev. B* 27, 112 (1983).
- [80] S. H. Liu, and R. A. Klemm, *Phys. Rev. Lett.* 73, 1019 (1994).
- [81] M. Gurvitch, J. M. Valles, Jr., A. M. Cucolo, R. C. Dynes, J. P. Garno, L. F. Schneemeyer, and J. V. Waszczak, *Phys. Rev. Lett.* 63, 1008 (1989).
- [82] K. Kuroda, K. Kojima, O. Wada, M. Tanioku, K. Yokoyama, and K. Hamanaka, *Jpn. J. Appl. Phys.* 29, L1816 (1990).
- [83] S. A. Sunshine, T. Siegrist, L. F. Schneemeyer, D. W. Murphy, R. J. Cava, B. Batlogg, R. B. van Dover, R. M. Fleming, S. H. Glarum, S. Nakahara, R. Farrow, J. J. Krajewski, S. M. Zahurak, J. V. Waszczak, J. H. Marshall, P. Marsh, L. W. Rupp, Jr., and W. F. Peck,

- Phys. Rev. B 38, 893 (1988).
- [84] R. Ramesh, G. Thomas, S. Green, C. Jiang, Y. Mei, M. L. Rudee, and H. L. Luo, Phys. Rev. B 38, 7070 (1988).
- [85] C. H. Chen, D. J. Werder, G. P. Espinosa, and S. A. Cooper, Phys. Rev. B 39, 4686 (1989).
- [86] P. Bordet, J. J. Capponi, C. Chaillout, J. Chenavas, A. W. Hewat, E. A. Hewat, J. L. Hodeau, and M. Marezio, Stud. High Temp. Supercond. 2, 171 (1989).
- [87] J. Schneck, L. Pierre, J. C. Toledano, and C. Daguet, Phys. Rev. B 39, 9624 (1989).
- [88] S. X. Dou, H. K. Liu, A. J. Bourdillon, M. Kviz, N. X. Tan, and C. C. Sorrell, Phys. Rev. B 40, 5266 (1989).
- [89] R. Ramesh, M. S. Hegde, C. C. Chang, J. M. Tarascon, S. M. Green, and H. L. Luo, J. Appl. Phys. 66, 4878 (1989).
- [90] H. Nobumasa, T. Arima, K. Shimizu, Y. Otsuka, Y. Murata, and T. Kawai, Jpn. J. Appl. Phys. 28, L57 (1989).
- [91] Z. Zhang, Y. L. Wang, X. Li. Wu, J. -L. Huang, and C. M. Lieber, Phys. Rev. B 42, 1082 (1990).
- [92] R. C. Dynes, V. Narayanamurti, and J. P. Garno, Phys. Rev. Lett. 41, 1509 (1978).
- [93] R. C. Dynes, J. P. Garno, G. B. Hertel, and T. P. Orlando, Phys. Rev. Lett. 53, 2437 (1984).
- [94] J. Bardeen, L. N. Cooper, and J. R. Schrieffer, Phys. Rev. 108, 1175 (1957).
- [95] T. Schneider, H. De Raedt, and M. Frick, Z. Phys. B 76, 3 (1989).
- [96] J. R. Kirtley, Phys. Rev. B 41, 7201 (1990).
- [97] I. Giaever, and K. Megerle, Phys. Rev. 122, 1101 (1961).
- [98] A. Sommerfeld, and H. Bethe, *Handbuch der Physik Vol. 24/2*, edited by S. Flügge, Springer-Verlag, Berlin, 450 (1933).

Chapter 5

Observations on YBCO Thin Films

5.1 Introduction

Although there are a lot of successful works on BSCCO single crystals as discussed in Chapter 4, neither an atomic resolution STM image nor the tunneling spectrum showing a clear superconducting gap has been reported on the surfaces of bulk YBCO materials at cryogenic temperature so far [Refs. 1-3] except a recent work in UHV by Edwards *et al.* [Refs. 4, 5]. They observed YBCO single crystals which were cleaved *in situ* at 20 K prior to measurements, and obtained atomic images corresponding to the CuO chain layer and observed tunneling spectra with broad superconducting gap structures of $2\Delta/k_B T_c = 6-8$ [Ref. 4]. Recently, they also identified corrugations in the electron density along the CuO chains with a periodicity of several lattice constants, which they considered to be due to a CDW state. The STM observation on a bulk YBCO surface in air seems to be limited because the surface of this system is chemically reactive and tends to be degraded by H₂O or CO₂ contained in an ambient atmosphere [Refs. 6, 7]. Furthermore, there is no stable cleavable plane in YBCO unlike in BSCCO, so that the rearrangement of atoms may take place even on a clean surface. In fact, Edwards *et al.* reported that atomic resolution STM images could be obtained only when the cleavage and the measurement were done at $T < 60$ K [Ref. 4]. On the other hand, spiral growth patterns were clearly observed on *c*-axis oriented YBCO epitaxial films at room temperature even in air [Refs. 8-12]. Lang *et al.* have reported on the imaging of two kinds of rectangular atomic lattices with lattice spacing of 2.7 Å and 3.8 Å, which were assigned to the oxygen atom arrangement of the CuO₂ layer and other atomic arrangements, respectively, on *c*-axis oriented laser-deposited films under such conditions. These results suggest that the surfaces of YBCO epitaxial films are atomically flat and more stable in ambient gas than those of the bulk specimens. However, at cryogenic temperature, atomic resolution STM/STS had not been successful on YBCO films before the present study in spite of many attempts [Refs. 13-15].

The LDA band-structure calculations [Refs. 16-18] revealed the presence of four bands crossing the E_F [Fig. 5.1(a)]. Two strongly dispersed CuO₂ bands consist of $\text{Cu}3d_{x^2-y^2}-\text{O}2p_{x,y}$ combinations and have a 2D character [(2) and (3) in Fig. 5.1]. Two CuO bands are in sharp contrast [(1) and (4) in Fig. 5.1]. The $\text{Cu}3d_{x^2-y^2}-\text{O}2p_{z,y}$ anti-bonding band shows the large 1D dispersion expected from the CuO linear chains but is almost entirely unoccupied. Possible nesting features can be observed for this 1D structure. On the contrary, the π -bonding band formed from the $\text{Cu}3d_{xy}-\text{O}2p_{x,y}$ orbitals is almost entirely occupied and form two additional hole pockets around

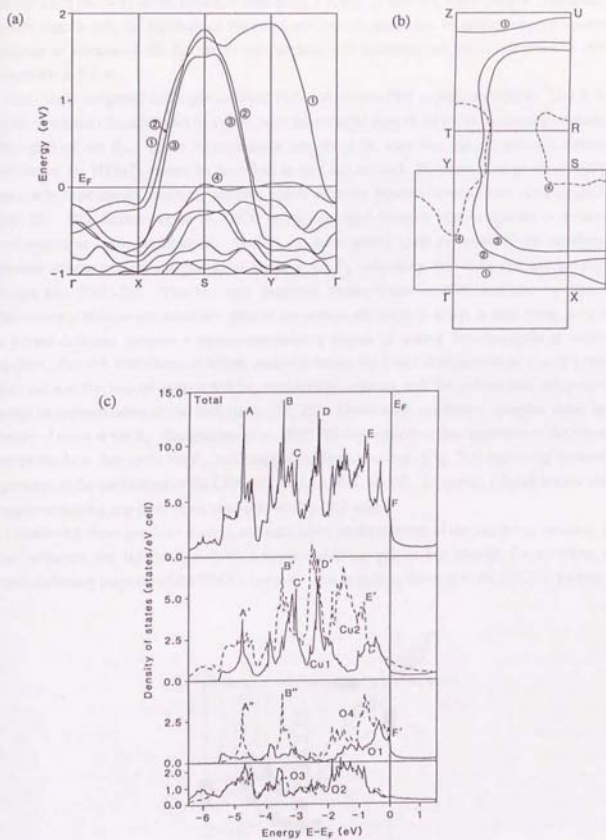


Fig. 5.1 Results of LDA band structure calculation by Massidda *et al.* [Ref. 16]. (a) Energy bands of YBCO near the E_F on an enlarged scale. (b) Fermi surface of YBCO. (c) Total and projected DOS for the valence bands.

the $Y(T)$ and the $S(R)$ in the Brillouin zone [Fig. 5.1(b)]. Therefore, extra oxygen vacancies can modify significantly the topology of the Fermi surface. In particular, by adding oxygen vacancies resulting in increase of the E_F , the π hole pockets will disappear and the 1D structure is shifted toward the S - Y line.

Early angle-integrated and angle-resolved PES and inverse-PES experiments [Refs. 19-27] have shown spectrum characteristics of oxides, with pronounced gaps of ~ 2 eV in the density of states in the region of the E_F . These measurements reinforced the idea that the ground-state electronic structure of the HTSC's cannot be described by an LDA method. However, List *et al.* shown that these early experiments measured samples which were not representative of bulk superconductors [Ref. 28]. The surface region of YBCO undergoes rapid changes when subjected to a vacuum environment at room temperature. Veal *et al.* have shown clear evidence of the relationship between oxygen content and density of states at the E_F concluding that those changes are due to oxygen loss [Ref. 29]. This has very important consequences in PES, and also in tunneling spectroscopy, because the mean free path of low-energy electrons in solids is very short, such that in oxygen-deficient samples a nonsuperconducting region of only a few unit cells in depth is sampled. But if a YBCO crystal is first cooled to below 40 K and then cleaved *in situ* to reveal a fresh surface, the loss of oxygen will be considerably reduced, and the surface thus obtained will indeed be representative of the bulk [Refs. 28, 29]. Under such conditions, samples show large density of states at the E_F . Campuzano *et al.* [Ref. 30] have observed the dispersion of the electron energy bands as they cross the E_F , and mapped the Fermi surface [Fig. 5.2] indicating reasonable agreement to the predictions of the LDA calculations [Ref. 16-18]. However, reliable results about a superconducting gap have never been obtained by PES study.

Considering these previous studies, although some understanding of the electronic structure has been achieved, the information about a superconducting gap is not enough for revealing the superconducting property of the YBCO system. This is quite in contrast to the BSCCO system on

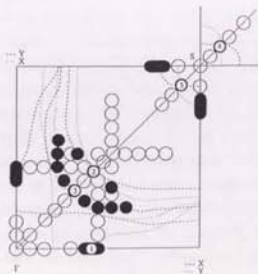


Fig. 5.2 Experimentally determined Fermi surface of YBCO. From [Ref. 30].

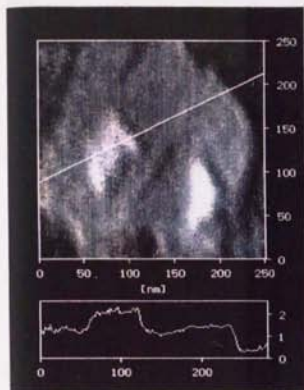
which ARPES experiments have measured the anisotropy of the superconducting energy gap (see Chapter 4). This delay of the study despite of the earlier discovery of YBCO seems to be due to its chemically unstable surface and lack of a stable cleavable plane of this system.

5.2 STM Observations on (001) Oriented YBCO Thin Films

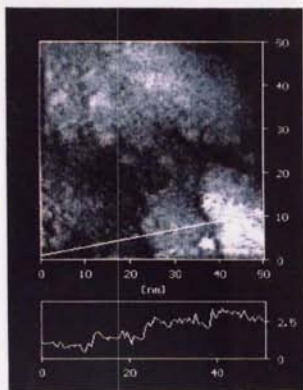
In our previous STM measurements, we had experienced that the surfaces of bulk single crystals of YBCO were covered with thick insulating layers with band gaps of more than 3 eV and hence did not allow atomic resolution STM observations even in a dry nitrogen atmosphere at room temperature unlike the case of BSCCO. However, the surfaces of YBCO epitaxial films employed in this work were much more stable than those of the bulk cleaved crystals and, to our surprise, the surfaces of these films remained in good conditions for tunneling measurements as well as for atomic imaging for more than 20 days after the film deposition.

Let us, at first, focus our attention on the semi-macro scale surface morphology. Figs. 5.3(a)-5.3(c) show STM images of the (001) surfaces of YBCO thin films taken at room temperature [Fig. 5.3(a)] and 4.2 K [Figs. 5.3(b) and 5.3(c)] with different scales of the scanning area. In Fig. 5.3(a), the terrace structure is observed, which seems to be formed by the two-dimensional nucleation and layer growth mechanism. This result is consistent with other STM observations on *c*-axis oriented YBCO thin films [Refs. 8-12]. In Fig. 5.3(b), step structures and flat terraces are observed in the lower half of the figure. The heights of these steps are 1.2 nm, corresponding to the *c*-spacing of the YBCO unit cell. These structures seem to be a part of the two-dimensional island structures as shown in Fig. 5.3(a). We found the presence of reproducible small structures of several nm in diameter on the terrace regions as shown in Fig. 5.3(c). The height of these structures was < 0.3 nm. These structures are presumably related with the spatial variation of the local density of states arising from the disorder of the surface oxygen atoms as suggested by Edwards *et al* [Ref. 4].

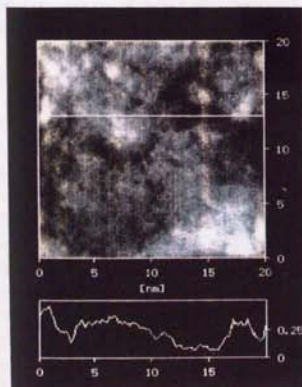
Figs. 5.4(a) and 5.4(b) show the STM images of the (001) plane of a YBCO thin film taken at 4.2 K. In these narrow scan images, one can clearly see the square atomic arrangements with the lattice spacing of ~ 4 Å corresponding to the *a*- or *b*-spacing. These features were observed reproducibly on subsequent images and did not vary in shape or orientation depending on the scanning frequency, so are real ones. These images suggest that the surfaces of the films were free from severe contamination or from chemical reaction. In Figs. 5.4(a) and 5.4(b), the crystalline axes are not at right angle to each other. This non-orthogonality, which was not always but often observed, is thought to be caused by some extrinsic effect. Creep of the piezoelectric rods of the scanner can cause this non-orthogonality. Another possibility is that the effective shape of the tip, which is determined by the atomic scale structure of the tip and the angle which the tip and the sample surface make, was not ideal one [Refs. 31-37]. Figs. 5.4(a) and 5.4(b) indicate distortion of the atomic lattice. Generally, in an STM measurement, this kind of distortion is often observed when the interaction between the tip and the sample is strong. On the other hand, disorder of the



(a)



(b)



(c)

Fig. 5.3 STM images of the (001) surfaces of laser-deposited YBCO thin films measured at (a) room temperature and (b)-(c) 4.2 K (constant current mode). (a) Island structures with steps and flat terraces. Image size 250×250 nm, tip bias voltage (V_b) -1900 mV, tunneling current (I_t) 2.5 nA. (b) Step structures with heights of about 1.2 nm corresponding to c -spacing of the YBCO unit cell. Image size 50×50 nm, V_b -1200 mV, I_t 0.3 nA. (c) Small structures with heights < 0.3 nm. Image size 20×20 nm, V_b -1200 mV, I_t 1.0 nA.

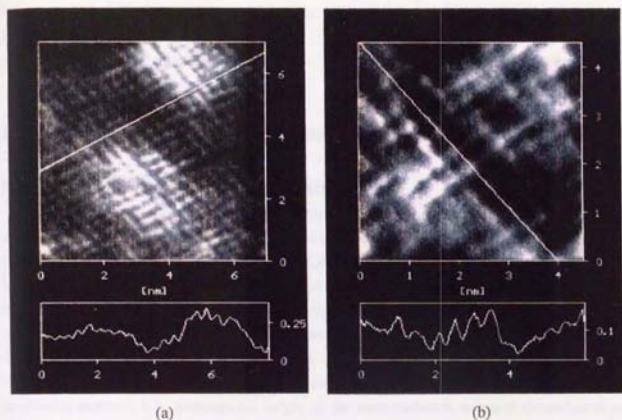


Fig. 5.4 STM images of the (001) surface of a laser-deposited YBCO thin film measured at 4.2 K (constant current mode). A square surface lattice with average spacing of 0.4 nm corresponds to the a - or b -spacing of the unit cell. Image size (a) 7×7 nm, (b) 4.5×4.5 nm, V_s (a), (b) -500 mV, and I_s (a) 50 pA, (b) 15 pA, respectively.

surface oxygen also may yield real distortion of the lattice.

Considering the crystallographic structure of YBCO, the atoms of all the sites except the O site of the CuO_2 plane can form the observed rectangular lattice with the spacing of $\sim 4 \text{ \AA}$. By the STM measurement itself, we cannot make clear which site appears in the STM images. Some models for the surface termination of a (001) oriented YBCO film are proposed by several groups adopting various experimental methods as will be discussed in section 5.6.2. Our atomic images shown in Figs. 5.4(a) and 5.4(b) seem to be similar to that observed by Lang *et al.* [Refs. 11, 12] which is a simple lattice, and quite different from those by Edwards *et al.* [Refs. 4, 5] which show complex structures. This difference must arise from the difference between the surface preparations, *i.e.*, as-grown surfaces and cleaved ones. In the case of the as-grown surface, the growth must end with the lowest surface energy which is actualized in a complete lattice. Hence the terminating layer must be close to the perfect lattice. On the contrary, if one cleaves a YBCO crystal, some of the atoms of the top layer remain and the other attach to the removed part because no stable cleavable plane exists in YBCO. Therefore the top layer has a great deal of missing atoms, which can no longer be called defects, and a complex structure appears. Such a surface must be very unstable. This must be the origin of the deference of stability between as-grown surfaces of thin films and

cleaved surfaces of single crystals as mentioned above. We did not observe any bias voltage dependence of the atomic image as reported by Lang *et al.* [Ref. 12], which may be due to the difference of the surface termination.

5.3 STS Measurements on (001) Oriented YBCO Thin Films

5.3.1 AST Measurement on Surface Layer

Fig. 5.5 shows the result of an AST measurement performed on the (001) oriented YBCO film surface, with Fig. 5.5(a) showing the 64 spots where the tunneling spectra were taken during the imaging. Tunneling spectra obtained at the locations marked by '+' do not show difference depending on the measuring locations, but demonstrate essentially the same feature with a band gap of about 0.1 eV, indicating that the surface layer is uniformly semiconductive. Fig. 5.5(b) superimposes the 16 tunneling spectra chosen among the 64 spectra at random. Same results were observed on the films irrespective of the periods of the exposure to air, and similar results were obtained on the cleaved surfaces of BSCCO single crystals which are chemically stable, as described in section 4.3.1. Although the origin of the semiconductive nature of the surface is not

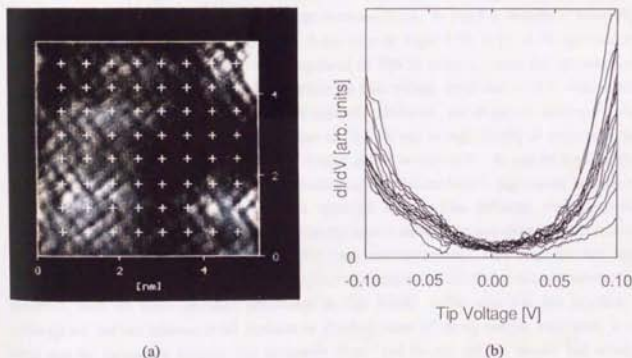


Fig. 5.5 STS observation of the (001) surface of a YBCO epitaxial film at 4.2 K. (a) Surface image taken in the STS mode. Image size 5.5×5.5 nm, locations of tunneling spectroscopic measurements 8×8 points (marked by '+'), $V_b = -500$ mV, $I_p = 0.2$ nA. (b) 16 tunneling spectra chosen at random showing a semiconductive nature with a band gap of 0.1 eV.

known at the present moment, it is clear that the state of the surface was completely different from that of degraded one which showed a much larger insulating gap and did not allow an STM observation. There is a possibility that non-superconducting layers originally exist in the unit cell, and the terminating layer is one of these layers. Another possible assumption is that only the surface electronic structure is different from that in the bulk material because only the surface layer is not sandwiched by other layers. In any case, it is thought that the semiconductive layer is confined just in the top-most surface region because the atomically resolved surface images could be obtained in Fig. 5.4(a) and 5.4(b), excluding the possibility of occurrence of severe surface degradation, and the superconducting gap structure was observed by decreasing the tip-sample distance as will be described below in the next section. Here, we would like to point out the fact that, at least, the top layer of atomic size thickness is semiconductive on the *c*-axis oriented YBCO film. Therefore, when one makes a tunneling junction by depositing an artificial barrier on the (001) surface of the YBCO film, the existence of this non-superconducting surface layer has to be taken into account considering the extremely short coherence length along the *c*-axis (ξ_c) of the HTSC [Ref. 38].

5.3.2 Barrier Width Dependence of Tunneling Spectrum

Fig. 5.6 shows the tunneling spectra measured with various tip bias voltages between -200 mV and -500 mV where set-point current I_p was kept constant, 2 nA. In Fig. 5.6, therefore, lower $|V|$ means the shorter tip-sample distance, which is the same as Figs. 4.20, 4.22, 4.24 appeared in Chapter 4. When we measured the cleaved surfaces of YBCO single crystals, the surfaces had band gaps more than 3 eV and we could not adjust the bias voltage lower than ~ 1.5 V without the collision between the STM tip and the sample surface. However, the as-grown surfaces of the films employed in this work had small band gaps of ~ 0.1 eV and enough density of states near the Fermi level, which enabled us to set the bias voltage as low as -200 mV. As can be seen, as the tip-sample distance was decreased, the conductance in the semiconductive gap region increased, and finally a superconducting gap structure appeared in it. This behavior was observed reproducibly when we changed the bias voltage in the same manner again and again, and the atomic image could be obtained just before and after these measurements. This indicates that any destruction had never occurred with both the tip and the sample surface during this measurement. However, with the same operating parameters as Fig. 5.6(d), stable scan was not possible. Although we did not measure work function or absolute value of the tip-sample separation, it is likely that the tip-sample distance was extremely short and the tip and the sample had strong interaction in Fig. 5.6(d). We found the same tendency, except the high conductance inside the superconducting gap (see section 5.6.3 about it) on the cleaved surfaces of BSCCO single crystals at 4.2 K as described in section 4.3.5. The fact that the tunneling spectrum taken on the (001) surface of the YBCO film changes its shape depending on the tip-sample distance in the same manner as BSCCO indicates that the superconducting CuO_2 layer lies under the surface

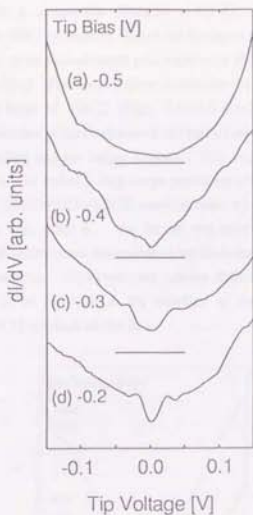


Fig. 5.6 Barrier width dependence of the tunneling spectrum on the (001) surface of a YBCO thin film at 4.2 K. V_p 's are (a) -500 mV, (b) -400 mV, (c) -300 mV, (d) -200 mV, respectively. $I_p = 2$ nA const. Zero conductance value is shown by the line under each spectrum.

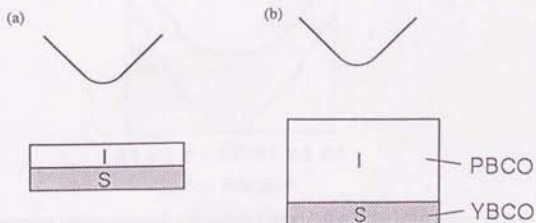


Fig. 5.7 Schematic diagrams of the tip and sample conditions for (a) Fig. 5.6 and (b) Fig. 5.8.

semiconducting layer with a comparable distance ($\sim 4.5 \text{ \AA}$). It is hence likely that the semiconductive layer on the YBCO surface is also of the thickness of atomic size [Fig. 5.7(a)].

Fig. 5.8 demonstrates the same measurement performed on a 50 \AA thick PBCO deposited YBCO (001) oriented film [Fig. 5.7(b)]. The spectra show essentially the same semiconducting feature as the surface semiconducting layer of YBCO [Figs. 5.6(a)-5.6(c)] irrespective of the tip-sample distance. This result indicates that if the thickness of the surface semiconducting layer is at least 50 \AA , the quasi-particle tunneling can no longer happen. This supports the legitimacy of our conclusion discussed above. So called a long-range proximity effect has been often observed on the SNS junctions of the YBCO/PBCO/YBCO configuration where the thickness of the PBCO layer is sometimes longer than 1000 \AA . As far as our experiments are concerned, such a phenomenon is unreal and it seems more reasonable to attribute such results to low quality barriers with pin holes of the junctions. However, we cannot definitively rule it out because this phenomenon is thought to be sensitive to the interface of the junction and we have never characterized the YBCO/PBCO interface of our film.

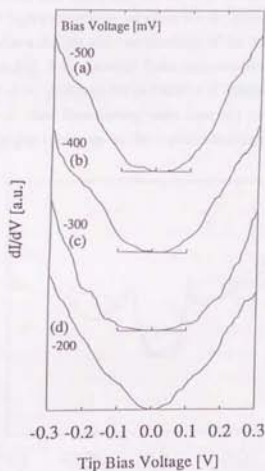


Fig. 5.8 Tunneling spectra measured with various barrier widths on the (001) surface of a 50 \AA PBCO deposited YBCO thin film at 4.2 K . V_b 's are (a) -500 mV , (b) -400 mV , (c) -300 mV , (d) -200 mV , respectively. $I_p = 2 \text{ nA}$ const. Zero conductance value is shown by the line under each spectrum.

5.3.3 Superconducting Energy Gap

Fig. 5.9 is one of the typical examples of tunneling spectra showing superconducting energy gap structure. The shape of the conductance curve in Fig. 5.9 is qualitatively close to the BCS function except for high zero-bias conductance in the gap relative to that in the normal-state region. As can be seen in Fig. 5.6, the width of the smaller gap in the U-shaped broad valley changes depending on the extent of the relative contribution from the surface non-superconducting layer. In order to avoid overestimating the energy gap, we adopted the spectra with two clear peaks on the sides of the gap as seen in Fig. 5.6(d) or Fig. 5.9. If we take the peak-to-peak separation in the conductance curve as the value of the superconducting energy gap, 2Δ is estimated to be ~ 40 meV, corresponding to the reduced gap value $2\Delta/k_B T_c \sim 5.2$. This value is smaller than that of the BSCCO 80 K phase ($2\Delta/k_B T_c \sim 9-12$) in spite of the higher T_c of ~ 90 K. This is consistent with previous works reporting the gap energies in the strong coupling regime by macroscopic junction methods [Refs. 39-41].

The tunneling spectrum in Fig. 5.9 indicates zero-bias conductance as high as 50% of the normal one. Most of the spectrum data measured on the YBCO films prepared under the condition described above showed high conductance values at $V = 0$. However, on some of the YBCO thin film samples prepared under a slightly different condition of the substrate temperature, we observed tunneling spectra given in Fig. 5.10 showing finite superconducting gap structure with very low zero-bias conductance of $\sim 1\%$. Although the probability of obtaining the conductance curve of this feature was very small, *i.e.*, three times among more than fifty measurements, this result seems to suggest that a finite energy gap opens up in the superconducting band, *i.e.*, s -wave symmetry of

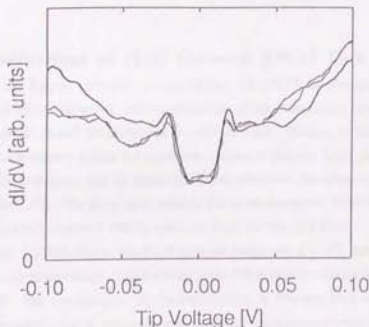


Fig. 5.9 Tunneling spectra measured on the (001) surface of a YBCO thin film showing a superconducting nature with an energy gap 2Δ of ~ 40 meV corresponding to a reduced gap value $2\Delta/k_B T_c \sim 5.2$ at 4.2 K. $V_b = -200$ mV, $I_p = 2$ nA.

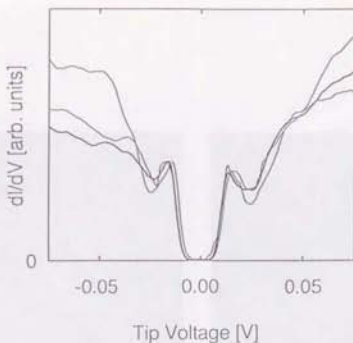


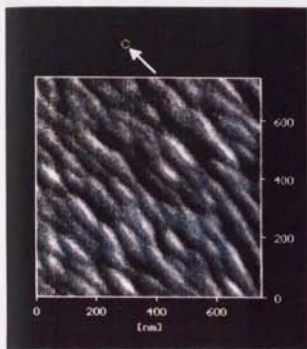
Fig. 5.10 Tunneling spectra measured on the (001) surface of a YBCO thin film showing a finite superconducting gap with a low zero-bias conductance value ($\sim 1\%$) at 4.2 K. $V_b = -100$ mV, $I_p = 4$ nA.

the Cooper pair. The difference between Fig. 5.9 and Fig. 5.10, *i.e.*, the extremely high zero-bias conductance, can be attributed to the difference of the termination of the films as will be discussed in section 5.6.3.

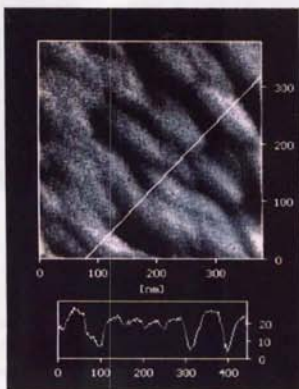
5.4 STM Observations on (110) Oriented YBCO Thin Films

As described in the former sections, we performed STM/STS observations on (001) oriented YBCO epitaxial thin films. However, the identification of the terminating layer of the YBCO (001) film is still controversial as will be discussed in section 5.6.2. Hence, tunneling spectrum data on the (001) films, which mainly reflect the electronic nature of the top layer, have ambiguity in their interpretations. This ambiguity can be excluded if one observes the cross-sectional surface of the layered structure [Ref. 42]. We have succeeded in the cross-sectional STM/STS observations with atomic resolution on (110) oriented YBCO epitaxial films for the first time.

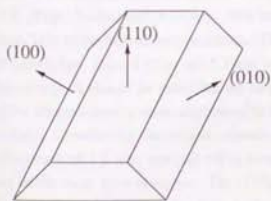
Figs. 5.11(a) and 5.11(b) show the STM images taken on a (110) oriented film with wide scanning areas at room temperature. Semi-macro scale hill structures which are elongated along the *c*-axis are observed. The average size of these structures is 150 nm long and 50 nm wide. The sectional diagram perpendicular to the *c*-axis schematically indicates the plateaus on the top of these structures [Fig. 5.11(b)]. The top flat planes and the other side facets are assigned from their angles as (110) and (100)/(010) planes, respectively [Fig. 5.11(c)]. Under a different growth condition, (110) oriented films with smoother surfaces were obtained. However, the surfaces of



(a)



(b)



(c)

Fig. 5.11 (a), (b) STM images of the surface of a (110) oriented YBCO thin film measured at room temperature. V_s 's and I_p 's are (a) -1.7 V, 8 nA, and (b) -1.7 V, 5 nA, respectively. (c) Schematic diagram of the observed hill structure.

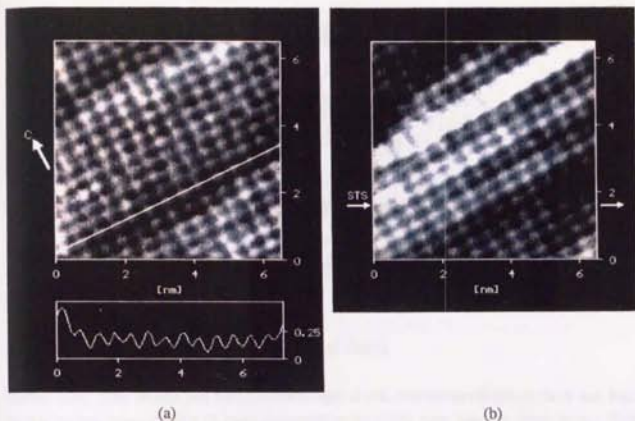


Fig. 5.12 Atomic resolution images obtained by scanning the same area of the (110) plane of a YBCO epitaxial film at 4.2 K. V_b 's and I_p 's are (a) -1.9 V, 0.13 nA, (b) -0.75 V, 0.09 nA, respectively. In Fig. 2(b), the arrows point at the scanning position of the STS measurement shown in Fig. 5.15.

such films were unstable and became insulating after exposure to the ambient atmosphere.

On the plateau region of the structure, *i.e.*, on the (110) plane, atomic images were obtained at 4.2 K [Figs. 5.12(a) and 5.12(b)]. The images clearly show an orthorhombic lattice of surface atoms. This is the first atomic resolution STM imaging on the (110) plane of YBCO to the best of our knowledge. Figs. 5.12(a) and 5.12(b) were taken with tip bias voltages of -1.9 V and -0.75 V, respectively. It should be noted that the relative difference in brightness between the duplex layer and the adjacent layer is more emphasized in the STM image taken with the lower bias voltage [Fig. 5.12(b)]. Considering the surface crystallographic structure of the YBCO (110) plane with the *c*-axis length of 1.2 nm, one unit cell is composed of three layers in the images, and two of them must be the same kind of layers. The (110) plane of YBCO can be uniquely defined, contrary to the (001) plane, as illustrated in Fig. 5.13. If the tunneling probability to Cu atoms of both the CuO_2 and CuO chain layers is higher, the orthorhombic lattice images as shown in Figs. 5.12(a) and 5.12(b) are understandable. It is also possible to assign the corrugations as the Y and Ba atoms. However, it is more plausible to assume that the CuO_2 layer, which is responsible for the quasi-2D conduction of this system, appears in the STM images. Therefore, we conclude that the atomic corrugations in Fig. 5.12 correspond to Cu atoms, and the brighter duplex layer is the CuO_2

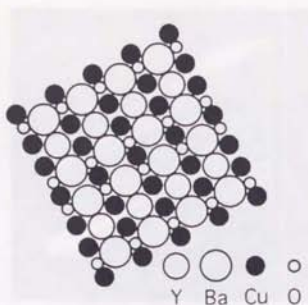


Fig. 5.13 Schematic diagram of the (110) plane of YBCO.

double layer. This implies that the CuO chain layer is also conductive relative to the Y and BaO layers, but has lower density of states compared to the CuO_2 layer near the Fermi level. This conductive nature of the CuO chain layer must be the origin of the small anisotropy of this system compared to other HTSC's.

This result is very consistent with the result of the LDA band-structure calculation [Refs. 16-18]. Fig. 5.1(c) demonstrates the calculated partial density of states for each site. The negative tip bias voltage corresponds to the unoccupied states of the specimen. Near the E_F (0.75 eV of the $E-E_F$ in the figure), the Cu site of the CuO_2 layer possesses more density of states than that of the CuO chain layer. At the higher energy (1.9 eV), the density of states of these two Cu sites become the same asymptotically. This directly explains the bias voltage dependence of the STM image observed on the (110) plane as described above.

5.5 STS Measurements on (110) Oriented YBCO Thin Films

5.5.1 Spatial Variation of Electronic Structure

Fig. 5.12 shows light and dark areas which are observed in the images independent of the tip bias voltage. Fig. 5.14 demonstrates an STM image with a larger scanning area. Each of the bright line in the figure corresponds to a pair of CuO_2 layers, being enhanced with a lower tip bias voltage of -0.5 V. In Fig. 5.14, large swells and depressions are observed as stripes perpendicular to the c -axis of dimensions of a few to several nano-meter wide. We measured a series of tunneling spectra during one scan along the line indicated in Fig. 5.12(b) by the arrows between the STM

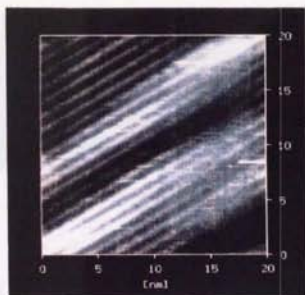


Fig. 5.14 STM image of the (110) plane of the YBCO epitaxial film measured at 4.2 K. $V_b = -0.5$ V, $I_p = 0.28$ nA.

imaging of Figs. 5.12(a) and 5.12(b). Fig. 5.15 shows the result of this STS measurement. Fig. 5.15(a) is the sectional view of the surface topography, indicating the measuring locations of tunneling spectroscopy (A-L in the figure). The spectra averaged over A-F and G-L locations are superimposed in Fig. 5.15(b). On the line of points A-F, which corresponds to the swell in the image, the tunneling spectra had a metallic nature with a superconducting gap structure, while the spectra showed a semiconducting gap of -0.1 eV on G-L corresponding to the depression. Similar results were obtained at several other locations. These results indicate that the electronic structure of the surface changed in relation to the undulation along the c -axis with a distance scale of a few to several nano-meter, and the swells and depressions in the STM images correspond to superconducting and semiconducting regions, respectively.

We would like to discuss the possible origins of this spatial variation of the electronic structure. It seems to be natural to consider the observed undulation along the c -axis as a topographic feature of the surface itself. However, this cannot give a convincing explanation for changing the electronic structure. One possibility is the ordering of oxygen atoms. It is well known that YBCO has oxygen nonstoichiometry mainly on the CuO chain layer, and oxygen content changes the hole concentration which determines the electronic nature of this system [Refs. 43, 44]. If the oxygen atoms concentrate preferentially on some CuO chain planes, the hole concentration varies microscopically in the crystal, and this alters the local electronic structure along the c -axis in the observed manner. Another possible origin may be the stress effect. We deposited a PBCO template layer before deposition of YBCO because the c -spacing of SrTiO_3 substrate is longer than that of YBCO. However, the film before annealing in O_2 atmosphere had low T_c of ~ 50 K owing to the stress effect [Ref. 45]. After annealing in O_2 , the c -axis length decreased and the T_c was raised up to 85 K which was, however, lower than the maximum T_c of this system, 90 K. We

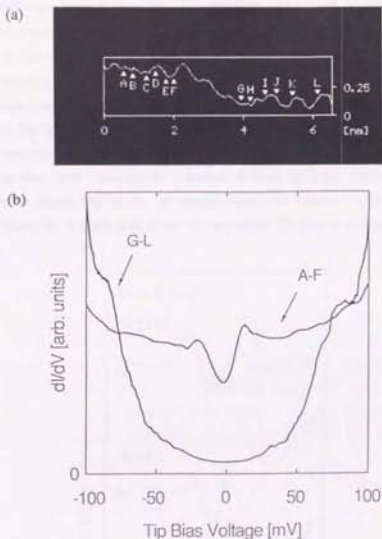


Fig. 5.15 STS measurement on the (110) plane of the YBCO epitaxial film at 4.2 K. (a) The sectional view showing the locations of tunneling spectroscopy measurements (A-L, marked by \blacktriangle), $V_b = -0.1$ V, $I_p = 0.1$ nA. (b) The tunneling spectra averaged over A-F and G-L locations.

cannot exclude the possibility of the presence of residual stress. If we assume that the stress concentrates in some areas, the superconductivity of the stressed areas may be destroyed while other relaxed areas are superconducting, hence resulting in the same feature. The above two possible mechanisms may be combined because increase of oxygen content decreases the c -axis length and relaxes the crystal. Although it is not clear, at the present moment, that the observed features reflected bulk ones, we would like to suggest a possibility of occurrence of some kind of microscopic phase separation. In either case of the possible mechanisms, the microscopic phase separation is thought to decrease the total free energy of the thin film structure. Further investigations should be made on this subject.

5.5.2 Tunneling Spectroscopy Changing Barrier Width

Fig. 5.16 shows tunneling spectra with various barrier widths on the (110) surface of a YBCO film measured in the same way described above, when the spectra showed a superconducting feature. The tunneling spectra always show a metallic nature and superconducting gap structure with high zero-bias conductance independent of the tip-sample distance. Apparently, this behavior is different from the results of the same measurement performed on the *a-b* basal plane. The behavior of the spectrum measured on the *a-b* plane can be explained by assuming that the spectrum consists of more than two components contributed from different layers, and the ratio of the contributions varies depending on the tip-sample separation because of the change of the barrier shape. This explanation is applicable to the system where 2D planes normal to the simply assumed

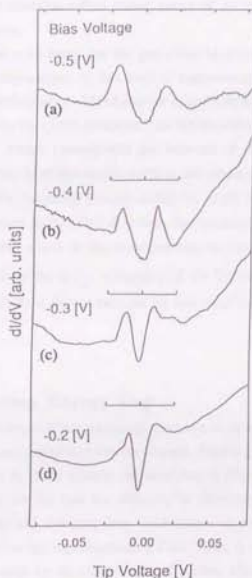


Fig. 5.16 Tunneling spectra measured with various barrier widths on the (110) surface of a YBCO thin film at 4.2 K. V_b 's are (a) -500 mV, (b) -400 mV, (c) -300 mV, (d) -200 mV, respectively. $I_p = 2$ nA const. Zero conductance value is shown by the line under each spectrum.

tunneling direction are piled up. However, in the case of the (110) plane, the situation is completely different. The edges of all the 2D planes parallel to the tunneling direction appear on the surface. The tunneling spectrum must also have components from different planes, but the ratio of the contributions depends rather on the lateral tip position than the tip height. Since the edges of the conductive CuO_2 and CuO planes appear, there must be enough surface states and the STM tip cannot go to the vicinity of the surface unlike the case that it is covered with an insulating layer. This suggests that the tunneling area cannot become extremely small but is kept larger than some extent which contains more than one plane. The tunneling area can change depending on the tip-sample distance. However, this tunneling direction has a simple vacuum barrier, thus the tunneling current decays rapidly as the distance increases, which means that the change of tunneling resistance corresponds to very small change of the tip height. All these situations make the tunneling spectrum in this direction reflect mixed nature of the planes without remarkable change depending on the tip position.

Fig. 5.16 seems to have a tendency that the gap value becomes small as the tip is closer to the sample surface, although the number of this kind of measurement on the (110) plane is not large enough to discuss the reproducibility. This behavior is understandable if we assume the anisotropic gap which has maximum in the (110) direction. As the tip-sample separation becomes small, the tunneling area decreases, which corresponds the increase of the probed area in the k -space. Therefore, if the tip is further from the sample surface, the nature reflected in the spectrum is limited to the information about the tunneling process along the (110) direction. If the superconducting order parameter has maximum in the (110) direction, the spectrum must show a larger gap with the larger tip-sample separation, which is the same manner as shown in Fig. 5.16. This result is opposite to that expected from the $d_{x^2-y^2}$ symmetry of the Cooper pair but consistent with the d_{xy} symmetry. Further investigation should be done on this topic in relation to the interest in the pair symmetry of the HTSC.

5.5.3 Superconducting Energy Gap

Fig. 5.17 indicates an example of the tunneling spectrum showing a superconducting energy gap. On the (110) plane, the superconducting spectra always show a gapless feature and high zero-bias conductance higher than 50 % of the normal one as shown in Figs. 5.16 and 5.17. This result was surprising for us, because we felt that the difficulty in observing the clear superconducting gap structure with a flat bottom and low zero-bias conductance on the a - b basal planes of the HTSC materials is due to the fact that the superconducting CuO_2 plane is covered with other layers in usual cases. Therefore, we expected, on the cross-sectional surface where the CuO_2 layer appear, it must be possible to probe the electronic nature of the CuO_2 plane directly without interference from other layers. However, as discussed in the former section, it seems that, on the cross-sectional plane, the spectrum always reflects the mixed nature of the planes included in the tunneling area. The CuO_2

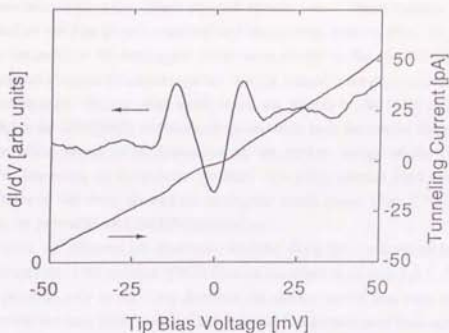


Fig. 5.17 Tunneling spectrum showing a superconducting feature measured on the (110) plane of a YBCO epitaxial film at 4.2 K. $V_g = -0.2$ V, $I_p = 0.1$ nA.

nature can be probed rather on the basal plane under the limited configuration of the planes near the surface as will be discussed in section 5.6.3 and Chapter 7. This situation is analogous to the fact that STM possesses higher resolution in the z -direction (~ 0.1 Å) than in the x , y -direction (~ 1 Å) owing to the sensitiveness of the tunneling current to the tip height.

The superconducting gap values measured on the (110) oriented films, which were roughly estimated from the peak-to-peak separations, ranged from 20 meV to 40 meV corresponding to $2\Delta/k_B T_c$ of 2.7–5.5 ($T_c \sim 85$ K). This scattering of the gap values may be also attributed to the variation of the local T_c in the superconducting swell region. Such variation is possibly caused by the quasi-2D electronic structure intrinsically, and also by the extrinsic effect such as the variation of the oxygen concentration as described in section 5.5.1. If the barrier width dependence of the gap energy discussed in the former section is true, it can also cause this scattering of the observed gap values. However, at present, we have never found any tendencies or rules of the scattering. A systematic experiment should be done.

5.6 Discussions

5.6.1 Growth Mechanisms of YBCO Thin Films

On (001) oriented YBCO films, two dimensional island structures have been observed by a number of researchers [Refs. 8–12]. Some groups reported rectangular shapes of the spirally rising

steps or the concentric rings, while others reported circular ones. These features of the island structure depended on the film growth condition and the substrate material [Ref. 10]. It has been pointed out that the sides of the rectangular island were parallel to the (100)/(010) directions. Hence, the rectangular shape of the island structure must be formed if the growth in the (100)/(010) directions is predominant. On the other hand, when the growth in the (110) direction occurs comparably to that in the (100)/(010) directions, the island must have the circular shape. Therefore, the shape of the island seems to be determined by the surface energy of the (110) and the (100)/(010) planes depending on the growth condition. The (001) oriented films fabricated under the growth condition of this work showed the rectangular island shapes [Fig. 5.3(a)], suggesting the dominance of the growth in the (100)/(010) directions.

On the other hand, we observed hill structures elongated along the *c*-axis which have trapezoid cross-sectional shapes on (110) oriented YBCO films as described in section 5.4.1. If the growth of the film had occurred only in the (110) direction, the surface would have been rather flat and these structures could not have been formed. Therefore, the film growth must have occurred in both the (110) and the (100)/(010) directions, forming both the (110) and the (100)/(010) planes competitively. Judging from Fig. 5.11(b), the formation of the (100)/(010) planes seems to be dominant.

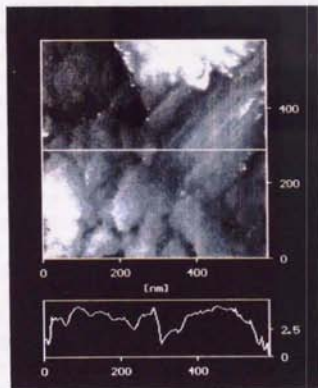


Fig. 5.18 STM image of the (100) surface of a laser-deposited YBCO thin film measured at 4.2 K (constant current mode).

These two results are consistent with each other suggesting the dominance of the film growth in the (100)/(010) directions of the YBCO system. If it is true, (100) oriented YBCO films are expected to have smoother surfaces than the (110) oriented films. Fig. 5.18 shows an STM image of a (100) oriented YBCO film grown by the same method under the same growth condition. In the image, a lot of grains and their boundaries are observed. The cross-sectional topographic view indicates the heights of the structures of 2-3 nm which are an order of magnitude lower than that observed on the (110) oriented films of ~20 nm, which confirms that our expectation is true.

5.6.2 Models for Surface Termination of (001) Oriented Film

As described above in section 5.2, we have observed steps with one unit cell height, which is consistent with other reports [Refs. 8-12]. Harmer *et al.* [Ref. 46] and Heyvaert *et al.* [Ref. 47] reported that repeated rastering with an STM tip on the *c*-axis oriented YBCO thin film removed surface atomic layers by field induced evaporation, and the removed layers were multiples of the *c*-spacing (1.2 nm). These observations suggest that the terminating layer of a (001) oriented YBCO thin film is always the same layer. Although the terminating atomic layer cannot be identified by the STM observation itself, there are a number of studies which have determined the termination. Liu *et al.* [Ref. 48] and Fowler *et al.* [Ref. 49] employed PES and x-ray photoelectron spectroscopy (XPS), respectively, to study cleaved single crystals of YBCO. They detected two Ba chemical states, a bulk one and a surface one, indicating a BaO-CuO₂- terminated structure. From the quantitative angle-resolved XPS (ARXPS) study of YBCO epitaxial films, Frank *et al.* concluded that the BaO termination with BaO-CuO-BaO-CuO₂- sequence is the most stable one [Ref. 50]. On the other hand, Terashima *et al.* examined YBCO thin films on SrTiO₃ substrates deposited by reactive evaporation under a high-resolution transmission electron microscope (TEM) and studied the superconducting properties of the one unit cell thick YBCO films [Ref. 51]. According to them, the core of the growth unit is the BaO-CuO₂-Y-CuO₂-BaO atomic layers, and the CuO chain layer is located on the top of the core. Tanaka *et al.* [Ref. 52] used low-energy ion scattering spectroscopy (ISSP) to examine the scattering of ions from Ba atoms on the surface of YBCO, and found a "shadow" in the scattering which they attributed to a chain oxygen atom diagonally above each Ba at the surface, which means also the CuO-BaO-CuO₂- termination. Pennycook *et al.* directly observed the amorphous/crystal interface in a *c*-axis oriented ion-implanted YBCO film by *z*-contrast electron microscopy, and also concluded the termination at the CuO chain layer [Ref. 53].

Summarizing these results, the possible termination is at the CuO chain layer, or at the BaO layer on the CuO chain layer, or at the BaO layer on the CuO₂ layer. We feel that the terminating layer is not necessarily the same for all the YBCO specimens including single crystals and thin films grown by various methods under various conditions. In either case, the terminating layer is not the CuO₂ layer which is thought to be essentially responsible for the quasi-two-dimensional superconductivity of this system. Our data can be explained reasonably if we assume the

BaO-CuO-BaO-CuO₂- termination for the usual cases indicating high zero-bias conductance and the BaO-CuO₂- termination for the rare case showing a finite superconducting gap with low zero-bias conductance as will be discussed in Chapter 7.

5.6.3 Origins of High Zero-Bias Conductance Values in Superconducting Spectra

A number of tunneling data on YBCO reported so far gave high conductance values, larger than 50 % of the normal conductance, in the superconducting gap region. On the other hand, most of the data measuring other compounds of HTSC did not show such high values [Ref. 54]. Actually we obtained tunneling spectra with zero-bias conductance values smaller than several % of the normal one when we observed BSCCO single crystals. Therefore this extremely high zero-bias conductance value seems to be a special feature of YBCO. Here, we would like to discuss the origin of the high zero-bias conductance observed in the YBCO system.

First, we try to explain two different observations on the (001) plane, *i.e.*, a superconducting gap with high zero-bias conductance observed in the usual cases, and a finite gap with a flat bottom with very low conductance inside the gap rarely observed. We can presume that the high value at zero-bias in the conductance curve can be attributed to extrinsic effects such as short circuiting and local destruction of superconductivity in the case of macroscopic tunneling methods such as planar, break and point-contact junctions. However, these extrinsic effects can be excluded in the present STS measurement which can avoid chemical reaction or mechanical damage of the material surface. In every measurement, the specimen was once exposed to ambient gas. Therefore, degradation of the surface does not seem to be the origin of the significant difference in the zero-bias conductance between these two results. It is mysterious to obtain both the high zero-bias conductance and the flat shape of the bottom in the gap structure at the same time in Fig. 5.9. Considering this rather flat bottom region around $V = 0$ in the conductance curve, it seems that a finite gap is opened in the quasi-particle excitation spectrum of the superconducting CuO₂ layer, and this high zero bias conductance is contributed by another layer whose electronic nature is close to normal metal. We speculate that the terminating layer was different depending on the growth condition, and the specimen showing high zero-bias conductance has a normal metallic layer formed between the surface semiconducting layer and the underlying CuO₂ layer. The special feature of the YBCO system which other HTSC materials don't have is the presence of the one dimensional CuO chain layer. There is a possibility that the CuO chain layer gives an additional band which has a normal metallic nature. Another explanation is that the CuO₂ layer nearest to the surface cannot become superconducting because the hole donor layers are not complete at the surface, and this normal CuO₂ layer yields the residual density of states in the midgap region. The former explanation seems to be preferable considering the consistency with the explanation for the result measured on the (110) surface presented below. If this normal metallic layer does not exist, a finite superconducting

gap is observed. The probability of the occurrence of this configuration of the planes near the surface seems to be very rare.

Next, we discuss the case of the (110) plane. Judging from the STM results on the (110) planes, the Y and BaO layers have no density of states near the Fermi level. Hence, the contribution from the Y and BaO layers to this high zero-bias conductance can be excluded. As mentioned above, the spectra shown in Fig. 5.10 suggest that a finite gap opens up in the quasiparticle excitation spectrum of the superconducting CuO_2 layer. A possible candidate for the origin of the extremely high zero-bias conductance in the (110) spectrum is the CuO chain layer. If we assume that the CuO chain layer is normal metallic or weakly-superconducting by a proximity effect, the present tunneling results are understood as follows. On the (110) plane, the tunneling occurs to both the superconducting CuO_2 layer and the normal metallic CuO chain layer as discussed in section 5.2.2. Hence, the spectrum shows the residual conductance originating from the CuO chain layer even in the superconducting gap region.

5.6.4 Symmetry of Cooper Pair

Symmetry of the Cooper pair must be the key feature to reveal the mechanism of the high temperature superconductivity. The original BCS theory [Ref. 55] adopted simple isotropic s -wave symmetry,

$$\Delta(k) = \Delta = \text{const.} \quad (5.1)$$

However, for the HTSC which has strong anisotropy, this symmetry may not be able to be applied. In order to take anisotropic features of the HTSC into account, the gap parameters which depend on k have been proposed (anisotropic s -wave). For such examples, following equations have been introduced by Schneider *et al.* [Ref. 56] and Kirtley *et al.* [Ref. 57], respectively, as discussed in section 4.6.2.

$$\Delta(k) = \Delta_1 - 2\Delta_2 \cos(k_x a) \quad (5.2)$$

$$\Delta(k) = \Delta_{ab} \sin^2 \theta - \Delta_c \cos^2 \theta \quad (5.3)$$

Although these gap parameters have k -dependence, at least, finite gap opens in all the directions, hence this symmetry is still s -wave.

On the other hand, it is well known that the HTSC has strong correlation. In the system accompanied by the on-site Coulomb repulsive force, the symmetry which has a node is advantageous. The $d_{x^2-y^2}$ symmetry

$$\Delta(k) \sim \cos k_x a - \cos k_y a \quad (5.4)$$

has a four fold node in the direction of the diagonal of the CuO_2 network. On the other hand, the extended s -wave symmetry

$$\Delta(k) \sim \cos k_x a + \cos k_y a \quad (5.5)$$

shows an eight fold node.

Whether the superconducting gap of the HTSC has a node or not has lately attracted considerable attention, because a half of the proposed mechanisms for the high temperature superconductivity could be ruled out if it became clear. Therefore, the experiments to elucidate this problem become the most significant recently. Under a realistic condition, tunneling spectroscopy using macroscopic junction methods can obtain information about k -dependent features. For example, in the case of $d_{x^2-y^2}$ symmetry, if the junction is formed on the (110) plane of a HTSC material, no superconducting gap must be observed in the spectrum. However, the interface of a real junction does not have an atomically flat surface over the wide area, but locally has step structures and planes of other orientations which cause electron diffraction at the interface and electron tunneling in the different directions. Therefore it seems to be quite difficult to prove the existence of a node in the gap symmetry by using these methods.

On the contrary, in STM, the tunneling area is very small, and atomical smoothness of such a small area is actually possible. STM observations before the spectroscopic measurements allow to choose such a smooth area. However, in this case, the too small tunneling area causes a problem of the uncertainty of momentum. As is well known, uncertainty principle is expressed by the following equation.

$$\Delta x \Delta p \geq \frac{\hbar}{2} \quad (5.6)$$

Since STM possesses atomic resolution, the tunneling area, which determines the uncertainty in the real space (Δx), must be not more than the order of the lattice parameter a .

$$\Delta x \leq a \quad (5.7)$$

Thus we obtain for the uncertainty of momentum

$$\Delta p \geq \frac{\hbar}{2a} \quad (5.8)$$

Considering the relation $p = (\hbar/2\pi)k$, Eq. 5.8 gives

$$\Delta k \geq \frac{1}{2a} \quad (5.9)$$

where $1/2a$ corresponds to $1/4\pi$ of the first Brillouin zone ($-\pi/a \leq k \leq \pi/a$). Therefore the tunneling spectrum measured by STM reflects information integrated in the k -space. From this reason, we cannot derive k -dependent information from the data measured with STM. However, paradoxically, we can verify s -wave symmetry of the Cooper pair based on the tunneling data with STM if the observed material has it. The spectrum reflecting k -integrated information should always show a finite gap in the case of s -wave, and a gapless feature in the case of d -wave independent of the observing direction.

As discussed in Chapter 4 and Chapter 5, we obtained the tunneling spectra clearly showing finite superconducting energy gaps with flat bottoms and very low zero-bias conductance values on both BSCCO [Figs. 4.14, 4.25(b), 4.25(c)] and YBCO (Fig. 5.10). These spectra were measured on the a - b basal plane. From this direction, the k -integrated spectra cannot avoid the influence of the node if it exists. The fact that these spectra were measured on BSCCO and YBCO strongly suggests that these materials have s -wave gap symmetry. The probability of observing this kind of spectra is not so high. However, we would like to point out that there is no extrinsic reason why a finite superconducting gap appears in the spectrum. On the contrary, there are a number of

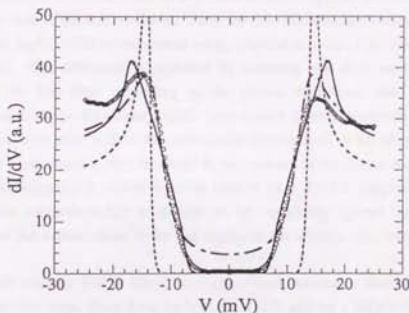


Fig. 5.19 Comparison of the observed tunneling spectrum on the (001) plane of YBCO with spectral functions predicted from various models.

○: experimental data, —: BCS function assuming $\Delta = 15$ meV, - - -: Dynes function assuming $\Delta = 13$ meV and $\Gamma = 2$ meV, — — —: layered model proposed by Schneider *et al.* assuming $\Delta_1 = 12$ and $\Delta_2 = 5$ meV.

extrinsic effects which cause the broadening of a superconducting gap, thus it is meaningless to insist d -wave symmetry based on the tunneling data indicating a broad gap structure. Fig. 5.19 demonstrates the comparison of the observed tunneling spectrum on the YBCO (001) plane (Fig. 5.10) with spectral functions predicted from various s -wave models. The data can be fitted well to the conductance curve calculated from the anisotropic s -wave model proposed by Schneider *et al.* [Ref. 56].

5.7 Conclusions

We have performed STM/STS observations at 4.2 K in order to probe the topographic and electronic properties of the (001) and (110) surfaces of YBCO epitaxial films. On the (001) plane, a square lattice of surface atoms with the a - or b -spacing (0.4 nm) was clearly observed in the STM images together with step structures with height of 1.2 nm which was always equal to the c -spacing of the YBCO unit cell. Therefore the surface of the c -axis oriented YBCO film was covered with the same layer over the entire surface of the specimen which was stable and free from severe reaction with ambient gas. We speculate that the tunneling current on the basal plane is composed of two different contributions; one from the non-superconducting surface layer whose thickness seems to be atomic size and the other from the superconducting CuO_2 layer underneath the top covering layer, and that the contribution from the CuO_2 layer becomes dominant when the tip-sample distance is small and hence the superconducting energy gap is observable only under this condition. In most of the (001) oriented films, the zero-bias conductance in the superconducting state was rather high (~50% of the normal value) whereas in some of the specimens it was as low as 1% or less. This difference is explained by assuming that there are two kinds of surface structures of the thin films depending on the growth conditions; one is composed of the semiconducting top layer, the normal metallic layer beneath it, and the superconducting layer further beneath them, and the other without the intermediate normal layer. If we adopt this assumption, the high zero-bias conductance is then attributed to the presence of the normal metallic layer, therefore the superconducting gap ($2\Delta \sim 40$ meV giving value of $2\Delta/k_B T_c \sim 5.2$, suggesting a strong coupling regime for this superconductor) is thought to be completely opened up in the CuO_2 band considering the flat bottom shape in the gap region of the spectra, *i.e.*, s -wave symmetry of the Cooper pair.

On the (110) oriented YBCO films, semi-macro scale structures observed in the wide scan images suggest that these films grew in both the (110) and the (100)/(010) directions and the competition between formations of the (110) and the (100)/(010) planes occurred. Atomic resolution STM pictures imaged Cu atoms of both the CuO and CuO_2 layers clearly, and a couple of layers were enhanced relatively to the adjacent layer with low tip bias voltage. These enhanced layers and their adjacent layer are assigned as the CuO_2 double layer and the CuO chain layer, respectively, implying that the CuO chain layer is conductive but has lower density of states near the Fermi level than the CuO_2 layer. Furthermore, we observed a broad undulation in the

c-direction. The results of STS measurements indicated a superconducting nature on the swells and a semiconducting nature on the depressions, suggesting occurrence of some kind of microscopic phase separation. The tunneling spectra measured on the swell region show a superconducting property with a gapless feature and high zero-bias conductance. This spectral feature is understandable if we consider the tunneling spectrum as a convolution of the contribution from the superconducting CuO_2 layer and that from the normal metallic CuO chain layer.

References

- [1] J. R. Kirtley, R. T. Collins, Z. Schlesinger, W. J. Gallagher, R. L. Sandstrom, T. R. Dinger, and D. A. Chance, *Phys. Rev. B* 35, 8846 (1987).
- [2] L. E. C. van de Leemput, P. J. M. van Bentum, L. W. M. Schreurs, and H. van Kempen, *Physica C* 152, 99 (1988).
- [3] A. M. Okoniewski, J. E. Klemberg-Sapieha, and A. Yelon, *Appl. Phys. Lett.* 53, 151 (1988).
- [4] H. L. Edwards, J. T. Markert, and A. L. de Lozanne, *Phys. Rev. Lett.* 69, 2967 (1992).
- [5] H. L. Edwards, A. L. Barr, J. T. Markert, and A. L. de Lozanne, *Phys. Rev. Lett.* 73, 1154 (1994).
- [6] S. Pan, K. W. Ng, A. L. de Lozanne, J. M. Tarascon, and L. H. Greene, *Phys. Rev. B* 35, 7220 (1987).
- [7] M. E. Hawley, K. E. Gray, D. W. Capone II, and D. G. Hinks, *Phys. Rev. B* 35, 7224 (1987).
- [8] C. Gerber, D. Anselmetti, J. G. Bednorz, J. Mannhart, and D. G. Schlom, *Nature* 350, 279 (1991).
- [9] M. Hawley, I. D. Raistrick, J. G. Beery, and R. J. Houlton, *Science* 251, 1587 (1991).
- [10] J. Moreland, P. Rice, S. E. Russek, B. Jeanneret, A. Roshko, R. H. Ono, and D. A. Rudman, *Appl. Phys. Lett.* 59, 3039 (1991).
- [11] H. P. Lang, T. Frey, and H. -J. Güntherodt, *Europhys. Lett.* 15, 667 (1991).
- [12] H. P. Lang, H. Haefke, G. Leemann, and H. -J. Güntherodt, *Physica C* 194, 81 (1992).
- [13] M. C. Gallagher, and J. G. Adler, *J. Vac. Sci. Technol. A* 8, 464 (1990).
- [14] R. Wilkins, M. Amman, R. E. Soltis, E. Ben-Jacob, and R. C. Jaklevic, *Phys. Rev. B* 41, 8904 (1990).
- [15] J. R. Kirtley, *Int. J. Mod. Phys. B* 4, 201 (1990).
- [16] S. Massida, J. Yu, A. J. Freeman, and D. D. Koelling, *Phys. Lett. A* 122, 198 (1987).
- [17] J. Yu, S. Massida, A. J. Freeman, and D. D. Koelling, *Phys. Lett. A* 122, 203 (1987).
- [18] L. F. Mattheiss, and D. R. Hamann, *Solid State Commun.* 63, 395 (1987).
- [19] P. D. Johnson, S. L. Qiu, L. Jiang, M. W. Ruckman, M. Strongin, S. L. Hulbert, R. F. Garret, B. Sinkovic, N. V. Smith, R. J. Cava, C. S. Jee, D. Nichols, E. Kaczanowicz, R. E. Salomon, and J. E. Crow, *Phys. Rev. B* 35, 8811 (1987).

- [20] A. Fujimori, E. Takayama-Muromachi, Y. Uchida, and B. Okai, *Phys. Rev. B* 35, 8814 (1987).
- [21] N. Nücker, J. Fink, B. Renker, D. Ewert, C. Politis, P. J. W. Weijs, and J. C. Fuggle, *Z. Phys. B* 67, 9 (1987).
- [22] K. L. Kurtz, R. L. Stockbauer, D. Mueller, H. Shih, L. E. Toth, M. Osofski, and S. A. Wolf, *Phys. Rev. B* 35, 8818 (1987).
- [23] Z. Shen, J. W. Allen, J. J. Yeh, J.-S. Knag, W. Ellis, W. Spicer, I. Lindau, M. B. Maple, Y. D. Dalichaouch, M. S. Torikachvili, J. Z. Sun, and T. H. Geballe, *Phys. Rev. B* 36, 8414 (1987).
- [24] T. Takahashi, F. Maeda, H. Arai, H. Katayama-Yoshida, Y. Okabe, T. Suzuki, S. Hosoya, A. Fujimori, T. Shidara, T. Koide, T. Miyahara, M. Onoda, S. Shamoto, and M. Sato, *Phys. Rev. B* 36, 5686 (1987).
- [25] M. Onellion, Y. Chang, D. W. Niles, R. Joynt, G. Margaritondo, N. G. Stoffel, and J. M. Tarascon, *Phys. Rev. B* 36, 819 (1987).
- [26] P. Steiner, *Z. Phys. B* 66, 275 (1987).
- [27] H. M. Meyer, D. M. Hill, T. J. Wagener, Y. Gao, J. H. Weaver, D. W. Capone, and K. Goretta, *Phys. Rev. B* 38, 6500 (1988).
- [28] R. S. List, A. J. Arko, Z. Fisk, S.-W. Cheong, S. D. Conradson, J. D. Thompson, C. B. Pierce, D. E. Peterson, R. J. Bartlett, N. D. Shinn, J. E. Schirber, B. W. Veal, A. P. Paulikas, and J. C. Campuzano, *Phys. Rev. B* 38, 11966 (1988).
- [29] B. W. Veal, A. P. Paulikas, K. Vandervoort, H. Claus, J. C. Campuzano, C. G. Olson, A.-B. Yang, R. Liu, C. Gu, R. S. List, A. J. Arko, and R. J. Bartlett, *Physica C* 158, 276 (1989).
- [30] J. C. Campuzano, G. Jennings, M. Faiz, L. Beaulaigue, B. W. Veal, J. Z. Liu, A. P. Paulikas, K. Vandervoort, H. Claus, R. S. List, A. J. Arko, and R. J. Bartlett, *Phys. Rev. Lett.* 64, 2308 (1990).
- [31] C. J. Chen, *J. Vac. Sci. Technol. A* 6, 319 (1988).
- [32] N. Isshiki, K. Kobayashi, and M. Tsukada, *Surf. Sci.* 238, L439 (1990).
- [33] K. Kobayashi, M. Tsukada, and N. Isshiki, *Solid State Commun.* 74, 1187 (1990).
- [34] K. Kobayashi, and M. Tsukada, *J. Vac. Sci. Technol. A* 8, 170 (1990).
- [35] S. Ohnishi, and M. Tsukada, *J. Vac. Sci. Technol. A* 8, 174 (1990).
- [36] N. Isshiki, K. Kobayashi, and M. Tsukada, *J. Vac. Sci. Technol. B* 9, 475 (1991).
- [37] M. Tsukada, K. Kobayashi, N. Shima, and N. Isshiki, *J. Vac. Sci. Technol. B* 9, 492 (1991).
- [38] G. Deutscher, and K. A. Müller, *Phys. Rev. Lett.* 59, 1745 (1987).
- [39] A. Edgar, C. J. Adkins, and S. J. Chandler, *J. Phys. C* 20, L1009 (1987).
- [40] P. Chaudhari, R. T. Collins, P. Freitas, R. J. Gambino, J. R. Kirtley, R. H. Koch, R. B. Laibowitz, F. K. LeGoues, T. R. McGuire, T. Penney, Z. Schlesinger, A. P. Segmüller, S. Foner, and E. J. McNiff, Jr., *Phys. Rev. B* 36, 8903 (1987).

- [41] M. Gurvitch, J. M. Valles, Jr., A. M. Cucolo, R. C. Dynes, J. P. Garno, L. F. Schneeneyer, and J. V. Waszczak, *Phys. Rev. Lett.* 63, 1008 (1989).
- [42] T. Hasegawa, and K. Kitazawa, *Jpn. J. Appl. Phys.* 29, L434 (1990).
- [43] R. J. Cava, A. W. Hewat, E. A. Hewat, B. Batlogg, M. Marezio, K. M. Rabe, J. J. Krajewski, W. F. Peck Jr., and L. W. Rupp Jr., *Physica C* 165, 419 (1990).
- [44] J. D. Jorgensen, S. Pei, P. Lightfoot, H. Shi, A. P. Paulikas, and B. W. Veal, *Physica C* 167, 571 (1990).
- [45] E. Olsson, A. Gupta, M. D. Thouless, A. Segmuller, and D. R. Clarke, *Appl. Phys. Lett.* 58, 1682 (1991).
- [46] M. A. Harmer, C. R. Fincher, and B. A. Parkinson, *J. Appl. Phys.* 70, 2760 (1991).
- [47] I. Heyvaert, E. Osquiguil, C. van Haesendonck, and Y. Bruynseraede, *Appl. Phys. Lett.* 61, 111 (1992).
- [48] R. Liu, *Phys. Rev. B* 40, 2650 (1989).
- [49] D. E. Fowler, C. R. Brundle, J. Lerczak, and F. Holtzberg, *J. Electron. Spectrosc. Relat. Phenom.* 52, 323 (1990).
- [50] G. Frank, Ch. Ziegler, and W. Gopel, *Phys. Rev. B* 43, 2828 (1991).
- [51] T. Terashima, K. Shimura, Y. Daitoh, Y. Yano, Y. Matsuda, S. Komiyama, and Y. Bando, *Proc. of MRS Spring Meeting, San Francisco, 1992.*
- [52] S. Tanaka, *Appl. Phys. Lett.* 59, 3637 (1991).
- [53] S. J. Pennycook, M. F. Chisholm, D. E. Jesson, D. P. Norton, D. H. Lowndes, R. Feenstra, H. R. Kerchner, and J. O. Thomson, *Phys. Rev. Lett.* 67, 765 (1991).
- [54] See T. Hasegawa, H. Ikuta, and K. Kitazawa, *Physical Properties of High Temperature Superconductors III*, edited by D. M. Ginsberg, World Scientific Publishing, 525 (1992).

Chapter 6

Typical Structures Appeared in Tunneling Spectra by Extrinsic Effects

It has been demonstrated that spurious structures of various extrinsic origins may often be observed in the tunneling spectra on the HTSC's. Because these structures could easily be misinterpreted as a superconducting gap or as phonon structures, caution needs to be taken in interpreting the obtained spectra. Here we examine the frequently reported cases which we believe to be related to extrinsic effects: charging effect (Fig. 6.1), a dip structure in the conductance

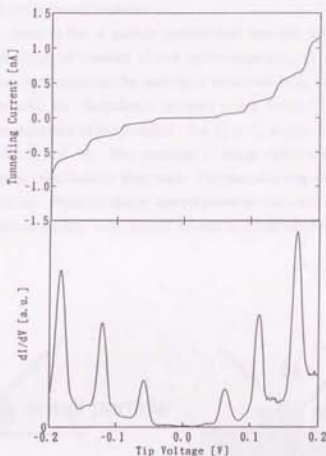


Fig. 6.1 I - V and differential conductance curves indicating multiple-peak structures with equal inter-peak spacing caused by charging effect of a capacitive small particle between the tip and the sample observed on the (001) plane of YBCO at 4.2 K after scanning with very low tip bias voltage. $V_b = -200$ mV, $I_p = 0.8$ nA.

spectrum due to a proximity effect (Figs. 6.3, 6.4), and zero-bias anomaly arising from the same origin (Fig. 6.5). All these structures were observed also in our tunneling measurements using STM only when the probe tip crashed onto or contacted with the sample surface with very low tip bias voltage of $V_b \leq 50$ mV [Figs. 6.1-6.3]. Hence we can claim that these are extrinsic structures, and the tunneling spectrum did not indicate these structures when the tip is well-controlled under an usual condition.

Especially in the early data, multiple-peak structures often appeared with nearly equal inter-peak spacing, and were discussed in terms of multiple superconducting gaps [Refs. 1, 2]. Ruggiero *et al.* [Refs. 3-5] suggested that these were likely to result from the quantized charging of small particles (Coulomb staircase), based on their observation of similar effect on a junction of Ag-Al₂O₃-Ag with tiny Ag particles sandwiched in the tunneling region. van Bentum *et al.* [Ref. 6] also observed the effect on YBCO with STM, possibly due to small metallic particles unintentionally introduced on the sample surface. Fig. 6.1 shows a typical spectrum indicating the charging effect measured on a (001) oriented YBCO thin film with our cryogenic STM at 4.2 K, after scanning with low tip bias voltage of 20 mV which must have caused chipping of the specimen surface and yielded small particles.

When a tunneling junction has a particle sandwiched between the two electrodes [see Fig. 6.2(a)], an equivalent circuit of a series of two micro-capacitors, C_1 and C_2 , may be conceived [Refs. 7, 8]. Because the charge on the particle is quantized as $Q = ne$ and the voltage of the capacitors changes by e/C_i , the conductance becomes a step function if $C_1 \gg C_2$ or $R_1 \gg R_2$, where R_i is the Ohmic resistance of the junction. For $C_1 \cong C_2$, a gap should appear because of the Coulomb blockade effect [Ref. 9]. The presence of many particles could produce a V-shaped conductance by summing contributions from each. The particles may either be broken chips of the sample or foreign particles. Because equally spaced peaks are expected and the spacing varies with a change in the geometrical factors, one should be able to discriminate the charging effect from the

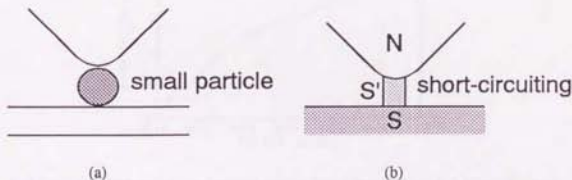


Fig. 6.2 Schematic diagrams of the tip and sample conditions for (a) Fig. 6.1, (b) Figs. 6.3-6.5.

intrinsic structure by changing the contact pressure (point contact) or the tip-surface distance (STM).

Another frequent observation in the tunneling conductance of the HTSC's has been the sharp dips which appear symmetrically with respect to $V = 0$ [Refs. 10-12]. Fig. 6.3 shows a typical example of tunneling spectra accompanied with this bilateral dip structures measured on the cleaved surface of a BSCCO single crystal at 4.2 K. This structure often shows hysteresis for upward and downward voltage sweeps, and has been attributed to the switching effect of microscopic supercurrent paths [see Fig. 6.2(b)]. The voltage where it appears shifts towards $V = 0$ under a magnetic field and at higher temperature [Refs. 11, 12]. This dip structure disappears above T_c . The shift of the voltage with T is in accordance with the change in the critical current of the supercurrent path [Ref. 13]. Therefore, even if an observed dip structure disappears at T_c , one should not simply say it must be related to a superconducting gap. There seem to be many reports in which this sort of dip structure has been discussed in terms of phonon structures or a superconducting gap.

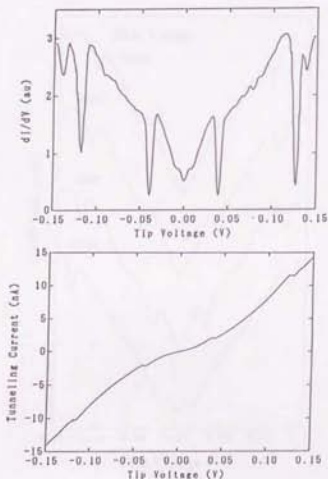


Fig. 6.3 I - V and differential conductance curves indicating bilateral dip structures caused by switching effect of microscopic supercurrent paths observed on the a - b plane of BSCCO at 4.2 K. $V_b = -50$ mV, $I_p = 2$ nA.

Fig. 6.4 demonstrates the tunneling spectra indicating the dip structures measured with various tip bias voltages from 55 mV to 40 mV and constant set-point current of 2 nA, *i.e.*, various tunneling resistances, at the same point on the cleaved surface of a BSCCO single crystal at 4.2 K. This series of tunneling spectra show two pairs of dips at symmetrical positions. This suggests the existence of two supercurrent paths between the tip and the specimen. These dips shift in a systematic manner that the pair of dips at higher voltage shifts towards $V = 0$ as the tunneling resistance decreases while that at lower voltage shows opposite behavior. This seems to be because one contact area of the path decreased and the other increased as the tip height was varied by changing the bias voltage. This result proves that this kind of dip structure is not intrinsic one.

A zero-bias conductance peak (ZBCP) has been found even in conventional superconductors [Refs. 14-16] and it has been discussed in relation to a magnetic impurity state [Refs. 17, 18]. Various types of ZBCP's have been discussed frequently in HTSC's. They can be attributed to the formation of a microscopic short circuit in the junction like in the case of the dip structure discussed above. If this is the case, they should be suppressed by a magnetic field, and indeed such a

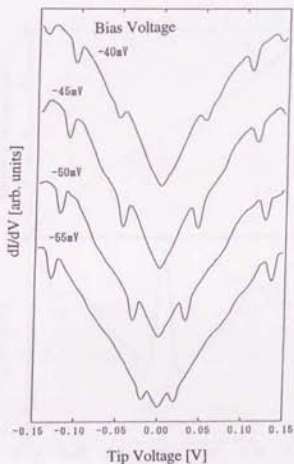


Fig. 6.4 Tunneling spectra showing bilateral dip structures caused by switching effect of microscopic supercurrent paths measured with various tunneling resistances on the a-b plane of BSCCO at 4.2 K. $V_b = -40, -45, -50, -55$ mV, $I_p = 2$ nA const.

suppression has been observed [Ref. 19]. The difference between the dip structure and the ZBCP must be the contact area which determines the critical current of the supercurrent path. When the contact area is very small, the voltage at which the superconductivity of the path is broken becomes low and the difference between the resistance before and after the break becomes large, which yields not dips but a peak at $V = 0$. Fig. 6.5 indicates a typical tunneling spectrum showing the ZBCP measured on the cleaved surface of a BSCCO single crystal at 4.2 K. It should be noted that this spectrum also indicates the dip structure, suggesting the essentially same origin of these two extrinsic structures.

This ZBCP is often interpreted as the Andreev reflection [Refs. 20, 21]. However, if this ZBCP is caused by the Andreev reflection, the height of the conductance peak should be lower than twice of the normal conductance. There are lots of spectrum data measured on the HTSC showing much higher ZBCP's. Moreover, according to the BTK (Blonder-Tinkham-Klapwijk) theory [Ref. 21], the conductance peak inside the superconducting gap is observed only when the ratio of the Fermi velocity of the normal tip to that of the superconductor $r = v_{FN}/v_{FS}$ is smaller than 1.0 ($r < 1.0$).

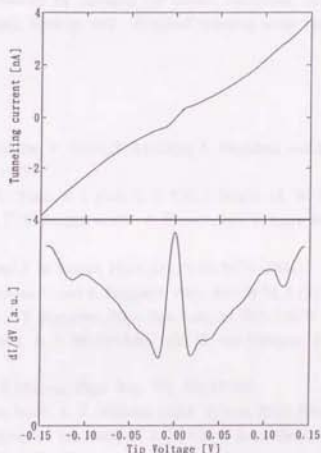


Fig. 6.5 I - V and differential conductance curves indicating a zero-bias conductance peak caused by switching effect of microscopic supercurrent paths with very small critical current observed on the a - b plane of BSCCO at 4.2 K. $V_b = -50$ mV, $I_p = 1$ nA.

The value of v_F can be calculated from the expression for the coherence length, $\xi_0 = \hbar v_F / \pi \Delta$. Using experimental values, e.g., of the YBCO system, $\xi_{ab} = 15 \text{ \AA}$ and $\Delta = 20 \text{ meV}$, we obtain $v_{FS} = 1.5 \times 10^7 \text{ cm/sec}$. On the other hand, an ordinary metal, e.g., Au has $v_{FN} = 1.4 \times 10^8 \text{ cm/sec}$. [Ref. 22]. Therefore the value of r of the SN junction between an ordinary metal and the HTSC cannot be smaller than 1.0. This implies that a sharp ZBCP should not be observed on the HTSC's in terms of the Andreev reflection.

Tanaka *et al.* [Ref. 23] recently calculate the conductance curves expected on an SN junction assuming $d_{x^2-y^2}$ symmetry of the superconductor with various values of parameters. Their result predicts that the conductance curve has a sharp ZBCP if the value of r equals to 5.0 and the tunneling direction has an angle of 45° to the Cu-O bond direction of the CuO_2 plane. They attribute the ZBCP observed on the HTSC's to d -wave superconductivity of this system. However, the tunneling process in a real junction is not coherent, so that the conductance peak should be broadened, especially in the case of the STM tunneling. The observed ZBCP seems to be too sharp to be explained by their calculation result.

To conclude this Chapter, we would like to stress that the tunneling spectrum should be examined for reproducibility by changing the contact conditions, and if possible, should be examined under magnetic fields as well. A typical spectrum under one condition is not always intrinsic.

References

- [1] I. Iguchi, H. Watanabe, Y. Kasai, T. Mochiku, A. Sugishita, and E. Yamaka, *Jpn. J. Appl. Phys.* 26, L645 (1987).
- [2] J. R. Kirtley, C. C. Tsuei, S. I. Park, C. C. Chi, J. Rozen, M. W. Shafer, W. J. Gallagher, R. L. Sandstrom, T. R. Dinger, and D. A. Chance, *Jpn. J. Appl. Phys.* 26, Suppl. 26-3, 997 (1987).
- [3] S. T. Ruggiero, and J. B. Barner, *Phys. Rev. B* 36, 8870 (1987).
- [4] K. Mullen, E. Ben-Jacob, and S. Ruggiero, *Phys. Rev. B* 38, 5150 (1988).
- [5] J. B. Barner, and S. T. Ruggiero, *Phys. Rev. Lett.* 59, 807 (1987).
- [6] P. J. M. van Bentum, R. T. M. Smokers, and H. van Kempen, *Phys. Rev. Lett.* 60, 2543 (1988).
- [7] H. R. Zeller, and I. Giaever, *Phys. Rev.* 181, 789 (1969).
- [8] K. Mullen, E. Ben-Jacob, R. C. Jaklevic, and Z. Schuss, *Phys. Rev. B* 37, 98 (1988).
- [9] P. J. M. van Bentum, H. van Kempen, L. E. C. van de Leemput, and P. A. A. Teunissen, *Phys. Rev. Lett.* 60, 369 (1988).
- [10] H. Koch, R. Cantor, J. F. March, H. Eickenbusch, and R. Schöllhorn, *Phys. Rev. B* 36, 722 (1987).
- [11] S. Takacs, S. Benacka, A. Plecenik, and V. M. Svistunov, *Physica C* 162-164, 1049 (1989).

- [12] T. Walsh, J. Moreland, R. H. Ono, and T. S. Kalkur, *Phys. Rev. B* 43, 11492 (1991).
- [13] J. S. Tsai, Y. Kubo, and J. Tabuchi, *Jpn. J. Appl. Phys.* 26, L701 (1987).
- [14] E. L. Wolf, *Principles of Electron Tunneling Spectroscopy*, Oxford University Press, New York, 395 (1985).
- [15] A. F. G. Wyatt, *Phys. Rev. Lett.* 13, 401 (1964).
- [16] L. Y. L. Shen, and J. M. Rowell, *Phys. Rev.* 165, 566 (1968).
- [17] J. Appelbaum, *Phys. Rev. Lett.* 17, 91 (1966).
- [18] P. W. Anderson, *Phys. Rev. Lett.* 17, 95 (1966).
- [19] T. Lehnert, H. Riedel, and K. Keck, *Solid State Commun.* 71, 953 (1989).
- [20] A. E. Andreev, *Sov. Phys. JETP* 19, 1228 (1964).
- [21] G. E. Blonder, M. Tinkham, and T. M. Klapwijk, *Phys. Rev. B* 25, 4515 (1982).
- [22] N. W. Ashcroft, and N. D. Mermin, *Introduction to Solid State Physics*, Edited by P. G. Crone, Holt-Saunders International (1981).
- [23] Y. Tanaka *et al.*, (private communication).

Chapter 7

Explanations for Variations and Anomalous Behaviors of Tunneling Spectra Measured on HTSC's

A great deal of tunneling experiments have been performed on the HTSC's, and various results have been reported so far [Ref. 1]. This variety of the spectrum data caused a confused situation in this field of study, and it continues even now. STM is thought to be an ideal probe to investigate this variety because it can change a measuring position and a barrier width, *i.e.*, it can make lots of junctions during one measurement. In fact, we observed so many types of spectra depending on the measuring condition, and found some tendencies. As discussed in Chapter 6, we revealed some types of spectra, which were considered as intrinsic properties of the HTSC's in the early period, to be extrinsic ones. However, even the spectra regarded as intrinsic ones have various shapes as described in Chapter 4 and Chapter 5. We presumed the condition of the tip and the sample surface for each spectrum, and interpreted some behavior. In this Chapter, we try to explain all the spectral results systematically.

Based on our spectrum data, and considering some band calculations [Refs. 2-7], ARPES studies [Refs. 8-11], and theoretical models [Refs. 12-19], we assume that, in HTSC's, the electronic structure varies in one-unit cell and each layer has a different property, which is assumed as follows:

[BSCCO]

- CuO₂: metallic and superconducting
- BiO : semiconducting with a band gap of ~ 0.1 eV (depending on the oxygen content)
- SrO : semiconducting with a band gap wider than that of the BiO layer
- Ca : insulating with a wide band gap

[YBCO]

- CuO₂: metallic and superconducting
- CuO : metallic but smaller density of states near the E_F than the CuO₂ layer, normal metallic or weakly superconducting due to a proximity effect
- BaO : semiconducting with a band gap of ~ 0.1 eV
- Y : insulating with a wide band gap

Normal density of states of each layer is expressed as $N_{\text{CuO}_2}(E)$, $N_{\text{BiO}}(E)$, $N_{\text{SrO}}(E)$, $N_{\text{Ca}}(E)$ for the

BSCCO system, and $N_{\text{CuO}_2}(E)$, $N_{\text{CuO}}(E)$, $N_{\text{BiO}}(E)$, $N_{\text{Y}}(E)$ for the YBCO system. Now, we assume that total density of states of each system consists of several components from the different layers, which is expressed as

$$\begin{aligned} \Psi_{L, \text{BSCCO}}(x)N_{\text{BSCCO}}(E, x) \\ = \Psi_{L, \text{CuO}_2}(x)N_{\text{CuO}_2}(E) + \Psi_{L, \text{BiO}}(x)N_{\text{BiO}}(E) + \Psi_{L, \text{SrO}}(x)N_{\text{SrO}}(E) + \Psi_{L, \text{Ca}}(x)N_{\text{Ca}}(E) \end{aligned} \quad (7.1)$$

$$\begin{aligned} \Psi_{L, \text{YBCO}}(x)N_{\text{YBCO}}(E, x) \\ = \Psi_{L, \text{CuO}_2}(x)N_{\text{CuO}_2}(E) + \Psi_{L, \text{CuO}}(x)N_{\text{CuO}}(E) + \Psi_{L, \text{BiO}}(x)N_{\text{BiO}}(E) + \Psi_{L, \text{Y}}(x)N_{\text{Y}}(E) \end{aligned} \quad (7.2)$$

where $\Psi_i(x)$ expresses a wave function. We assume that Ψ_i 's are independent of and have no interaction with each other. In order to take the spatial variation of the order parameter into account, we express a superconducting state

$$N_s(E, x) = S(E, \Delta(x))N_n(E, x) \quad (7.3)$$

by introducing a superconducting gap function $S(E, \Delta(x))$. Now we take note of the energy level V_1 (V_2) which is inside (outside) the band gap of the semiconducting layer (BiO, BaO) [and not so lower (higher) than the edge]. V_1 corresponds to the energy level outside the superconducting gap. Fig. 7.1 schematically indicates expected $\Psi_i(x)N(V_i, x)$ in the normal state, $\Psi_i(x)N(V_2, x)$, and $\Delta(x)$ for both the BSCCO system [Fig. 7.1(a)] and the YBCO system [Fig. 7.1(b)]. In the BSCCO system, at the energy of V_1 , only the CuO_2 layer has density of states and $\Psi_i(x)N(V_1, x)$ has its maximum at the positions of the CuO_2 layers. At the energy of V_2 , the BiO layer has finite density of states which is smaller than that of the CuO_2 layer. The SrO and Ca layers have no density of states both at V_1 and at V_2 . The superconducting order parameter $\Delta(x)$ has maximum on the CuO_2 layer and decays with the coherence length ξ_s of $\sim 1.2 \text{ \AA}$. On the other hand, in a YBCO, the CuO_2 layer and the CuO chain layer have density of states at $E = V_1$, and that of the CuO_2 layer is larger. At $E = V_2$, the BaO layer also has finite density of states which is smaller if compared to those of the CuO_2 and CuO chain layers. The order parameter $\Delta(x)$ becomes maximum at the CuO_2 layer and tails into the vicinity of the CuO chain layer, where $\Psi_i(x)N(E, x)$ has finite value.

Next, we discuss what a differential conductance curve reflects in the case that the electronic structure has the spatial variation as shown in Fig. 7.1. We start with Eq. 2.22 which appeared in the semi-phenomenological theory by Giaever and Megerle [Ref. 20] expressing the tunneling current between a superconductor and a normal metal.

$$I_m = \frac{2\pi e}{\hbar} |M|^2 N_n \int_{-\infty}^{\infty} N_s(E) [f(E) - f(E+V)] dE \quad (7.4)$$

where the density of states in the normal metal is constant N_n , the density of states in the

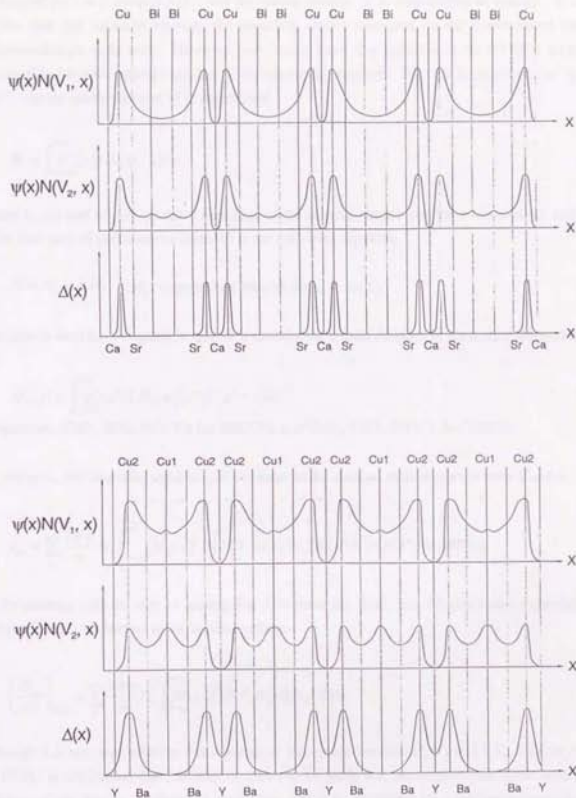


Fig. 7.1 Expected spatial variations of the electronic structure of (a) BSCCO and (b) YBCO. The oscillation of $\psi_4(x)$ is ignored in the diagrams.

superconductor $N_s(E)$ depends on energy, quasi-particles occupy a given state of energy E with a probability $f(E) = [1 + \exp(\beta E)]^{-1}$, and the matrix element M is independent of energy. It is well known that this equation explains the tunneling results measured on the conventional uniform superconductors quite well. However, we cannot apply this equation to the HTSC's which are assumed to have the spatial variation of the electronic structure. Eq. 7.4 is based on the "golden rule", and the matrix element M is determined

$$M = \int_{-\infty}^{\infty} \psi_s'(x) \lambda H_1 \psi_n(x) dx \quad (7.5)$$

where $\psi_s(x)$ and $\psi_n(x)$ are wave functions of the superconductor and the normal metal, and λH_1 is the first term of perturbation appeared in the following equation.

$$H = H_0 + \lambda H_1 \quad (H_0: \text{unperturbed Hamiltonian}, \lambda \ll 1) \quad (7.6)$$

One idea to treat the x -dependent system is introducing a delta function in the matrix element M .

$$M_L(x) = \int_{-\infty}^{\infty} \psi_s'(x') \lambda H_1 \psi_n(x') \delta(x' - x) dx' \quad (7.7)$$

L represents CuO_2 , BiO , SrO , Ca for BSCCO , and CuO_2 , CuO , BaO , Y for YBCO .

By doing so, the tunneling current I_m is obtained as the integral with respect to both E and x .

$$I_m = \sum_L \frac{2\pi e}{h} N_s \int_{-\infty}^{\infty} |M_L(x)|^2 \left\{ \int_{-\infty}^{\infty} S(E, \Delta(x)) N_L(E) [f(E) - f(E+V)] dE \right\} dx \quad (7.8)$$

By the analogy with the way of leading Eq. 2.24 from Eq. 2.22, Eq. 7.8 gives next expression by differentiating with respect to the applied voltage.

$$\left(\frac{dI_m}{dV} \right)_{V=0} = \sum_L \frac{2\pi e}{h} N_s \int_{-\infty}^{\infty} |M_L(x)|^2 S(V, \Delta(x)) N_L(V) dx \quad (7.9)$$

Although it is not clear whether this equation is true or not because $M_L(x)$ and $S(V, \Delta(x)) N_L(V)$ of the HTSC is not known here, at least, it seems to be likely that the conductance curve reflects the addition of the density of states of each layer which is multiplied by a prefactor expressing its weight which is determined by the wave functions and integrated with respect to the position. From this point of view, we will explain our various tunneling data qualitatively.

Figs. 7.2-7.4 schematically summarize our tunneling results. Figs. 7.2(a) and 7.2(b) demonstrate the expected tip positions and surface terminations of the specimens, which are

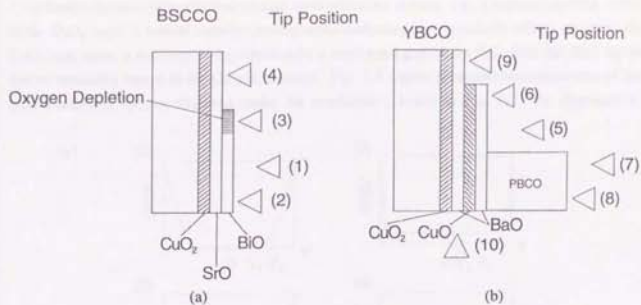


Fig. 7.2 Tip and sample surface conditions expected for each typical type of spectrum observed on (a) BSCCO [case (1)-(4)] and (b) YBCO [case (5)-(10)].

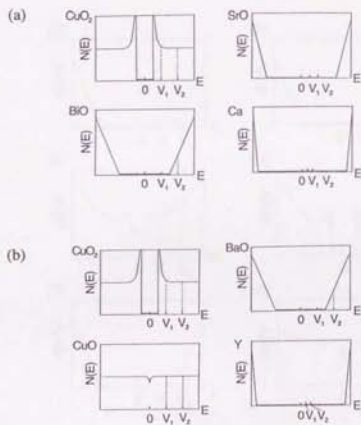


Fig. 7.3 Assumed electronic structures for each layer of (a) BSCCO and (b) YBCO.

presumed by considering the observed STM images and the values of set-point current and tip bias voltage and by comparing each result with others, as discussed in Chapter 4 and Chapter 5. Fig. 7.3 indicates the electronic structure of each layer which we assume, *i.e.*, a superconducting nature of the CuO_2 layer, a normal metallic (weakly superconducting by a proximity effect) nature of the CuO chain layer, a semiconducting nature with a small band gap of the BiO, SrO and BaO layers and an insulating nature of the Ca and Y layers. Fig. 7.4 shows schematic representations of the typical tunneling spectra observed under the conditions (1)-(10) in Fig. 7.2. As discussed in

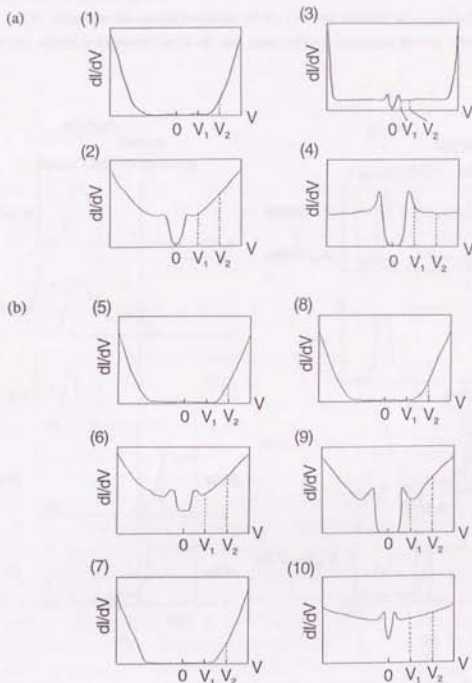


Fig. 7.4 Typical spectral shapes observed on (a) BSCCO single crystals and (b) YBCO thin films in our experiments. (1)-(10) correspond to the cases (1)-(10) described in Fig. 7.2.

section 5.6.2, the termination of a (001) oriented YBCO film is still controversial [Refs. 21-24]. However, here, we assume the BaO termination with the underlying CuO chain layer, which is consistent with the conclusion by Frank et al. [Ref. 22]. With this termination, the hole donor block of the BaO-CuO-BaO sequence is complete at the surface, which allows the first one-unit cell to become superconducting. Hence each layer near the surface can have the same electronic nature as in the bulk. Moreover, in this Chapter, we do not take into account the extrinsic effects discussed in section 4.6.2 and section 5.6.3, and explain the features of the observed spectra regarding them as intrinsic ones.

Fig. 7.5(a) illustrates the spatial variation of the electron density $\psi_{\pm, \text{BSCCO}}(x)N_{\text{BSCCO}}(E, x)$ near the surface, which is expected based on the assumptions described above, when the specimen is

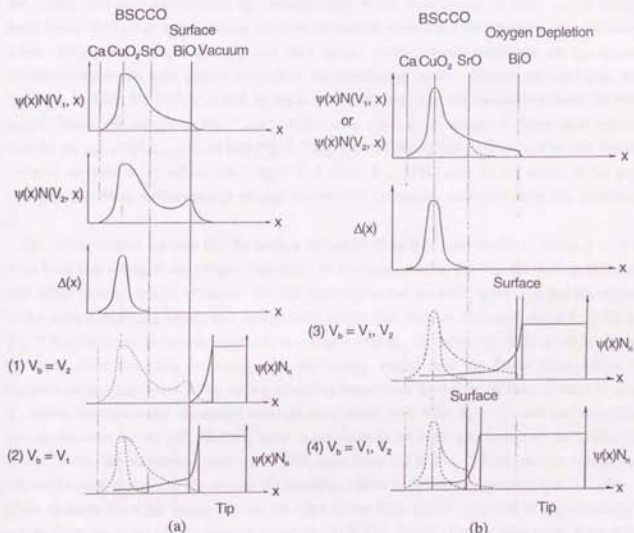


Fig. 7.5 Expected electronic feature near the surface for each type of spectrum observed on BSCCO single crystals. (a) BiO terminated surface. (b) Oxygen depleted BiO surface or SrO terminated surface.

terminated with the semiconducting BiO layer which has small band gap of -0.1 eV. At $E = V_1$, the Ca layer, the BiO layer and the SrO layer do not have density of states [$N_{Ca}(V_1) = N_{BiO}(V_1) = N_{SrO}(V_1) = 0$], and the $\psi_{E, BSCCO}(x)N_{BSCCO}(V_1, x)$ originating from the CuO_2 layer [$N_{CuO_2}(V_1) \neq 0$] decays gently through the BiO and SrO layers because the barrier height of this region is determined by the edge energy of the unoccupied conduction bands of the BiO and SrO layers which is much lower than the vacuum barrier. At $E = V_2$, the surface BiO layer has finite electron density which rapidly decays in the vacuum. The superconducting order parameter $\Delta(x)$ has maximum value Δ_0 at the CuO_2 layer, and decays abruptly with the coherence length ξ_c of $1-2 \text{ \AA}$. If the tip bias voltage $V_b = V_2$, the tip can detect the electronic states of the surface BiO layer, and tunneling process between the tip and the BiO layer mainly occurs. Therefore, the tip is kept away from the specimen, and the tunneling spectrum reflects only the electronic nature of the BiO layer. This corresponds to the case (1) in Fig. 7.2(a). On the other hand, when $V_b = V_1$, the tip cannot sense the surface BiO layer and the SrO layer because they do not have density of states at this energy level, hence the tip can approach very close to the sample surface and the tunneling into the CuO_2 states, which tails through the SrO and BiO layers, mainly occurs within the energy region corresponding to the band gap of the surface semiconducting layers. Outside the band gap, the tunneling between the BiO layer and the tip is overwhelming, thus the spectrum reflects the BiO states. This is the case (2) in Fig. 7.2(a). In this case, the $\Delta(x)$ is thought to decay more rapidly than the $\psi_{E, BSCCO}(x)N_{BSCCO}(V_1, x)$ [see Fig. 7.5(a)], thus the conductance curve must include lots of components with $\Delta(x)$ values satisfying $0 \leq \Delta(x) < \Delta_0$. This must be the origin of the gap smearing and finite conductance in the gap observed in the spectra measured under the condition (2).

Fig. 7.5(b) shows the case that the surface semiconducting BiO layer become insulating with a large band gap owing to the oxygen depletion. In this case, even at $E = V_2$, the surface BiO and SrO layers have no density of states. The electronic density of the CuO_2 layer tails into the region of the surface insulating layers, and decays more rapidly than the case discussed above [(1), (2) in Fig. 7.2(a)] because the barrier height of this region is higher. The behavior of the $\Delta(x)$ is almost the same since there are no changes in the energy region near the Fermi level where a superconducting gap opens. The surface insulating layers have no density of states at both V_1 and V_2 , hence the tip-sample separation becomes very small even with $V_b = V_2$, and the tunneling process between the tip and the CuO_2 layer is dominant in the band gap region of the insulating layers. When the terminating layer is the BiO layer [case (3) in Fig. 7.2(a)], the tip position is almost the same as the case (2), so that the smearing feature of the superconducting gap is similar. If we measure the wide energy region, the edge of the band gap is observed at higher energy, which yields the shape of the spectrum shown in (3) of Fig. 7.4(a). On the other hand, if the SrO layer appears on the surface [case (4) in Fig. 7.2(a)], the tip- CuO_2 distance becomes small, and the electronic density of the CuO_2 layer decays abruptly into the vacuum from the surface SrO layer. As a result of these differences, the conductance curve have less contributions of $\psi_{E, BSCCO}(x)N_{BSCCO}(E, x)$ from the positions where the $\Delta(x)$ is smaller than the Δ_0 or zero. This is

probably the reason why the tunneling spectra measured under this condition showed clear superconducting gap structures with flat bottoms and low conductance values at zero bias.

Fig. 7.6(a) represents the electronic features near the BaO terminated surface of YBCO. At $E = V_1$, the CuO_2 layer has more density of states than the CuO chain layer. The BaO layers work as low barriers and make the decrease of the CuO_2 and CuO electronic density in the BaO layer regions much gentler than in vacuum. At $E = V_2$, the BaO layer also has density of states which is small if compared to the CuO_2 and CuO chain layers. The $\Delta(x)$ decays from the CuO_2 layer with the coherence length ξ_s of $\sim 3 \text{ \AA}$ which is longer than that of BSCCO. This seems to have influence slightly on the CuO chain layer. When $V_b = V_2$ [case (5) in Fig. 7.2(b)], the tunneling between the tip and the surface BaO layer occurs because of the presence of the surface BaO states. If we adjust

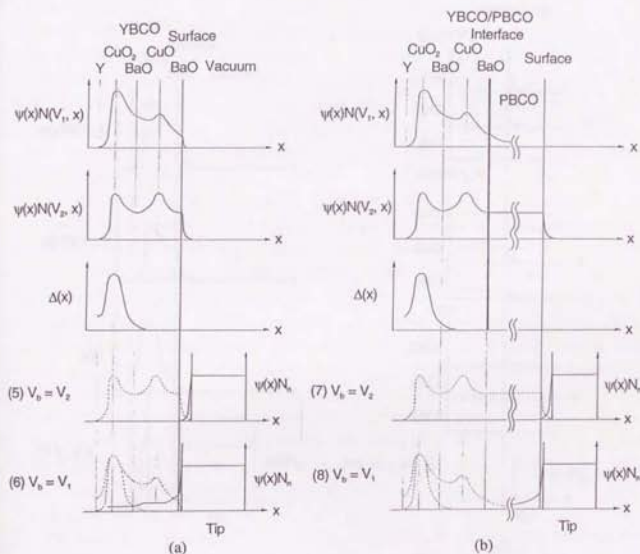


Fig. 7.6 Expected electronic feature near the surface for each type of spectrum observed on YBCO thin films. (a) BaO-CuO-terminated surface. (b) PBCO deposited surface.

V_b to V_1 , the tip is brought to the vicinity of the sample surface and the tunneling processes to both the CuO_2 and the CuO chain layers occur. Since the $\Delta(x)$ has the decay length of $\sim 3 \text{ \AA}$, the tunneling spectrum has contributions of $\psi_{k, \text{YBCO}}(x)N_{\text{YBCO}}(V_1, x)$ from the positions where $\Delta(x) = 0$. This normal component mainly from the CuO chain layer must yield the high zero-bias conductance observed in the spectra measured under the condition (6) in Fig. 7.2(b).

If we deposit 50 \AA PBCO on YBCO, the $\psi_{k, \text{YBCO}}(x)N_{\text{YBCO}}(V_1, x)$ and the $\Delta(x)$ cannot have finite values at the surface because the PBCO bulk itself is semiconducting with a band gap comparable to the BaO layer in YBCO [Fig. 7.6(b)]. At $E = V_2$, the PBCO has density of states, but $E = V_1$, the PBCO bulk has no density of states. Therefore, the tunneling spectrum shows a semiconducting feature irrespective of the tip-sample separation [(7), (8) in Fig. 7.2(b)].

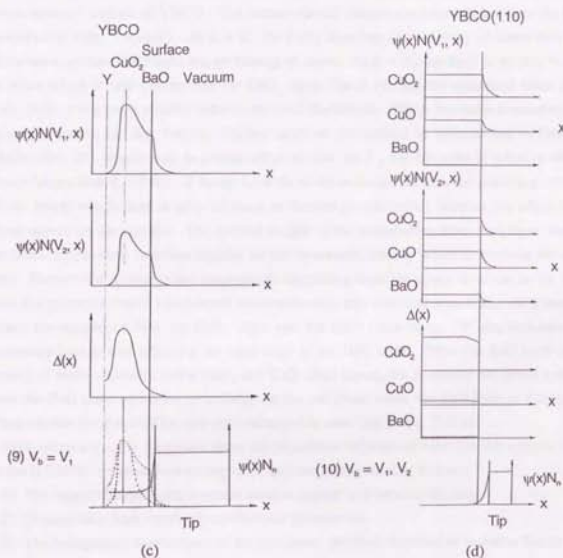


Fig. 7.6 Expected electronic feature near the surface for each type of spectrum observed on YBCO thin films. (c) BaO-CuO_2 -terminated surface. (d) Cross-sectional surface.

Fig. 7.6(c) demonstrates the variation of the electronic density of YBCO near the surface which is terminated with another BaO layer adjacent to the CuO_2 layer. At $E = V_1$, the CuO_2 layer has density of states and $\psi_{i, \text{YBCO}}(x)N_{\text{YBCO}}(V_1, x)$ decays in the BaO layer with a gentle slope because of the low barrier height in this region. At $E = V_2$, both the CuO_2 layer and the BaO layer have density of states, and the electronic density drops exponentially from the surface into the vacuum region. The $\Delta(x)$ shows the same tendency as shown in Fig. 7.6(a). When $V_b = V_1$, the tip-sample distance becomes very small, and only the tunneling process between the tip and the CuO_2 layer occurs because of the lack of the BaO states at this energy level [case (9) in Fig. 7.2(b)]. In this case, the tip- CuO_2 distance becomes short and the spectrum has a relatively large component of $\psi_{i, \text{YBCO}}(x)N_{\text{YBCO}}(V_1, x)$ from the positions where $\Delta(x) = \Delta_0$, which allow us to observe the clear superconducting gap structure with a flat bottom and very low conductance inside the gap.

Finally, Fig. 7.6(d) indicates the electronic features at the positions of the different layers on the cross-sectional surface of YBCO. The feature should change continuously between the layers as described in Figs. 7.6(a)-(c). At $E = V_1$, the CuO_2 layer has more density of states than the CuO chain layer, and the BaO layer has no density of states. At $E = V_2$, the BaO layer also has density of states which is still smaller than the CuO_2 layer. The $\Delta(x)$ has the maximum value Δ_0 at the CuO_2 layer and a much smaller value at the CuO chain layer. The $\Delta(x)$ value is constant on each layer ($x = \text{const.}$) and may become slightly small at the surface as pointed out by Deutcher and Müller [Ref. 25], which must be a weak effect because the ξ_{ab} has the order of a few or several nm (much longer than $\xi_c \sim 3 \text{ \AA}$). If the tip is on the cross-sectional surface, the tunneling processes to all the layers which have density of states at the energy can occur, because the edges of all the layers appear on the surface. The spectral weight of the contribution from each layer depends on the lateral tip position, and also slightly on the tip-sample distance which determines the tunneling area. Because the spectrum has components originating from the layers involved in the tunneling area, the spectrum shows a broadened superconducting gap with high zero-bias conductance which reflect the natures of both the CuO_2 layer and the CuO chain layer. It also indicates slightly increasing background reflecting the band edge of the BaO layer. Since the BaO layer has small density of states relatively to the CuO_2 and CuO chain layers, the spectrum has small contribution from the BaO layer which becomes large on the a - b plane when the BaO layer is the top layer. These explain the shape of the spectrum measured in case (10) in Fig. 7.2(b).

Now we return to the discussion about the anomalous behavior of the tunneling spectra measured on the HTSC's. As described in chapter 1, they are summarized as follows:

- 1) The superconducting gap structure tends to appear in a broadening shape.
- 2) Considerably high inner-gap conductance is observed.
- 3) The background conductance of the spectrum, which is expected to be rather flat in the case of normal metal, often shows linear feature.
- 4) Unexpected dip structure appears just outside the peak of the superconducting gap structure, which is enhanced in the occupied states.

In the case of macroscopic junction methods, the gap broadening can be caused by the technical

problem, e.g., unsuitable high tunneling resistance, and by extrinsic effects such as inhomogeneity of the crystal, oxygen depletion and chemical reaction as discussed in section 4.6.2. However, even the tunneling data measured by STM which is thought to be free from these problems because of vacuum tunneling and its small area of an atomic scale also show considerable smearing of the gap structure [Refs. 26 -29]. The broadening feature of the spectra measured by STM can be explained in terms of the gap anisotropy. However, if the HTSC's have anisotropic *s*-wave symmetry of the Cooper pair, the spectrum should always show a flat bottom, and if they have *d*-wave symmetry, the spectrum should always show a gapless feature. The fact observed is that sometimes the spectrum shows a finite gap with a flat bottom, and, in most cases, it shows a gapless feature. We would like to point out the possibility that if the electronic structure varies in the real space, as discussed above, it can cause the gap broadening. If this is the case, a finite gap can be observed only when the tip-CuO₂ distance is small and the contribution of $\psi_i(x)N(E, x)$ from the positions where $\Delta(x) = \Delta_0$ is relatively large. However, the terminating layer is thought to be the BiO layer of BiO-SrO-CuO₂- sequence for BSCCO, and the BaO layer of BaO-CuO-BaO-CuO₂- sequence for YBCO in most cases. This must be the reason why most of the spectra show the gap broadening and it is very rare that a finite gap is observed.

It has been reported that superconducting gap structure in the spectrum measured on the HTSC shows considerably high conductance inside the gap. The number of the reports of this feature decreased as the technique of tunneling experiments and the quality of junctions were improved by understanding the unstable and fragile features of HTSC materials. However, this feature is still observed remarkably on the YBCO system, which has been often attributed to the unstable surface of this system and a normal region formed by degradation. In our case, the surfaces of the specimens are thought to be not degraded because the atomic images can be obtained on them. On BSCCO, the superconducting spectrum showed zero-bias conductance as low as ~5 % of the normal background, if the energy resolution was high enough, which was actually not zero. On YBCO, most of the superconducting spectra indicated pretty high zero-bias conductance values which were 50 % or higher of the normal ones. However, some of the spectra showed very low zero-bias conductance values of ~1 %. This residual conductance can be also explained by assuming the spatial variation of the electronic structure and a normal metallic nature of the CuO chain layer. The coherence length along the *c*-axis ξ_c of the HTSC is extremely short. Therefore the tunneling spectrum measured on the HTSC cannot help having contributions of $\psi_i(x)N(E, x)$ from the positions where $\Delta(x) = 0$, which is relatively large when the tip-CuO₂ separation is large as discussed above. Furthermore, in the case of YBCO, the normal metallic CuO layers where $\Delta(x) \cong 0$ give additional contributions. This is considered as the reason why only YBCO tends to indicate extremely high zero-bias conductance, because the CuO chain layer exists only in the YBCO system.

The linear background has also been reported as a key feature of the HTSC. It has been discussed in some new theories such as the RVB model [Ref. 30] and the marginal Fermi liquid model [Ref. 31] connected with the mechanism of the high temperature superconductivity.

However, the data of ARPES studies [Refs. 8-11, 32-44] did not show this feature, and some of the tunneling data measured by STM also showed flat background even when the data seemed to be reliable because atomic resolution was obtained so that the STM was thought to be operated under an ideal condition. Actually, in our results, the tunneling spectrum, which is thought to reflect only the nature of the CuO_2 layer around the E_F [(3), (4) in Figs. 7.2(a), 7.4(a)], showed a typical superconducting gap structure and a flat background. Considering these facts, it is most likely that this linear background is not the nature of the CuO_2 band but the increasing background which appeared in the spectra classified in (2), (6), (9) shown in Figs. 7.2 and 7.4, namely the band edge of the semiconducting layer such as the BiO , SrO and BaO layers. Since absolute value of the density of states at the band edge is much smaller than that of the CuO_2 layer around the E_F , this feature cannot be observed by PES, and in the case of the tunneling experiment, this feature is remarkable when the top layer is one of the semiconducting layers. As discussed above, the BiO termination for BSCCO and the BaO termination for YBCO are the most likely cases. Therefore a planar junction tends to show this linear background because it has a wide junction area, and most part of the interface is terminated with the semiconducting layer. On the contrary, flat background is observed in a break junction and a point contact which can break this surface semiconducting layer and detect the nature of the CuO_2 layer, and in STS which reflects the nature of a local area where the band gap becomes larger and only the nature of the CuO_2 band is observed around the E_F .

The problem which still remains is the diplike structure outside the pileup peak of superconducting gap structure observed on the BSCCO system. Even the spectra which are considered to reflect only the nature of the CuO_2 layer [(2), (4) in Fig. 7.2] show this feature. This suggests that this structure is originating from the CuO_2 band. In order to explain this diplike feature in the tunneling spectrum, it seems to be attractive to assume that the CuO_2 band has a strongly energy dependent asymmetric $N_g(E)$ with a heap near the E_F , and the spectrum is a convolution of the usual parabolic tunneling conductance and this $N_g(E)$ as proposed by Huang *et al.* [Ref. 49] (see section 4.5). However, this cannot explain the same feature appeared in the PES spectra [Refs. 8, 10, 11, 39-44]. There are several explanations for this structure from other points of view. The simplest explanation for this effect is that there are two bands in close proximity to each other and by coincidence they superimpose to form one feature in the normal state. As the temperature is lowered, one or both of these bands sharpen up due to reduced lifetime broadening owing to decreased electron-electron scattering in the superconducting state, and the dip appears between them. Arnold *et al.* think that the dip may be related to the high-energy (relative to the pileup peak of the superconducting gap structure) oscillations observed in the tunneling spectra of strong-coupling superconductors [Ref. 46]. Anderson wrote that due to the hopping matrix element connecting the two close CuO_2 layers in BSCCO, there is a doubling of the calculated energy bands at general points in the 2D zone with a splitting of the order of 0.1 eV. The fact that this splitting has not been observed above T_c is, he speculated, strong support for the two-dimensionally correlated non-Fermi-liquid theory of the normal state. In the superconducting

state, the quasiparticle fermionlike nature of the electronic excitations is partially restored and the 3D band structure reappears. As a result, the splitting band is observed as the diplike feature [Ref. 30]. The phenomenological marginal Fermi liquid theory shows two peaks (one at Δ and one at 3Δ) in the calculated spectral weight function of the superconducting state, and thus the dip can be interpreted as a valley between these two peaks [Ref. 31]. At the present moment, it is not clear which model is true. We would like to suggest that, at least, this diplike feature seems to be originating from the CuO_2 band, which then may be intrinsic for the high temperature superconductivity.

As discussed in this Chapter, the variation and some of the anomalous behaviors of the tunneling spectra observed on the HTSC's can be explained by assuming the position-dependent electronic structure of this system, which is suggested by some theoretical [Refs. 12-19] and experimental results [Refs. 47-51]. If this assumption is true, it must be intrinsically very difficult to observe a finite gap even if a superconducting gap completely opens up in the CuO_2 band, *i.e.*, *s*-wave symmetry of the Cooper pair. Furthermore, there are lots of extrinsic effects which cause gap broadening. Therefore we would like to point out that it is meaningless to conclude, from tunneling experiments, the existence of a node in the gap symmetry based on the spectrum data showing gapless features.

References

- [1] See T. Hasegawa, H. Ikuta, and K. Kitazawa, *Physical Properties of High Temperature Superconductors III*, edited by D. M. Ginsberg, World Scientific Publishing, 525 (1992).
- [2] S. Massidda, J. Yu, and A. J. Freeman, *Physica C* 152, 251 (1988).
- [3] M. S. Hybertsen, and L. F. Mattheiss, *Phys. Rev. Lett.* 60, 1661 (1988).
- [4] H. Krakauer, and W. E. Pickett, *Phys. Rev. Lett.* 60, 1665 (1988).
- [5] S. Massidda, J. Yu, A. J. Freeman, and D. D. Koelling, *Phys. Lett. A* 122, 198 (1987).
- [6] J. Yu, S. Massidda, A. J. Freeman, and D. D. Koelling, *Phys. Lett. A* 122, 203 (1987).
- [7] L. F. Mattheiss, and D. R. Hamann, *Solid State Commun.* 63, 395 (1987).
- [8] Z.-X. Shen, D. S. Dessau, B. O. Wells, D. M. King, W. E. Spicer, A. J. Arko, D. Marshall, L. W. Lombardo, A. Kapitulnik, P. Dickinson, S. Doniach, J. DiCarlo, A. G. Loeser, and C.-H. Park, *Phys. Rev. Lett.* 70, 1553 (1993).
- [9] D. S. Dessau, Z.-X. Shen, D. M. King, D. S. Marshall, L. W. Lombardo, P. H. Dickinson, A. G. Loeser, J. DiCarlo, C.-H. Park, A. Kapitulnik, and W. E. Spicer, *Phys. Rev. Lett.* 71, 2781 (1993).
- [10] J. Ma, C. Quitmann, R. J. Kelley, H. Berger, G. Margaritondo, and M. Onellion, submitted to *Phys. Rev. Lett.*
- [11] H. Ding, J. C. Campuzano, A. F. Bellman, T. Yokoya, M. R. Norman, M. Randeria, T. Takahashi, H. Katayama-Yoshida, T. Mochiku, K. Kadowaki, and G. Jennings, submitted to *Phys. Rev. Lett.*

- [12] M. Tachiki, and S. Takahashi, *Solid State Comm.* 70, 291 (1989).
- [13] M. Tachiki, S. Takahashi, F. Steglich, and H. Adrian, *Z. Phys. B* 80, 161 (1990).
- [14] L. N. Bulaevskii, and M. V. Zyskin, *Phys. Rev. B* 42, 10230 (1990).
- [15] A. A. Abrikosov, *Physica C* 182, 191 (1991).
- [16] S. H. Liu, and R. A. Klemm, *Phys. Rev. B* 48, 4080 (1993).
- [17] S. H. Liu, and R. A. Klemm, *Phys. Rev. B* 48, 10650 (1993).
- [18] S. H. Liu, and R. A. Klemm, *Physica C* 216, 293 (1993).
- [19] S. H. Liu, and R. A. Klemm, *Phys. Rev. Lett.* 73, 1019 (1994).
- [20] I. Giaever, and K. Megerle, *Phys. Rev.* 122, 1101 (1961).
- [21] M. A. Harmer, C. R. Fincher, and B. A. Parkinson, *J. Appl. Phys.* 70, 2760 (1991).
- [22] G. Frank, Ch. Ziegler, and W. Gopel, *Phys. Rev. B* 43, 2828 (1991).
- [23] T. Terashima, K. Shimura, Y. Daitoh, Y. Yano, Y. Matsuda, S. Komiyama, and Y. Bando, *Proc. of MRS Spring Meeting, San Francisco, 1992.*
- [24] S. J. Pennycook, M. F. Chisholm, D. E. Jesson, D. P. Norton, D. H. Lowndes, R. Feenstra, H. R. Kerchner, and J. O. Thomson, *Phys. Rev. Lett.* 67, 765 (1991).
- [25] G. Deutscher, and K. A. Müller, *Phys. Rev. Lett.* 59, 1745 (1987).
- [26] J.-X. Liu, J.-C. Wan, and A. M. Goldman, *Phys. Rev. Lett.* 67, 2195 (1991).
- [27] C. Renner, Ø. Fischer, A. D. Kent, D. B. Mitzi, and A. Kapitulnik, *Physica B* 194-196, 1689 (1994).
- [28] E. J. G. Boom, A. J. A. van Roy, and H. van Kempen, to be published in *Physica C*.
- [29] C. Manabe, M. Oda, and M. Ido, to be published in *Physica C*.
- [30] P. W. Anderson, *Phys. Rev. Lett.* 67, 660 (1991).
- [31] C. M. Varma, P. B. Littlewood, S. Schmitt-Rink, E. Abrahams, and A. E. Ruckenstein, *Phys. Rev. Lett.* 63, 1996 (1989).
- [32] T. Takahashi, H. Matsuyama, H. Katayama-Yoshida, Y. Okabe, S. Hosoya, K. Seki, H. Fujimoto, M. Sato, and H. Inokuchi, *Nature* 334, 691 (1988).
- [33] C. G. Olson, R. Liu, A.-B. Yang, D. W. Lynch, A. J. Arko, R. S. List, D. W. Veal, Y. C. Chang, P. Z. Jiang, and A. P. Paulikas, *Science* 245, 731 (1989).
- [34] C. G. Olson, R. Liu, D. W. Lynch, R. S. List, A. J. Arko, D. W. Veal, Y. C. Chang, P. Z. Jiang, and A. P. Paulikas, *Solid State Commun.* 76, 411 (1990).
- [35] C. G. Olson, R. Liu, D. W. Lynch, R. S. List, A. J. Arko, D. W. Veal, Y. C. Chang, P. Z. Jiang, and A. P. Paulikas, *Phys. Rev. B* 42, 381 (1990).
- [36] R. Manzke, T. Buslaps, R. Claessen, and J. Fink, *Europhys. Lett.* 9, 477 (1989).
- [37] J.-M. Imer, F. Patthey, B. Dardel, W.-D. Schneider, Y. Baer, Y. Petroff, and A. Zettl, *Phys. Rev. Lett.* 62, 336 (1989).
- [38] Y. Chang, M. Tang, R. Zanon, M. Onellion, R. Joynt, D. L. Huber, G. Margaritondo, P. A. Morris, W. A. Bonner, J. M. Tarascon, and N. G. Stoffel, *Phys. Rev. B* 39, 4740 (1989).
- [39] B. O. Wells, Z.-X. Shen, D. S. Dessau, W. E. Spicer, C. G. Olson, D. B. Mitzi, A. Kapitulnik, R. S. List, and A. Arko, *Phys. Rev. Lett.* 65, 3056 (1990).

- [40] D. S. Dessau, B. O. Wells, Z.-X. Shen, W. E. Spicer, A. J. Arko, R. S. List, D. B. Mitzi, and A. Kapitulnik, *Phys. Rev. Lett.* **66**, 2160 (1991).
- [41] Y. Hwu, L. Lozzi, M. Marsi, S. La Rosa, M. Winokur, P. Davis, M. Onellion, H. Berger, F. Gozzo, F. Lévy, and G. Margaritondo, *Phys. Rev. Lett.* **67**, 2573 (1991).
- [42] D. S. Dessau, Z.-X. Shen, B. O. Wells, D. M. King, W. E. Spicer, A. J. Arko, L. W. Lombardo, D. B. Mitzi, and A. Kapitulnik, *Phys. Rev. B* **45**, 5095 (1992).
- [43] R. J. Kelley, J. Ma, G. Margaritondo, M. Onellion, *Phys. Rev. Lett.* **71**, 4051 (1993).
- [44] B. O. Wells, Z.-X. Shen, D. S. Dessau, W. E. Spicer, D. B. Mitzi, L. Lombardo, A. Kapitulnik, and A. J. Arko, *Phys. Rev. B* **46**, 11830 (1992).
- [45] Q. Huang, J. F. Zasadzinski, K. E. Gray, J. Z. Liu, and H. Claus, *Phys. Rev. B* **40**, 9366 (1989).
- [46] G. B. Arnold, F. M. Mueller, and J. C. Swihart, *Phys. Rev. Lett.* **67**, 2569 (1991).
- [47] Y. Iye, S. Nakamura, and T. Tamegai, *Physica C* **159**, 433 (1989).
- [48] Y. Iye, *Rev. Sci. Instrum.* **52**, 736 (1991).
- [49] Y. Iye, A. Fukushima, T. Tamegai, T. Terashima, and Y. Bando, *Physica C* **185-189**, 297 (1991).
- [50] S. N. Artemenko, and A. N. Kruglov, *Phys. Lett. A* **143**, 485 (1990).
- [51] R. Kleiner, F. Steinmeyer, G. Kunkel, and P. Müller, *Phys. Rev. Lett.* **68**, 2394 (1992).

Chapter 8

General Conclusions

We have designed and built a cryogenic STM which allow atomic resolution STM/STS and AST observations in the wide temperature range from room temperature to 4.2 K with enough stability. The apparatus has a vibration isolation system and an airtight structure which allows sample setting procedure without exposure to ambient atmosphere. This cryogenic STM apparatus has revealed capability of observing the HTSC's in a superconducting state.

STM observations were performed at 4.2 K on 1) the cleaved *a-b* planes of BSCCO single crystals, 2) the as-grown *a-b* planes of (001) oriented YBCO thin films, and 3) the as-grown (110) planes of (110) oriented YBCO thin films, and atomic resolution was achieved on all of them. The images revealed atomic arrangements corresponding to 1) Bi atoms of the surface BiO layer, 2) cation atoms (Cu, Ba, Y) or oxygen atoms of the BaO layer, and 3) Cu atoms of the CuO₂ and CuO layers, respectively. These results indicate that the STM was operated under an ideal condition, and the specimens kept appropriateness for STM observations without severe contamination or chemical reaction.

We performed tunneling spectroscopic measurements on the three kinds of specimens. Most of the measurements were accompanied with atomic resolution images, which secured that the obtained tunneling spectrum data were measured under the ideal condition and have reliability if compared to the earlier works in which STM was used as a tool of a point contact method. The observed features of the spectra can be roughly classified into two types: one is semiconducting or insulating, and the other is metallic and superconducting. Some of the spectra appeared as combinations of these two features. The spectrum varied its shape depending on the temperature, the oxygen content of the specimen, the tunneling barrier width, and the measuring position on the cross-sectional surface. Sometimes, different shapes of spectra were obtained under the same measuring condition, which can be attributed to the difference of the surface termination of the specimen. Not all but some of the superconducting spectra showed a clear gap structure with a flat bottom strongly suggesting that a finite gap opens up over the Fermi surface, *i.e.*, *s*-wave symmetry of the Cooper pair. All these behavior and variation of the tunneling spectra can be explained if we assume that, in the HTSC's, different layers possess different electronic structures, and the wave function, the density of states and the superconducting order parameter have spatial variations even in the one unit cell, and the tunneling spectrum has more than two components contributed from the different layers. This assumption is tolerably credible considering the crystallographic structure of the HTSC materials, their strong two dimensional features, their extremely short coherence lengths along the *c*-axis, and some calculational and experimental results

suggesting the intrinsic pinning or the interlayer Josephson coupling. This assumption also can account for the abnormal features observed in the tunneling spectra, which are not expected from the BCS theory.

This study has made it clear that, at least in the region near the surface of the HTSC, the electronic structure has spatial variation with an Å or nm scale, which seems to be caused intrinsically by the different electronic structures of different layers, and extrinsically by the spatial change of the oxygen concentration or by the substitution atoms. This fact is enough to say that since the macroscopic methods of tunneling spectroscopy give the information integrated over a wide junction area, we cannot derive the real low energy excitation spectrum reflecting an intrinsic nature of the high temperature superconductivity from the data obtained by these conventional methods. The possible origins of the spatial variation of the electronic structure observed in the surface region can be applied to the bulk feature, although whether or not it occurs in the bulk is not clear at the present moment. However, if it happens, it is dangerous to derive some conclusions from the data obtained by macroscopic measurements which were successfully applied to conventional uniform superconductors, and we have to consider once more the experimental results measuring the size of the superconducting gap or its temperature dependence with macroscopic probes, *i.e.*, NMR, ARPES, macroscopic tunneling measurements, the penetration depth (λ), which often conclude the *d*-wave superconductivity of the HTSC materials. NMR can detect the signal originating from one specified site such as the Cu site and the O site. In this sense, NMR is a microscopic probe. However, if the specimen has the spatial variation of the superconducting order parameter in the bulk, which seems to be caused mainly by the change of the local oxygen concentration, there are strong superconducting areas with large Δ 's and high T_c 's and weak or non-superconducting areas with small or zero Δ 's and low T_c 's in one specimen. Since the NMR signal reflects the natures of both areas, this must have influence on the $1/T_1$ - T curve ($1/T_1$: the spin-lattice relaxation rate). Some models which consists of alternating superconducting and normal layers coupled by a proximity effect, propose possible *s*-wave explanations for the ARPES and tunneling experiments based on the possible presence of electronic surface states whose spectral weight vanishes in the Γ - X and Γ - Y directions. They also obtained quantitative fits with the linear behavior of the $\lambda_{ab}(T)$ in the temperature $T \ll T_c$.

As discussed above, the data of the HTSC seem to be complicated intrinsically by the spatial variation of the electronic structure arising from the complex layered structure of this system and extrinsically by the oxygen nonstoichiometry which is changeable especially at the surface. In order to obtain intrinsic information, we should measure the specimen of well-controlled oxygen content by using a microscopic probe under the condition which does not cause the oxygen depletion, otherwise we have to analyze macroscopic data taking these factors into account. Although STM is a promising microscopic probe to investigate the electronic nature of the HTSC, decisive results have never been obtained. The key seems to be concealed in the technique of getting and keeping a clean surface of the specimen at low temperature enough to avoid the depletion of the surface oxygen.

List of Publications

Original Papers

- [1] "Atomic Resolution STM/STS on Oxide Superconductors down to 4.2 K", T. Hasegawa, M. Nantoh, H. Suzuki, N. Motohira, K. Kishio, and K. Kitazawa, *Physica B* 165&166, 1563 (1990).
- [2] "Cryogenic Scanning Tunneling Microscopy and Spectroscopy on the Cleaved Surface of Bi-Sr-Ca-Cu-O down to 4.2 K", T. Hasegawa, M. Nantoh, and K. Kitazawa, *Jpn. J. Appl. Phys.* 30, L276 (1991).
- [3] "STM/STS Study of Single Crystalline $\text{Bi}_2\text{Sr}_2\text{CaCu}_2\text{O}_7$ (1) : Superconducting Gap and Barrier Width Dependence of Tunneling Spectrum", M. Nantoh, S. Heike, H. Ikuta, T. Hasegawa, and K. Kitazawa, *Physica C* 185-189, 861 (1991).
- [4] "STM/STS Study of Single Crystalline $\text{Bi}_2\text{Sr}_2\text{CaCu}_2\text{O}_7$ (2) : Electronic Nature of BiO Layer as a Function of Oxygen Content", W. Wei, M. Nantoh, H. Ikuta, T. Hasegawa, and K. Kitazawa, *Physica C* 185-189, 863 (1991).
- [5] "Cryogenic Scanning Tunneling Spectroscopy on Oxide Superconductors", T. Hasegawa, M. Nantoh, H. Ikuta, and K. Kitazawa, *Physica C* 185-189, 1743 (1991).
- [6] "Anisotropic Electronic Structures in Cuprate Superconductors Investigated by STM/STS", T. Hasegawa, M. Nantoh, N. Motohira, K. Kishio, and K. Kitazawa, *Supercond. Sci. Technol.* 4, S73 (1991).
- [7] "Anisotropic Electronic Structures of High T_c Superconductors Investigated by STM/STS", T. Hasegawa, H. Ikuta, M. Nantoh, and K. Kitazawa, *Proceedings of the 1992 TcSUH HTS Workshop on Materials, Bulk Processing and Applications*, Houston, U.S.A., February 1992.
- [8] "Atom-Site Specified Tunneling Spectroscopy on $\text{Bi}_2\text{Sr}_2\text{CaCu}_2\text{O}_7$, $\text{YBa}_2\text{Cu}_3\text{O}_7$ and $\text{TaS}_2\text{-TaSe}_2$ ", M. Nantoh, W. Yamaguchi, A. Takagi, H. Ikuta, T. Hasegawa, and K. Kitazawa, *Proceedings of the Beijing International Conference on High Temperature Superconductivity (BHTSC'92)*, Beijing, China, May 1992.
- [9] "Atomic Site Tunneling Spectroscopy on Oxide Superconductors", T. Hasegawa, M. Nantoh, A. Takagi, H. Ikuta, M. Kawasaki, H. Koinuma, and K. Kitazawa, *J. Phys. Chem. Solids* 53, 1643 (1992).
- [10] "High Quality $\text{YBa}_2\text{Cu}_3\text{O}_7$ Thin Films Prepared by Pulsed Laser Deposition", J. P. Gong, M. Kawasaki, K. Fujito, M. Nantoh, T. Hasegawa, K. Hirai, K. Horiguchi, M. Yoshimoto, and H. Koinuma, *Proceedings of the Third China-Japan Symposium on Thin Films*, Huangshan, China, September 1992.
- [11] "Preparation and Nanoscale Characterization of Highly Stable $\text{YBa}_2\text{Cu}_3\text{O}_7$ Thin Films", M.

- Kawasaki, J. P. Gong, M. Nantoh, T. Hasegawa, K. Kitazawa, M. Kumagai, K. Hirai, K. Horiguchi, M. Yoshimoto, and H. Koinuma, *Jpn. J. Appl. Phys.* 32, 1612 (1993).
- [12] "Superconducting Gap Observed by the Atomic-Site Tunneling Spectroscopy in YBCO and BSCCO", K. Kitazawa, M. Nantoh, S. Heike, A. Takagi, H. Ikuta, and T. Hasegawa, *Physica C* 209, 23 (1993).
- [13] "Low Temperature STM and Atomic Site Tunneling (AST) on High Temperature Superconductors", M. Nantoh, T. Hasegawa, A. Takagi, H. Ikuta, K. Kitazawa, M. Kawasaki, J. P. Gong, and H. Koinuma, Proceedings of the 6th Int'l Symposium on Superconductivity (ISS'93), Hakodate, Japan, June 1993.
- [14] "STM and Tunneling Spectroscopy of Thin Films with Very Stable Surface", M. Kawasaki, J. P. Gong, K. Fujito, M. Nantoh, T. Hasegawa, K. Kitazawa, and H. Koinuma, Proceedings of the 6th Int'l Symposium on Superconductivity (ISS'93), Hakodate, Japan, June 1993.
- [15] "Cryogenic STM/STS of YBCO Thin Films and Its Significance for SIS Tunnel Junction", M. Kawasaki, J. P. Gong, K. Fujito, M. Nantoh, T. Hasegawa, K. Kitazawa, and H. Koinuma, Proceedings of ISEC'93, Boulder, U.S.A., August 1993.
- [16] "Scanning Tunneling Spectroscopy on High T_c Superconductors", T. Hasegawa, M. Nantoh, S. Heike, A. Takagi, M. Ogino, M. Kawasaki, H. Koinuma, and K. Kitazawa, *J. Phys. Chem. Solids* 54, 1351 (1993).
- [17] "Surface and Interface Characterization of High T_c Related Epitaxial Films by STM/STS and XPS", H. Koinuma, S. Gonda, J. P. Gong, M. Kawasaki, M. Yoshimoto, M. Nantoh, T. Hasegawa, and K. Kitazawa, *J. Phys. Chem. Solids* 54, 1215 (1993).
- [18] "Scanning Tunneling Spectroscopy on High T_c Superconductors", T. Hasegawa, M. Nantoh, S. Heike, A. Takagi, H. Ikuta, M. Kawasaki, H. Koinuma, and K. Kitazawa, *Physica Scripta* T49, 215 (1993).
- [19] "Atomic Site Tunneling Spectroscopy on High T_c Superconductors", T. Hasegawa, M. Nantoh, A. Takagi, W. Yamaguchi, M. Ogino, M. Kawasaki, J. P. Gong, H. Koinuma, and K. Kitazawa, *Physica B* 197, 617 (1994).
- [20] "Cryogenic Scanning Tunneling Microscopy / Spectroscopy on the (001) Surfaces of $\text{YBa}_2\text{Cu}_3\text{O}_7$ Epitaxial Thin Films", M. Nantoh, T. Hasegawa, W. Yamaguchi, A. Takagi, M. Ogino, M. Kawasaki, J. P. Gong, H. Koinuma, and K. Kitazawa, *J. Appl. Phys.* 75, 5227 (1994).
- [21] "Cryogenic STM/STS Observation on Oxide Superconductors", M. Nantoh, T. Hasegawa, M. Kawasaki, J. P. Gong, K. Fujito, A. Takagi, W. Yamaguchi, M. Ogino, H. Koinuma, and K. Kitazawa, *J. Superconductivity* 7, 349 (1994).
- [22] "Crystal Growth and Atomic-Level Characterization of $\text{YBa}_2\text{Cu}_3\text{O}_7$ Epitaxial Films", M. Kawasaki, and M. Nantoh, *MRS Bulletin* XIX (9), 33 (1994).
- [23] "Scanning Tunneling Microscopy / Spectroscopy on the (110) Surfaces of $\text{YBa}_2\text{Cu}_3\text{O}_7$ Thin Films", M. Nantoh, T. Hasegawa, W. Yamaguchi, A. Takagi, M. Ogino, M. Kawasaki, K.

- Fujito, H. Koinuma, and K. Kitazawa, *Physica C* 235-240, 1857 (1994).
- [24] "Cryogenic Scanning Tunneling Microscopy / Spectroscopy on the (110) Surfaces of $\text{YBa}_2\text{Cu}_3\text{O}_x$ Epitaxial Thin Films", M. Nantoh, M. Kawasaki, T. Hasegawa, K. Fujito, W. Yamaguchi, H. Koinuma, and K. Kitazawa, *Physica C* 242, 277 (1995).
- [25] "STM Tunneling Spectroscopy on High T_c Superconductors", T. Hasegawa, M. Nantoh, M. Ogino, H. Sugawara, M. Kawasaki, H. Koinuma, and K. Kitazawa, to be published in *J. Superconductivity*.

Original Papers in Japanese

- [26] "Low-Temperature STM Observations of Oxide Superconductors", T. Hasegawa, M. Nantoh, and K. Kitazawa, *Oyo Buturi* 59, 1642 (1990).
- [27] "Tunneling Spectroscopy on Oxide Superconductors - Recent Experiments Including STM Study -", T. Hasegawa, M. Nantoh, and H. Ikuta, *Solid State Physics* 26, 425 (1991).
- [28] "Electronic Structure and Superconducting State of High Temperature Oxide Superconductor", M. Nantoh, T. Hasegawa, and K. Kitazawa, *Journal of the Crystallographic Society of Japan* 35, 123 (1993).
- [29] "STM/STS Technique", T. Hasegawa, and M. Nantoh, *Oyo Buturi* 63, 402 (1994).

Reviews

- [30] "Atomic Resolution Scanning Tunneling Microscopy and Spectroscopy on the Cleaved Basal Plane of Bi-Sr-Ca-Cu-O down to 4.2 K", K. Kitazawa, T. Hasegawa, and M. Nantoh, *Research Report on Mechanism of Superconductivity I*, Science Research on Priority Areas No.031, Ministry of Education, Science and Culture, 287 (1991).
- [31] "Atom-Site Specified Tunneling Spectroscopy on Oxide Superconductors and Charge Density Wave Materials", K. Kitazawa, T. Hasegawa, H. Ikuta, M. Nantoh, and W. Wei, *Low Dimensional Properties of Solids* (Proceedings of Nobel Symposium, Gothenburg, Sweden, December 1991), *Physica Scripta*, 89 (1992).
- [32] "Anisotropy of Cuprate Superconductors under STM/STS", K. Kitazawa, T. Hasegawa, H. Ikuta, M. Nantoh, W. Wei, and N. Motohira, *Physics of High-Temperature Superconductors*, edited by S. Maekawa, and M. Sato, Springer-Verlag, Berlin, Heidelberg, 313 (1992).
- [33] "Anisotropic Electronic Structures of Oxide Superconductors Investigated by STM at Cryogenic Temperatures", T. Hasegawa, M. Nantoh, H. Ikuta, and K. Kitazawa, *Electronic Properties and Mechanisms of High T_c Superconductors*, edited by T. Oguchi, K. Kadowaki, and T. Sasaki, Elsevier Science, Amsterdam, 71 (1992).
- [34] "Cryogenic STM/STS of Sub-Nanometer Superstructure in High- T_c Thin Films", M.

LIST OF PUBLICATIONS

Kawasaki, M. Nantoh, K. Fujito, R. Tsuchiya, T. Hasegawa, K. Kitazawa, and H. Koinuma, *Nanostructures and Quantum Effects*, edited by H. Sakaki, and H. Noge, Springer-Verlag, Berlin, Heidelberg, 341 (1994).

Acknowledgements

There are many people who have contributed to the work presented in this dissertation. First of all, I wish to express my sincere appreciation to Prof. Koichi Kitazawa. He has provided tremendous mental and physical support throughout this study. His consideration has always been beyond my expectation, and his encouragement has been my motive force of this work. He is the hardest worker I have ever met, and I learned from him the fact that I should be a hard worker if I hope to succeed in something. He is one of the rare persons who possess a broad view of the society and the world situation as well as exceptional scientific talent.

All of the members of the Kitazawa Laboratory deserve many thanks for the creative discussions and friendship. Prof. Tetsuya Hasegawa has been my supervisor for these six years. I appreciate his help with electronics and software techniques and interpretation on the data. He is a very excellent scientist with well-balanced wide learning. He made me realize what I should study as an experimentalist. I am very much indebted to Mr. Naobumi Motohira who provided BSCCO single crystals of superior quality. Special thanks go to Prof. Kohji Kishio for his providing valuable suggestion and very careful proofreading of this dissertation. Thanks also goes to Prof. Kaoru Yamafuji, Dr. Hiroshi Ikuta, and Mr. Junichi Shimoyama for fruitful discussions and providing useful information. I am indebted to my collaborators which include Messrs. Tamotsu Tominaga, Akihiko Takagi and Masahiro Ogino. Other members in this laboratory are all to be thanked for providing a pleasant environment to work in.

I am also grateful to the people of the Koinuma Laboratory (Tokyo Institute of Technology). Prof. Hideomi Koinuma provided an opportunity to start this collaborative work and has been generous about it. Dr. Masashi Kawasaki is a very active scientist with bottomless vitality. His brain is always filled with ideas of new experiments. His continuous encouragement and valuable suggestion have sustained my interest in the experiments. Dr. Jianping Gong, Messrs. Kenji Fujito and Ryuta Tsuchiya prepared a lot of high quality YBCO thin films, and solved the problems arising from the specimens.

Finally, I would like to express my sincere gratitude to my parents for their endless tolerance, support and love, and also to my fiancée Miki Ishida for her sympathy and cheerful smile.

March, 1995

Masashi NANTOH





Kodak Color Control Patches

Blue Cyan Green Yellow Red Magenta White 3/Color Black

Kodak Gray Scale

A 1 2 3 4 5 6 M 8 9 10 11 12 13 14 15 B 17 18 19

C Y M

© Kodak, 2007 TM Kodak